

INVESTIGATION OF SOIL MOISTURE CONTENT IN SOIL UNDER DIFFERENT PREPARATION MODES USING ELECTRICAL RESISTIVITY AND GUIDED WAVE SOUNDING METHODS

By

ISSAHAKU SONTAA JAKALIA

(BSc. Physics and Computer Science)

**A Thesis Submitted to the Department of Physics, Kwame Nkrumah University of
Science and Technology in partial fulfillment of the requirements for the
degree of**

MASTER OF PHILOSOPHY (GEOPHYSICS)

College of Science

Supervisor: Dr. Akwasi Acheampong Aning

© Department of Physics

October 23, 2014

Declaration

I hereby declare that this submission is my own work towards the award of M.Phil degree and that, to the best of my knowledge, it contains no material previously published by another person or material which has been accepted for the award of any degree of the university, except where due acknowledgement has been made in the text.

Issahaku Sontaa Jakalia (20291838)

.....

.....

Student Name & ID

Signature

Date

Certified by:

Dr. Akwasi Acheampong Aning

.....

.....

Supervisor Name

Signature

Date

Certified by:

Prof. Sylvester K. Danuor

.....

.....

Head of Dept. Name

Signature

Date

Abstract

Continuous vertical electrical sounding (CVES) and the guided wave sounding (GWS) methods were used to investigate the soil moisture content of a maize farm at the KNUST Agricultural Research Station (ARS), Anwomaso, Kumasi – Ghana. The soils of the maize farm were categorized with four different land preparation modes; ploughed-harrowed, ploughed, hoed and no-till plot. Time-lapse measurement of the CVES was carried out using the multi-electrode Wenner array to produce 2D resistivity models as a result of soil moisture variation with the help of the ABEM Terrameter SAS 4000 resistivity meter. The GWS method (an invasive application of the ground penetrating radar (GPR)) retrieved the soil moisture content by analyzing reflections from the lower end of a metal rod with the help of an access tube preinstalled in the soil and a GPR system with 800 MHz shielded antenna. The results showed a heterogeneous distribution of soil moisture content both spatially and temporally. Most of the water available for plants' uptake was within a depth of 0.20 – 0.40 m which coincided with the root zones of the maize crops. In addition, the no-till plot was found to conserve more moisture during dry weather conditions than the rest of the plots. The research shows that CVES and GWS techniques are efficient in monitoring shallow soil water content in the field and the results obtained could be used to optimize irrigation scheduling and to assess the potential for variable-rate irrigation.

Contents

| | |
|---|-------------|
| Declaration | i |
| Abstract | ii |
| List of Tables | viii |
| List of Figures | xii |
| List of Symbols and Acronyms | xiii |
| Acknowledgements | xv |
| 1 INTRODUCTION | 1 |
| 1.1 Introduction | 1 |
| 1.2 Literature Review | 4 |
| 1.3 Statement of the Problem | 10 |
| 1.4 Project Objectives | 11 |
| 1.5 Justification of Objectives | 11 |
| 1.6 Thesis Layout | 12 |
| 2 THEORETICAL BACKGROUND OF GEOPHYSICAL METHODS USED | 13 |
| 2.1 Theory and Basic Principles of Electrical Resistivity | 13 |

| | | |
|-------|--|----|
| 2.1.1 | Equipotential Distribution of Current on the Subsurface | 16 |
| 2.1.2 | Electrode Array and Geometrical Coefficient | 17 |
| 2.2 | Basic Electrode Arrays | 20 |
| 2.2.1 | Wenner Array | 21 |
| 2.2.2 | Schlumberger Array | 22 |
| 2.2.3 | Gradient Array/Asymmetrical Schlumberger | 22 |
| 2.2.4 | Dipole-dipole Array | 23 |
| 2.2.5 | Pole-dipole Array | 23 |
| 2.2.6 | Pole-pole Array | 24 |
| 2.3 | Resistivity of Earth | 24 |
| 2.3.1 | Electrical Resistivity as a Function of Soil Water Content | 26 |
| 2.4 | Depth of Current Penetration | 29 |
| 2.5 | Modes of Electrical Resistivity Surveying | 30 |
| 2.5.1 | Vertical Electrical Sounding (VES) | 31 |
| 2.5.2 | Profiling | 31 |
| 2.5.3 | Continuous Vertical Electrical Sounding (CVES) | 32 |
| 2.5.4 | Time–lapse CVES Measurement | 33 |
| 2.6 | Theoretical Background of Ground Penetrating Radar (GPR) | 34 |
| 2.6.1 | Fundamentals of Electromagnetic Wave | 35 |
| 2.6.2 | Reflection of Electromagnetic Waves | 40 |
| 2.6.3 | Dielectric Coefficient of Geological Materials | 40 |
| 2.6.4 | The Guided Wave Method | 42 |
| 2.7 | Summary of Background to Methods | 44 |

3 MATERIALS AND METHODS

45

| | | |
|---------|---|----|
| 3.1 | Project Site Description | 45 |
| 3.1.1 | Geological Setting of the Project Area | 47 |
| 3.1.2 | Major Soil Types | 48 |
| 3.1.3 | Location and Accessibility | 49 |
| 3.1.4 | Physiography | 49 |
| 3.1.5 | Climatic Conditions and Vegetation | 50 |
| 3.2 | Materials and Equipment used for Data Collection | 50 |
| 3.2.1 | The ABEM LUND Imaging system | 51 |
| 3.2.1.1 | Modification of Electrodes/Improvised Electrodes | 51 |
| 3.2.2 | The RAMAC GPR System | 53 |
| 3.2.3 | Access Tubes and Wave Guide | 53 |
| 3.3 | Data Acquisition | 54 |
| 3.3.1 | Reconnaissance Survey | 55 |
| 3.3.2 | Data Acquisition Using ABEM Terrameter | 56 |
| 3.3.3 | Data acquisition using Guided Wave Sounding Technique | 58 |
| 3.4 | Processing of Field Data | 61 |
| 3.4.1 | 2D Resistivity Data Processing with RES2DINV | 61 |
| 3.4.2 | 2D Time-lapse Data Processing with RES2DINV | 62 |
| 3.4.2.1 | Editing of Data | 63 |
| 3.4.2.2 | Sorting of Data | 63 |
| 3.4.2.3 | Concatenation/Merging of Files | 64 |
| 3.4.2.4 | Inversion of Files | 64 |
| 3.5 | Processing of GWS Data using REFLEXW | 65 |

4 RESULTS AND DISCUSSIONS 67

| | | |
|----------|---|------------|
| 4.1 | Introduction | 67 |
| 4.2 | Spatial and Temporal Variation of Soil Moisture Content | 67 |
| 4.2.1 | Spatial and Temporal Variation of Soil Moisture Content in Ploughed-harrowed Plot | 68 |
| 4.2.2 | Spatial and Temporal Variation of Soil Moisture Content in Ploughed Plot | 72 |
| 4.2.3 | Spatial and Temporal Variation of Soil Moisture Content in Hoed Plot | 77 |
| 4.2.4 | Spatial and Temporal Variation of Soil Moisture Content in No-till Plot | 81 |
| 4.3 | Comparative Analysis of Soil Moisture Content Variation Based on Land Preparation Modes | 85 |
| 4.4 | Quantification of the Soil Water Content Available for Plant Uptake | 89 |
| 4.4.1 | Volumetric Water Content Distribution in Ploughed-harrowed plot | 90 |
| 4.4.2 | Volumetric Water Content Distribution in Ploughed Plot | 93 |
| 4.4.3 | Volumetric Water Content Distribution in Hoed Plot | 95 |
| 4.4.4 | Volumetric Water Content Distribution in No-till Plot | 97 |
| 4.5 | Comparison of CVES and GWS Results | 99 |
| 4.5.1 | CVES and GWS Results of Ploughed-harrowed Plot | 99 |
| 4.5.2 | CVES and GWS Results of Ploughed Plot | 100 |
| 4.5.3 | CVES and GWS Results of Hoed Plot | 102 |
| 4.5.4 | CVES and GWS Results of No-till Plot | 103 |
| 5 | CONCLUSION AND RECOMMENDATIONS | 104 |
| 5.1 | Conclusion | 104 |
| 5.2 | Recommendations | 107 |
| | REFERENCES | 109 |

| | |
|---|------------|
| A | 118 |
| A.1 Volumetric Water Content (VWC) Graphs | 118 |
| A.2 Calculation of Volumetric Water Content (VWC) | 120 |
| A.3 Contour Map | 120 |
| A.4 Shell Script Files | 121 |
| B | 123 |
| B.1 Used Softwares | 123 |

List of Tables

| | | |
|-----|--|-----|
| 2.1 | Resistivity of Rocks, minerals and industrial chemicals (Loke and Lane Jr, 2004) | 26 |
| 2.2 | Materials attenuation and relative permittivity measured at 100 MHz (Daniels, 1996) | 42 |
| 2.3 | Attenuation effects of the electromagnetic wave propagation for different conductivities of the embedding dielectric (Preko and Wilhelm, 2012) . . . | 44 |
| A.1 | Calculation of Volumetric Water Content (VWC) | 120 |

List of Figures

| | | |
|-----|---|----|
| 2.1 | Resistivity of an elemental cylindrical material | 14 |
| 2.2 | Current flow distribution in a homogeneous soil from a single electrode . . | 16 |
| 2.3 | Electrode configuration used in resistivity measurements (A, B: current electrodes, C, D: potential electrodes | 18 |
| 2.4 | Schematic diagram of four electrodes system used for measurements | 19 |
| 2.5 | Basic electrode arrangement used in DC resistivity surveying | 21 |
| 2.6 | Relationship between the VWC and electrical resistivity for different soil types (obtained from Michot et al. (2003)) | 29 |
| 2.7 | Fraction of current penetrating below a depth Z for current electrode separation L (Modified after Telford et al. (1990)) | 30 |
| 2.8 | (a) Arrangement of electrodes for 2D electrical survey and the sequence of measurements used to build up a pseudosection (b) Roll-along technique to cover more area (Loke, 2001) | 33 |
| 2.9 | Cylindrical soil model with a metal rod of radius a at the centre surrounded by a thin packet of air (Preko and Wilhelm, 2012) | 43 |
| 3.1 | (a) Project Site (b) Layout of Survey Profiles at the site | 46 |
| 3.2 | Geological map of Kumasi Metropolis showing the study area in red (Ghana, Geological Survey, 2009) | 48 |

| | | |
|------|--|----|
| 3.3 | Set of Terrameter for CVES measurement (a) Drum (b) Terrameter (c) Selector (d) Battery (e) Jumper (f) Cable (g) Stand | 51 |
| 3.4 | (a) Schematic design of electrode (b) Improvised electrode | 52 |
| 3.5 | MALA GPR System (a) 800 MHz Shielded antenna (b) XV Monitor (c) MALA ProEX control unit | 53 |
| 3.6 | (a) PVC pipes (b) Metal rod | 54 |
| 3.7 | Sketch of the electrodes for the 2D electrical resistivity survey and sequence of measurements for building the pseudo-section (Loke, 2001) | 56 |
| 3.8 | (a) Laying of cables (b) Cable-jumper- electrodes connection (c) Set-up of system | 58 |
| 3.9 | Schematic diagram showing reflected waves from the end of the metal rod . | 59 |
| 3.10 | (a) Set-up of GWS measurement (b) Operator taking GWS measurement . . | 60 |
| 3.11 | Pseudo-section showing bad data points with a spike | 62 |
| 3.12 | Flow diagram for time-lapse data processing | 63 |
| 3.13 | (a) Raw data with no processing performed. (b) after background removal, bandpass frequency, dynamic correction, static correction and f-k filter were carried out. | 66 |
| 3.14 | (a) Picks from the reflections arising from lower end of metal (b) reflections from graduations in metal rod | 66 |
| 4.1 | Ploughed-harrowed plot resistivity models from 10th – 24th June; (a) 10/06/13 (b) 11/06/13 (c) 12/06/13 (d) 13/06/13 (e) 17/06/13 (f) 19/06/13 (g) 20/06/13 (h) 24/06/13 | 69 |

| | | |
|------|--|----|
| 4.2 | Ploughed-harrowed plot percentage change in resistivity models from 11th – 24th June; (a) 11/06/13 (b) 12/06/13 (c) 13/06/13 (d) 17/06/13 (e) 19/06/13 (f) 20/06/13 (g) 24/06/13 | 71 |
| 4.3 | Ploughed plot resistivity models from 10th – 24th June; (a) 10/06/13 (b) 11/06/13 (c) 12/06/13 (d) 13/06/13 (e) 17/06/13 (f) 19/06/13 (g) 20/06/13 (h) 24/06/13 | 74 |
| 4.4 | Ploughed plot percentage change in resistivity models from 11th – 24th June; (a) 11/06/13 (b) 12/06/13 (c) 13/06/13 (d) 17/06/13 (e) 19/06/13 (f) 20/06/13 (g) 24/06/13 | 76 |
| 4.5 | Hoed plot resistivity models from 10th – 24th June; (a) 10/06/13 (b) 11/06/13 (c) 12/06/13 (d) 13/06/13 (e) 17/06/13 (f) 19/06/13 (g) 20/06/13 (h) 24/06/13 | 78 |
| 4.6 | Hoeing plot percentage change in resistivity models from 11th – 24th June; (a) 11/06/13 (b) 12/06/13 (c) 13/06/13 (d) 17/06/13 (e) 19/06/13 (f) 20/06/13 (g) 24/06/13 | 80 |
| 4.7 | No-till plot resistivity models from 10th – 24th June; (a) 10/06/13 (b) 11/06/13 (c) 12/06/13 (d) 13/06/13 (e) 17/06/13 (f) 19/06/13 (g) 20/06/13 (h) 24/06/13 | 82 |
| 4.8 | No-till plot percentage change in resistivity models from 11th – 24th June; (a) 11/06/13 (b) 12/06/13 (c) 13/06/13 (d) 17/06/13 (e) 19/06/13 (f) 20/06/13 (g) 24/06/13 | 84 |
| 4.9 | Resistivity models obtained on 19/06/13; (a) Ploughed-harrowed plot (b) Plough plot (c) Hoed plot (d) No-till plot | 86 |
| 4.10 | Resistivity models obtained on 16/08/13; (a) Ploughed-harrowed plot (b) Plough plot (c) Hoed plot (d) No-till plot | 87 |
| 4.11 | Ploughed-harrowed plot VWC distribution (a) VWC graphs from 22/07/13 – 23/08/13 (b) Temporal VWC distribution from 22/07/13 – 23/08/13 . . . | 92 |

| | | |
|------|--|-----|
| 4.12 | Ploughed plot VWC distribution (a) VWC graphs from 22/07/13 – 23/08/13 (b) Temporal VWC distribution from 22/07/13 – 23/08/13 | 94 |
| 4.13 | Hoed plot VWC distribution (a) VWC graphs from 22/07/13 – 23/08/13 (b) Temporal VWC distribution from 22/07/13 – 23/08/13 | 96 |
| 4.14 | No-till plot VWC distribution (a) VWC graphs from 22/07/13 – 23/08/13 (b) Temporal VWC distribution from 22/07/13 – 23/08/13 | 98 |
| 4.15 | Ploughed-harrowed plot CVES and GWS results measured on 24/07/13 (a) Resistivity model (b) Spatial VWC distribution map | 100 |
| 4.16 | Ploughed plot CVES and GWS results measured on 24/07/13 (a) Resistivity model (b) Spatial VWC distribution map | 101 |
| 4.17 | Hoed plot CVES and GWS results measured on 24/07/13 (a) Resistivity model (b) spatial VWC distribution map | 102 |
| 4.18 | No-till plot CVES and GWS results measured on 24/07/13 (a) Resistivity model (b) Spatial VWC distribution map | 103 |
| A.1 | Ploughed-harrowed plot VWC graphs (a) hole 1 (b) hole 2 | 118 |
| A.2 | Ploughed plot VWC graphs (a) hole 2 (b) hole 3 | 118 |
| A.3 | Hoed plot VWC graphs (a) hole 1 (b) hole 3 | 119 |
| A.4 | No-till plot VWC graphs (a) hole 1 (b) hole 3 | 119 |
| A.5 | Contour Map of study area showing elevation (m) | 120 |
| A.6 | Shell script for Sorting of Data | 121 |
| A.7 | Shell Script for Merging of Files | 121 |
| A.8 | Sample time-lapse data file with five data sets | 122 |

List of Symbols and Acronyms

| | | | |
|-----------------|----------------------------------|----------|---------------------------------------|
| ∇ | Dirac delta function | μ_r | Relative magnetic permeability |
| π | Pi | μ_0 | Permeability of free space |
| a | Phase coefficient | E | Electric field |
| b | Attenuation coefficient | J | Current density |
| c | Speed of light in vacuum | L | Length |
| ϵ_{ef} | Effective dielectric coefficient | Z | Impedance |
| $\tan(\delta)$ | Loss Tangent | H | Harmonic Velocity |
| v | Velocity | A | Area |
| Ω | Ohms | R | Resistance |
| σ | Conductivity | J | Jacobian matrix of partial derivative |
| ρ | Resistivity | D | Electric displacement current vector |
| ρ_a | Apparent Resistivity | I | Current |
| ϕ | Porosity | V | Voltage |
| S | Saturation | K | Geometric factor |
| ρ_w | Resistivity of ground water | t | Time |
| ϵ_0 | Permittivity of free space | 1D | One dimensional |
| θ_v | Volumetric water content | 2D | Two dimensional |
| B | Magnetic flux density vector | 3D | Three dimensional |
| H | Magnetic field intensity vector | VWC | Volumetric water content |
| P | Poynting vector | GPR | Ground penetrating radar |

CVES Continuous vertical electrical sounding

ERI Electrical Resistivity Imaging

ERT Electrical Resistivity Tomography

RMS Root Mean Square

VES Vertical Electrical Sounding

TWTT Two way travel time

Acknowledgments

My first thanks and heartfelt gratitude goes to the Almighty God for His unprecedented mercies and grace towards me throughout the duration of this work. I honestly thank my supervisors Dr. Akwasi Acheampong Aning and Dr. Kwasi Preko for their encouragement, motivation, technical advice and criticism that helped me through field work to the end of this project. I would also like to thank Prof. S. K. Danuor, Head of Department and the entire Physics Department for the financial support and provision of field equipment during the field work. To Dr. L. Amekudzi, Dr. M. K. E. Donkor and Mr. Ernest Asare I say God richly bless you for the support in Linux and Latex platform i used. I appreciate all the lecturers who took me through the geophysics programme and to all my course mates – Messrs. Obed Sedoawu, Emmanuel H. Tetteh, George Hinson, Richard K. Akorlie, Desmond Appiah, Nana Kofi Appiah - Badu and Evans K. Quaye who shared their knowledge and time on this project I say God bless you. In addition, I thank all Physics Laboratory Technicians especially Mr. Thomas Dwomoh, for their immense support. I am also grateful to my friend, course mate and field partner, Mr. Nathaniel Sackey who tirelessly helped me throughout this project, I say God richly bless you. Much appreciation also goes to Ghana Education Trust fund (GETFund) for their financial support throughout my two year programme. My final thanks go to my family members, especially my father, Mr. Abudulai Jakalia who understands and had hope in me; I really appreciate your support in diverse ways.

CHAPTER 1

INTRODUCTION

1.1 Introduction

Geophysical techniques are applied for the exploration of geotechnical structures and they provide several operational frequencies for the determination of soil moisture content distribution within the subsurface (Preko, 2007). For any geophysical techniques to work better and efficiently, it must be able to detect and predict subtle changes in the subsurface and this actually posed as a challenge to many methods.

So far, no single method has been able to measure the water content directly in the field due to factors such as soil types, surface characteristics, land use, vegetation and orography (Teuling and Troch, 2005), hence geophysical methods measure soil physical properties such as electrical resistivity and dielectric permittivity, among others, that varies with water saturation. These physical properties are then transformed into petrophysical parameters using an appropriate relationship to estimate the soil moisture content. Using geophysical methods to study the hydrogeology of the subsurface increase measurement speed, effort needed and most importantly larger area can be sampled as compared to use of inserted probes or devices.

One of the geophysical techniques which is frequently applied is electrical resistivity tomography (ERT) also known as continuous vertical electrical sounding (CVES). In this

method, artificial current is injected into the subsurface through current electrodes and the potential is measured across two potential electrodes. Potential difference patterns provide information on the form of subsurface heterogeneities such as water content in the soil which influences their electrical properties (Kearey et al., 2009).

The CVES imaging is popular nowadays due to its ability to produce images of the subsurface efficiently and effectively as a result of the availability of automated data acquisition systems and efficient user friendly inversion softwares (Aning et al., 2013). It incorporates sounding and profiling techniques to give information on both the lateral and vertical extent of the subsurface with better resolution. Several electrode arrays exist in the CVES. These include gradient, square, dipole-dipole, wenner, schlumberger, etc, and each array configuration has its specific advantages and disadvantages. The choice of the array depends on the type of heterogeneity to be mapped and also on the background noise level; the characteristics of an array have to be taken into account (Samouëlian et al., 2005). The wenner array, as compared to the others such as gradient, square, dipole-dipole and schlumberger, covers an intermediate resolution and shows moderate to near surface lateral effects such as soil moisture content. Hence, it has been employed in this project.

Ground Penetrating Radar (GPR) also emerges when the equation of homogeneity arises (Barner et al., 2001). One innovative method of the GPR which is widely gaining ground is the guided wave sounding (GWS) technique. The guided wave sounding (GWS) survey is similar to that of the conventional time domain reflectometry (TDR) since it is an invasive application of the GPR technique. This method (GWS) estimates the soil moisture content (VWC) by making use of the two-way reflection time data from the lower end of a metal rod which is lowered into the soil by constant increments through a vertical access tube (Schmalholz et al., 2004; Preko and Wilhelm, 2006; Preko and Rings, 2007). Due to the unstandardized nature of this technique, results from the GPR methods are subjective and

interpretation depends on the user experience (Preko, 2007).

Knowledge of soil moisture content distribution is important in several disciplines such as climate science, hydrology, meteorology and most importantly, agriculture (Lunt et al., 2005). In the case of agriculture, management practices and environmental factors such as temperature, moisture content, and solar radiation influence crop growth. Highest crop yield can only be achieved under optimum moisture conditions during the growing season whilst a drop in the moisture content at any of the growth stages will result in poor yield.

Moreover, information obtained from the distribution of soil water content in unsaturated zone is important for variety of investigations such as climate research, flood prevention, solute matter transport into the subsurface or decomposition and transformation processes in the soil.

Graham et al. (2013) indicated that the information obtained from the monitoring of soil moisture content is critical for increasing crop yields, achieving high irrigation efficiencies, planning irrigation scheduling, and minimizing loss of yield due to waterlogging and salinization. Such water content monitoring is also vital for addressing issues of water quality which is important for managing the environmental impacts of irrigated agriculture and for protecting functional ecosystems. In addition, detailed knowledge of the spatial and temporal variability of soil moisture content is important because it influences the energy balance in the planetary boundary layer via albedo (Dai et al., 1999).

This research investigated the soil moisture content of maize farm in the KNUST Agricultural Research Station (ARS) – Anwomaso, Kumasi – Ghana using continuous vertical sounding (CVES) technique and the guided wave sounding (GWS) technique of the GPR. It sought to explore the potential of using the CVES and the GWS in the monitoring of spatial and temporal variability of soil water content available for plants use.

The combination of the two methods will enhance the quality and predictability of soil

moisture data more than the use of single method. In addition, it is better to use integrated methods sensitive to different physical properties (as the electrical method is sensitive to electrical resistivity and the GPR response to differing dielectric permittivity of the soil) and are able to complement each other, thereby providing an integrated approach to a geological problem, and thus help reduce ambiguity in interpretation.

1.2 Literature Review

Over the years, there have been several attempts to determine the water content of soils due to its importance in several disciplines. This has led to a wide variety of methods available for assessing soil water content. The choice of a method depends greatly on weighing its advantages over its disadvantages and the ultimate aim of the project. Gardner et al. (2008) defined soil water as that component of water in the soil, which could be lost through evaporation by heating the soil between 100 °C and 110 °C but usually 105 °C until there is no further weight loss.

Basically, there are two ways of soil water measurement i.e, the direct and indirect methods. The direct method involves the elimination of the soil water by using either physical or chemical process and subsequently determining the quantity of water removed, e.g. the gravimetric soil sampling method.

Indirect methods on the other hand, e.g. using ground penetrating radar (GPR), the nuclear magnetic resonance (NMR), time domain reflectometry (TDR) and electrical resistivity tomography (ERT) involve the monitoring of a soil property such as relative dielectric permittivity, electromagnetic reflectivity, hydrogen nuclei content or electrical resistivity respectively, as a function of the soil water content. In all these methods, data may be

acquired through the direct contact of instrument with the ground surface or remotely whereby the sensors are mounted on satellites or helicopters above the soil surface (Preko, 2007).

TDR has become the most widely used and accepted method for soil water content measurement (Topp et al., 1982). However, Nadler et al. (1991) and Zegelin et al. (1992) pointed out that, the sample volume of this method (TDR) is restricted to a small cylindrical volume along the probe length.

Other methods such as magnetic resonance sounding (MRS), georadar or electromagnetic induction methods (Tabbagh, 1985) provide information without the insertion of probes into the subsurface. According to Whalley and Bull (1991), remotely sensed microwave radiation has also been used to accurately estimate soil water content below 1 m depth over a larger area.

For some time now, geophysical methods have been widely applied to soil science. The basic principle in non-destructive geophysical methods is to gather data in the medium under investigation without destroying the subsurface. Several of these methods are available but those that use the electric properties of the soil seem promising for the reason that, soil materials and properties can be quantified through geoelectrical properties such as resistivity, dielectric permittivity, etc. Moreover, most soils and even rocks conduct electricity via the electrolytes of interstitial or tissue water. Also, electrical resistivity is one of the most variable of all physical properties ranging between $1.6 \times 10^{-8} \Omega\text{m}$ for native silver and about $1.0 \times 10^{16} \Omega\text{m}$ for pure sulphur (Telford et al., 1990). Electrical resistivity therefore, decreases with increasing pore water content, salinity and hydraulic conductivity, as well as temperature and vice versa.

Indeed, electrical resistivity prospecting is a very attractive method for soil water determination in agricultural fields, as compared to classical soil science measurements and

observations which disturb the soil by drilling and sampling. In this way, temporal and spatial soil water content variability in the field can be monitored and quantified without altering the soil structure or destroying the vegetative cover. Electrical resistivity measurements also provide a good means for detail studies of vertical water movement in the unsaturated soil zone and therefore should help to assess the boundary conditions for infiltration modeling (Benderitter and Schott, 1999).

Bevan (2000) reported that the first known equipotential map was compiled by Malamphy in 1938 for archaeological research at the site of Williamsburg in USA. From that time onwards, the interest in subsurface soil prospecting using electrical resistivity has progressively gone higher.

The estimation of water content by resistivity measurements requires knowledge of the concentration of dissolved ions. The problem in which most people during these early stages faced was the estimation of soil salinity variation as recorded by (Rhoades et al., 1977). But since salts have to be in an ionized form to conduct the current, the amount of water in soil therefore governs the available paths of conduction which helps to overcome the said problem. This has paved way for many researches in the use of electrical resistivity survey in soil science.

Bottraud et al. (1984) observed different patterns of water distribution related to variations in grape vine growth in a homogeneous sandy soil. They were able to establish a qualitative description of water transfer using the relative variation of apparent resistivity, during forty-five (45) days monitoring periods. Jackson et al. (2002) identified anomalies in a roadside embankment following repeated measurement of resistivity over an 18 months period, incorporating several wet and dry seasons. Samouëlian et al. (2003) monitored artificial cracks as they deepened and observed an increasing apparent resistivity anomaly over time. This pattern was related to climatology variation affecting groundwater table,

precipitation and temperature. Binley et al. (2002) also found a good correlation between the net rainfall and the change of the electrical resistivity in the depth of 0–0.82 m. Rings et al. (2008) used electrical resistivity tomography to quantify the water content of a dike model. The ERT method successfully quantifies the water content in the dike to be about 34%. This method is very important in the monitoring of the water content evolution of soil which is of interest in a broad range of applications such as energy balance over the land surfaces and the stability of flood-protection dikes. In another study, Brunet et al. (2010) monitored soil water content using electrical resistivity tomography (ERT) in the Cevennes area in France. He demonstrated the potential of measuring soil water content and water deficit using electrical resistivity, and describe how uncertainties in temperature, porosity and fluid conductivity impact electrical resistivities – obtained estimates of soil water content and deficit.

The success of ERT technique makes it even possible to quantify the water uptake by crops, as Srayeddin and Doussan (2009) who applied ERT as an alternative method for quantifying and spatialising root water uptake on a field scale. Their results indicated the usefulness and uniqueness of this technique for monitoring and estimating field water uptake by plants roots.

Nijland et al. (2010), in a separate study, evaluated the possibilities of using ERT to measure soil moisture availability and plant water use in the Mediterranean natural area and found that ERT was a useful tool for measuring soil conditions, providing information on the spatial patterns within the soil and reaching depths otherwise inaccessible. Based on the ERT results, they also found that even with the shallow and rocky nature of the soils, plant roots penetrated as deep as 6 m and below into the fractured and weathered bedrock to access water.

In another attempt to test the usefulness of the geoelectrical method for assessment of spatio-temporal variability of water content, Celano et al. (2011) successfully applied

Electrical Resistivity Imaging (ERI), under semi-arid climate, to evaluate the soil water content in tilled and cover-cropped olive orchards. The ERI techniques allowed them to underscore the differences between the systems in the dynamics of water distribution along the soil profile due to the adopted soil management. Cousin et al. (2009) described the spatial and temporal evolution of the hydraulic functioning at high resolution from electrical resistivity data. The interpretation of the water content and matric potential maps demonstrated that some hydraulic processes such as lateral overland flow can occur.

Based on the above, it is therefore evident that the ERT method has successfully been employed in investigating soil water content at various scales. However, as pointed out by Srayeddin and Doussan (2009), few studies actually reported the application of ERT in soil-plant system and none aimed at quantifying water uptake by the plants. It therefore, calls for more research into the area which this project sought to achieve at the end.

However the ERT, unlike the conventional methods (gravimetric and time-domain reflectometry), has difficulty in quantifying the amount of soil water content. Though there are petrophysical relationships such as Archie's law which relates the resistivity of the soil to that of the water content in the soil, the main challenge is how to estimate the parameters (soil cementation, temperature, porosity and soil saturation) in this relation. The success of the electrical method in quantifying soil water content therefore is based on making useful assumptions which had often led to erroneous results.

As a guide, it is therefore necessary to use an integrated method whereas the second method serves as a guide to complement the result of the ERT. One geophysical method whose application has gained ground and can successfully estimate the soil water content is the Ground Penetrating Radar (GPR). The success chalked by GPR techniques in monitoring soil water content makes it a better complementary method for this project.

The GPR technique measures the volumetric water content (VWC) of the soil from its

apparent dielectric permittivity measurements through the use of calibration equations such as Topp model (Topp et al., 1980) which relate the soil water content to the dielectric permittivity. It is generally considered to be a non-invasive method although it can be applied in an invasive mode in determining the soil water content. Over the years, several of these modes have been employed by different authorities to investigate the soil water content. Among these are reflection, apparent ground wave, air-launched surface reflection coefficient, amplitude spectra, structure transillumination as well as a new innovative method like the guided wave sounding technique.

The waveguide principle has been employed by a number of authors to investigate the soil water content. Recently Graham et al. (2013) applied the guided wave technique on a vegetable garden for monitoring the soil water content. The result showed that, on the average, the VWC at the top soil (0.065 m) containing humus was higher ($0.12 \text{ m}^3\text{m}^{-3}$) as compared to a deeper depth of 0.295 m ($0.10 \text{ m}^3\text{m}^{-3}$).

Preko and Wilhelm (2012) employed the guided wave sounding (GWS) and time domain reflectometry with intelligible micro elements (TRIME-TDR) to investigate the distribution of VWC in dike model under controlled conditions in order to detect possible dike damage. In another dike experiment, Preko et al. (2009) compared the invasive and non-invasive modes of the GPR to test the reliability of the results in determining the soil water at varying levels in the dike. This was to enhance a follow up of long term monitoring and surveillance of embankments as water retaining structures.

Further works, using the GPR methods to investigate soil moisture content, can be obtained from Topp et al. (1982); Scheuermann et al. (2001); Becker et al. (2002), among many others. It is based on this premise that, ERT, also known as CVES and GWS techniques, have been proposed as alternative geophysical tools for investigating the spatial and temporal variability of soil moisture content of a maize farm in the Kwame Nkrumah University of Science and

1.3 Statement of the Problem

All crops need water to grow and produce yields and the main source of water is rainfall. When rainfall is insufficient, supplementary irrigation water may be supplied to guarantee a good harvest. One of the challenges of irrigation is to determine the right amount of water that has to be supplied to meet crops demands. Too much water means a waste of water which is so precious in arid countries. It can also lead to a rise of the groundwater table and an undesirable saturation of the root zone.

Too little water during the growing season causes plants to wilt. Long periods, during which water supply is insufficient, result in loss of yield or even crop failure. In addition, the irrigation requirement needs to be determined for proper design of the irrigation system and for establishment of the irrigation schedules.

Furthermore, in a country like Ghana, where water is the most limiting factor for crop production under dry season farming, sustainable water resource management requires a good knowledge of the spatial variability of soil properties which strongly affect the water balance.

Traditional soil characteristics and their spatial and temporal variations are quantified using destructive, laborious and time consuming direct measurements on a wide number of soil samples which are often subjected to large errors. An integrated geophysical technique, such as CVES and GWS can be effectively and efficiently applied in-situ to describe the horizontal, vertical, spatial and temporal variability of soil water content for efficient irrigation management. This is what this research work sought to make evident.

1.4 Project Objectives

The main objective of this research was to monitor soil water content available for plant use in the near surface of the maize farm using continuous vertical electrical sounding and the guided wave sounding technique.

This research work also had the following specific objectives:

- To validate the CVES and GWS techniques as efficient and appropriate methods for soil water content estimation in the near surface.
- To determine the spatial and temporal variability of soil water content in the farm.
- To do a comparative study of the soil water content in the farm with different land preparation modes.

1.5 Justification of Objectives

The implementation of sustainable practices in agriculture is one of the main strategies adopted by many countries in the world including Ghana, to solve problems such as food shortages, water shortage, desertification, greenhouse effect among others which are threatening the environment and human welfare. Sustainable soil management technologies such as irrigation management and enrichment of soil through fertilizer applications play a fundamental role in crop growth because they are aimed at improving productivity and increasing the well being of the populace.

Shortages of water and increases in energy costs are an incentive for many crop farmers to consider variable – rate irrigation. An efficient irrigation system should meet crops demands

for water. A limited water supply may result in reduction in yield while excess irrigation is a waste of resources. The outcome of this work could be used to optimize irrigation scheduling and to assess the potential for variable – rate irrigation and also to improve water efficiency, thereby, significantly increasing productivity and conserving fuel for economic growth.

1.6 Thesis Layout

The thesis consists of five (5) chapters with each chapter addressing a main heading. Chapter 1 introduces the subject matter, outlining the background of the research, literature review (previous research works), and objectives of the research as well as justification of the objectives.

Chapter 2 outlines the main fundamental theories behind electrical resistivity method and ground penetrating radar.

Chapter 3 presents a review of the geology of the study area, location and accessibility of the research area, physiography, climate and occupation of inhabitants of the research area. An overview of the methods used to acquire the datasets and some available softwares for enhancing the datasets is also presented. The chapter also outlines the steps employed in the data processing.

Chapter 4 analyses the results obtained from the electrical and GPR surveys data with detailed interpretation. The results are also discussed, compared to results of other research works.

Finally, Chapter 5 draws conclusions from the research and makes recommendations for future work.

CHAPTER 2

THEORETICAL BACKGROUND OF GEOPHYSICAL METHODS USED

2.1 Theory and Basic Principles of Electrical Resistivity

Electrical resistivity surveying on the subsurface is based on the principle that the distribution of electrical potential in the ground around a current-carrying conductor depends on the electrical resistivity and distribution surrounding soils and rocks. Therefore, the purpose of electrical resistivity surveys is to determine the resistivity distribution in the surrounding soil volume. Potential difference patterns supply information on the form of subsurface heterogeneities and their electrical properties (Kearey et al., 2002). The greater the electrical contrast between the soil matrix and heterogeneity, the easier is the detection.

The basic theory governing the electrical resistivity survey is Ohm's law which controls the flow of current in a conducting medium.

Consider an element of a heterogeneous material shown in Figure 2.1, a current is passed through the cylinder causing a potential drop $-\delta V$ between the ends of the element. According to Ohm's law, the current that flows in a conductor is proportional to the voltage across the conductor.

Mathematically,

$$-\delta V \propto I \tag{2.1}$$

which can be written as:

$$-\delta V = \delta R I \quad (2.2)$$

The constant of proportionality, δR , is the resistance of the conductor which opposes the flow of current in a material.

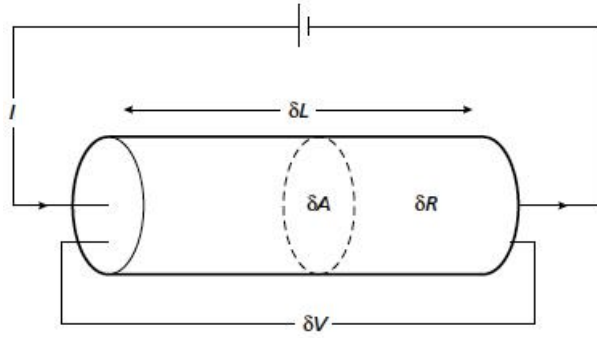


Figure 2.1: Resistivity of an elemental cylindrical material

For the elemental conducting cylinder in Figure 2.1, the resistance δR is proportional to the length δL and inversely proportional to the cross-sectional area δA , of the conductor;

$$\delta R \propto \frac{\delta L}{\delta A} \quad (2.3)$$

hence

$$\delta R = \rho \frac{\delta L}{\delta A} \quad (2.4)$$

where the constant of proportionality ρ is the resistivity, which is a physical property that expresses the ability of the material to opposes the flow of current. It is defined as the resistance in ohms between the opposite faces of a unit cube of the material (Kearey et al., 2002). The SI unit of resistivity is the ohm-metre (ohm.m) and the reciprocal of the resistivity is termed conductivity σ (units: Siemens (S) per metre; $1 \text{ Sm}^{-1} = 1 \text{ ohm}^{-1}\text{m}^{-1}$

the term 'mho' for inverse 'ohm' is sometimes encountered).

Thus:

$$\sigma = \frac{1}{\rho} \quad (2.5)$$

Substituting for δR in equation (2.4) with equation (2.2) and rearranging,

$$\frac{\delta V}{\delta L} = -\frac{\rho I}{\delta A} = -\rho J \quad (2.6)$$

where $\frac{\delta V}{\delta L}$ represents the potential gradient through the element in Volt.m⁻¹ and J the current density in Am⁻².

Generally, the current density in any direction within a material is given by the negative partial derivative of the potential in that direction divided by the resistivity.

In the form of the current density J , the electric field intensity E and the conductivity of the medium σ , Ohm's law can be re-written as:

$$J = \sigma E \quad (2.7)$$

But the physical parameter which is normally measured in the field is the electric potential V and it is related to the electric field in equation (2.8):

$$E = -\nabla V \quad (2.8)$$

Hence, by combining equation (2.7) and (2.8), equation (2.9) is derived:

$$J = \sigma \nabla V \quad (2.9)$$

2.1.1 Equipotential Distribution of Current on the Subsurface

In a homogeneous and isotropic half-space, the electric field lines surrounding a source (positive) electrode, which powers the subsurface, are directed radially outward, as in Figure 2.2. The electrical equipotentials are hemispherical when the current electrodes are located at the soil surface (Scollar et al., 1990; Kearey et al., 2002). In addition, the potential distribution around a source is positive which decreases as $1/r$ with increasing distance whilst that of the sink is negative, where the current flows out of the ground. Thus, around a sink the potential increases (becomes less negative) as $1/r$ with increasing distance from the sink. From the above observations, it is possible to calculate the potential difference between a second pair of electrodes at known distances from the source and sink.

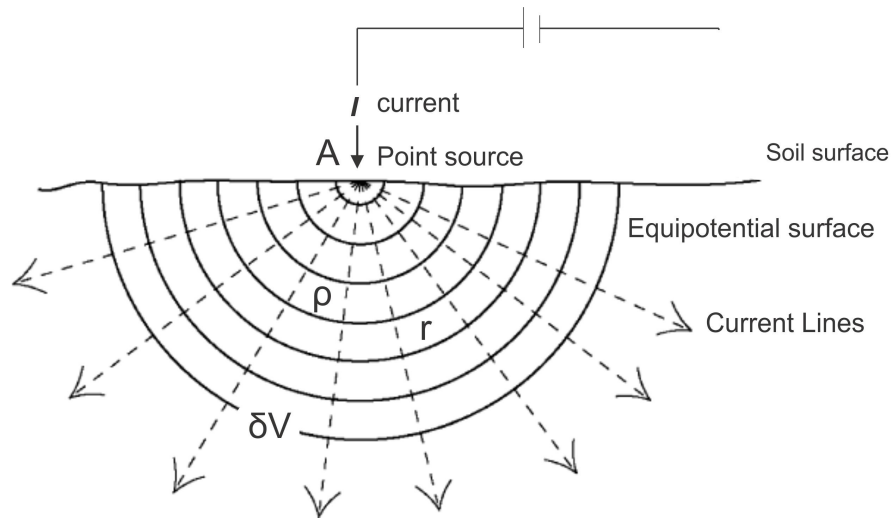


Figure 2.2: Current flow distribution in a homogeneous soil from a single electrode

Consider a single electrode on the surface of a medium of uniform resistivity ρ , as shown in Figure 2.2. To complete the circuit, a sink is placed at large distance from the electrode where the measurement is taken. Current flows radially away from the electrode so that the current distribution is uniform over hemispherical shells centered on the source.

At a distance r from the electrode, the shell has a surface area of $2\pi r^2$ so the current density J is given by;

$$J = \frac{I}{2\pi r^2} \quad (2.10)$$

From equation (2.6), the potential gradient associated with this current density is:

$$\frac{\partial V}{\partial r} = -\rho J = -\frac{\rho I}{2\pi r^2} \quad (2.11)$$

By integrating, the potential V_r at a distance r as shown in Figure 2.2 as;

$$V_r = \partial V = - \int \frac{\rho I \partial r}{2\pi r^2} = \frac{\rho I}{2\pi r} \quad (2.12)$$

where, the constant of integration is zero since $V_r = 0$ when $r = \infty$

Therefore, the potential at a distance r from a single point current source I , as shown in Figure 2.2 is given as:

$$V_r = \frac{\rho I}{2\pi r} \quad (2.13)$$

2.1.2 Electrode Array and Geometrical Coefficient

Practically, it is not possible to use a single electrode for resistivity measurement. Hence, measurement of electrical resistivity usually requires four electrodes; two electrodes called A and B that are used to inject current (current electrodes), and two other electrodes labeled C and D are used to record the resulting potential difference (potential electrodes) (Fig. 2.3).

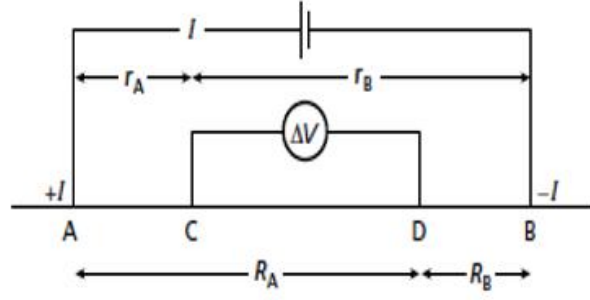


Figure 2.3: Electrode configuration used in resistivity measurements (A, B: current electrodes, C, D: potential electrodes)

Now, considering the case where the sink is at a finite distance from the source (Fig. 2.3), the potential V_C at an internal electrode C is the sum of the potential contributions V_A and V_B from the current source at A and the sink B. That is:

$$V_C = V_A + V_B \quad (2.14)$$

From equation (2.13)

$$V_C = \frac{\rho I}{2\pi} \left(\frac{1}{r_A} - \frac{1}{r_B} \right) \quad (2.15)$$

And similarly,

$$V_D = \frac{\rho I}{2\pi} \left(\frac{1}{R_A} - \frac{1}{R_B} \right) \quad (2.16)$$

However, absolute potentials are difficult to measure in the field, hence the potential difference ∇V between electrodes C and D is measured.

Therefore,

$$\nabla V = V_C - V_D = \frac{\rho I}{2\pi} \left(\left(\frac{1}{r_A} - \frac{1}{r_B} \right) - \left(\frac{1}{R_A} - \frac{1}{R_B} \right) \right) \quad (2.17)$$

Rearranging equation (2.17) in terms of the ground electrical resistivity;

$$\rho = \frac{2\pi \nabla V}{I \left[\left(\frac{1}{r_A} - \frac{1}{r_B} \right) - \left(\frac{1}{R_A} - \frac{1}{R_B} \right) \right]} \quad (2.18)$$

which can be written as;

$$\rho = \left[\frac{2\pi}{\left[\left(\frac{1}{r_A} - \frac{1}{r_B} \right) - \left(\frac{1}{R_A} - \frac{1}{R_B} \right) \right]} \right] \frac{\nabla V}{I} \quad (2.19)$$

$$\rho = K \frac{\nabla V}{I} \quad (2.20)$$

where,

$$K = \left[\frac{2\pi}{\left[\left(\frac{1}{r_A} - \frac{1}{r_B} \right) - \left(\frac{1}{R_A} - \frac{1}{R_B} \right) \right]} \right] \quad (2.21)$$

the K in equation (2.21) represents the geometrical coefficient which depends on the arrangements of the four electrodes A, B, C and D.

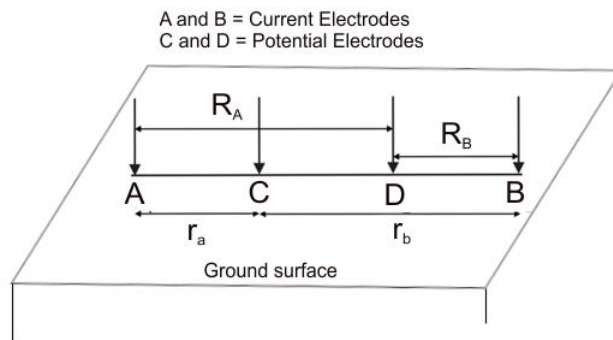


Figure 2.4: Schematic diagram of four electrodes system used for measurements

Practically, the current electrodes A, B and the potential electrodes C and D can be placed in the field at the soil surface (Fig. 2.4), or in boreholes. As compared with the surface

methods, the cross-borehole methods present the advantage of a high resolution with depth (Slater et al., 2000). The technique also requires intrusion into the studied bodies where the electrodes are inserted. At the laboratory scale, the technique can also be applied by placing the electrodes around the soil sample at various depths (Olsen et al., 1999)

In the case of a uniform ground, the resistivity calculated from equation (2.19) should be constant and independent of both electrode spacing and surface location. Since in almost all cases subsurface inhomogeneities exist, the resistivity will vary with the relative positions of the electrodes. Therefore, any computed value is then known as the *apparent resistivity*, ρ_a and will be a function of the form of the inhomogeneity.

Hence, for any electrode configuration, the basic equation for calculating the *apparent resistivity* is given as:

$$\rho_a = \left[\frac{2\pi}{\left[\left(\frac{1}{r_A} - \frac{1}{r_B} \right) - \left(\frac{1}{R_A} - \frac{1}{R_B} \right) \right]} \right] \frac{\nabla V}{I} \quad (2.22)$$

or

$$\rho_a = K \frac{\nabla V}{I} \quad (2.23)$$

2.2 Basic Electrode Arrays

Many electrode configurations have been designed for electrical resistivity surveying (Habberjam, 1979) based on the arrangement, separation of current and potential electrodes. The factors involved in choosing a particular array for a field work include the space available, labour intensity, dipping interfaces, sensitivity to lateral inhomogeneities, structure to be delineated, level of background noise and sensitivity of resistivity (Loke, 2001). The most common ones among them are wenner, schlumberger, gradient, dipole-dipole, dipole-pole and pole-pole arrays (Fig. 2.5).

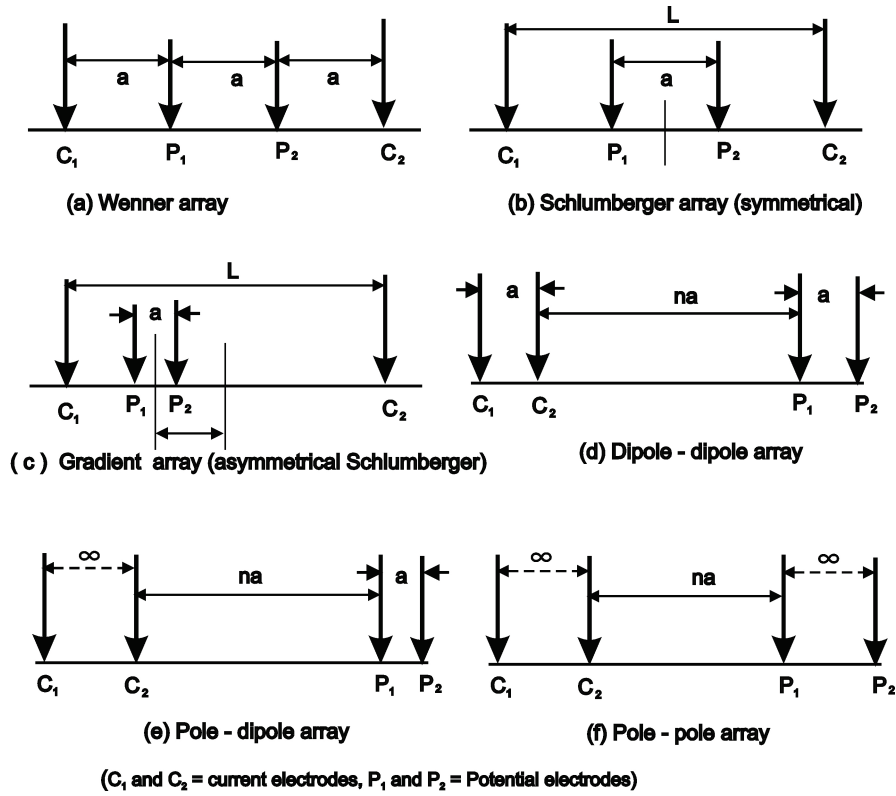


Figure 2.5: Basic electrode arrangement used in DC resistivity surveying

2.2.1 Wenner Array

The wenner array is very widely used and supported by a vast amount of interpretational literature and computer packages. It is described as the 'standard' array against which others are often assessed (Milsom, 2003). For this array, the separations between the current and the potential electrodes are the same (Fig. 2.5a). It is very sensitive to vertical changes in the subsurface (resolving of horizontal structures) but less sensitive to horizontal changes (resolving of vertical structures). In addition, it covers an intermediate depth range, has intermediate resolution and shows moderate sensitivity to near-surface lateral effects. The

apparent resistivity of the wenner array is given by:

$$\rho_a = 2\pi a \left(\frac{\nabla V}{I} \right) \quad (2.24)$$

where a is electrode spacing

2.2.2 Schlumberger Array

For this array, the potential electrodes are within the current electrodes (Fig. 2.5b and 2.5c).

One advantage of the schlumberger array is that, it resolves vertical structures better and penetrate deeper than the wenner array. Hence it is highly favoured, along with the wenner for electrical depth-sounding surveys (Milsom, 2003).

For the apparent resistivity;

$$\rho_a = \frac{\pi (L^2 - x^2)^2}{a (L^2 - x^2)} \left(\frac{\nabla V}{I} \right) \quad (2.25)$$

(where a = electrode separation, L = distance between current electrodes and x = separation between midpoints of the current and potential electrodes)

The schlumberger can be arranged symmetrically when $x = 0$, and equation (2.25) reduces to:

$$\rho_a = \frac{\pi L^2}{a} \left(\frac{\nabla V}{I} \right) \quad (2.26)$$

2.2.3 Gradient Array/Asymmetrical Schlumberger

Gradient array (Fig. 2.5c) is widely used for reconnaissance (Milsom, 2003). Large numbers of reading can be taken on the parallel transverses without moving the current electrodes

with the help of powerful generators. It is similar to Schlumberger array with the current electrodes at the extreme ends and that of the potential electrodes within them. Field measurement is done by the movement of the potential pair within the current pair.

2.2.4 Dipole-dipole Array

In the case of the dipole-dipole configuration, potential pair of electrodes is placed at one side of the survey line and the current electrodes at the other side (Fig. 2.5d). It is commonly used for induced polarization (IP) work because the complete separation of current and voltage circuits reduces the vulnerability of inductive noise. It is sensitive to horizontal changes in the subsurface but less sensitive to vertical changes. Information from different depths is obtained by changing the factor n .

In principle, the larger the value of ' n ', the deeper the penetration of the current paths sampled. Its apparent resistivity is given by:

$$\rho_a = \pi n a (n + 1)(n + 2) \left(\frac{\nabla V}{I} \right) \quad (2.27)$$

where n is the factor ranging from 1 to 5

2.2.5 Pole-dipole Array

It is an asymmetrical array with one of the current electrodes placed at a greater distance from the other three (Fig. 2.5e). This array produces asymmetric anomalies that are consequently more difficult to interpret than those produced by symmetric arrays (Milsom, 2003). Special care must therefore be observed during measurement because peaks are displaced from the

centers of the conductive bodies and the electrode positions. An advantage of this array is that, it has signal strength higher than that of the dipole-dipole.

Apparent resistivity is given as:

$$\rho_a = \pi na(n+1) \left(\frac{\nabla V}{I} \right) \quad (2.28)$$

2.2.6 Pole-pole Array

In this electrode configuration, the second current and potential electrodes are placed at a distance not more than twenty times the separation between the first current the potential electrodes (Fig. 2.5f). It is believed to have the deepest depth of investigation but with poorer resolution. The apparent resistivity is expressed as:

$$\rho_a = \pi na \left(\frac{\nabla V}{I} \right) \quad (2.29)$$

2.3 Resistivity of Earth

Soils and rocks on the surface of the earth have an intrinsic property (i.e. resistivity) that governs the relation between the current density and the gradient of the electrical potential. Therefore, variations in electrical resistivity of the earth materials produce a corresponding change in the relations between the applied current and the potential measured.

Electronic, electrolytic and dielectric conduction are considered to be the three modes through which current is conducted through the earth materials. In the electronic conduction, the current is transmitted through free mobile electrons as in the case of metal sulphides and

graphite. Electrolytic conduction occurs by the relative slow movement of ions within an electrolyte and depends upon the type of ion, ionic concentration and mobility. In the case of dielectric conduction, it occurs in poor conductors with a very few free charge carriers. Atomic electrons will be displaced with respect to nuclei separation of positive and negative charges (Reynolds, 1997).

Among the various types of rocks, sedimentary rocks tend to be the most conductive due to their high fluid content; igneous rocks has the highest resistivities and metamorphic rocks having intermediate but overlapping resistivities. For rocks, electrical current is mainly transmitted by the passage of ions in pore waters which is electrolytic rather ohmic processes. In essence, resistivity of igneous and metamorphic rocks depends on the rate of fracturing as well as the type of fluids within these fractures.

In soil science, the electrical resistivity is a function of a number of soil properties, including the nature of solid constituents (particle size distribution and mineralogy), arrangement of voids (porosity, pore size distribution, connectivity), degree of water saturation (water content), etc among others. These parameters affect the electrical resistivity, but in different ways and to different extents. The electrical resistivity and conductivity of earth materials are shown in Table 2.1.

Table 2.1: Resistivity of Rocks, minerals and industrial chemicals (Loke and Lane Jr, 2004)

| Material | Resistivity ($\Omega\cdot\text{m}$) | Conductivity (Siemens/m) |
|--------------------------------------|---------------------------------------|---|
| Igneous and Metamorphic rocks | | |
| Granite | $5 \times 10^3 - 10^6$ | $10^{-6} - 2 \times 10^{-4}$ |
| Basalt | $10^3 - 10^6$ | $10^{-6} - 10^{-3}$ |
| Slate | $6 \times 10^2 - 4 \times 10^7$ | $2.5 \times 10^{-8} - 1.7 \times 10^{-3}$ |
| Marble | $10^2 - 2.5 \times 10^8$ | $4 \times 10^{-9} - 10^{-2}$ |
| Quartzite | $10^2 - 2 \times 10^8$ | $5 \times 10^{-9} - 10^{-2}$ |
| Sedimentary rocks | | |
| Sandstone | $8 - 4 \times 10^3$ | $2.5 \times 10^{-4} - 0.125$ |
| Shale | $20 - 2 \times 10^3$ | $5 \times 10^{-4} - 0.05$ |
| Limestone | $50 - 4 \times 10^2$ | $2.5 \times 10^{-3} - 0.02$ |
| Soils and water | | |
| Clay | $1 - 100$ | $0.01 - 1$ |
| Alluvium | $10 - 100$ | $1.25 \times 10^{-3} - 0.1$ |
| Groundwater (fresh) | $10 - 100$ | $0.01 - 0.1$ |
| Sea water | 0.2 | 5 |
| Chemicals | | |
| Iron | 9.074×10^{-8} | 1.102×10^7 |
| 0.01 M Potassium chloride | 0.708 | 1.413 |
| 0.01 M Sodium chloride | 0.843 | 1.185 |
| 0.01 M Acetic acid | 6.13 | 0.163 |
| Xylene | 6.998×10^{16} | 1.429×10^{-17} |

2.3.1 Electrical Resistivity as a Function of Soil Water Content

The presence soil water in the subsurface acting as electrolytes controls electrical resistivity of the surface which is vital in porous sediments and sedimentary rocks. In these materials, their constituent minerals are less conductive than the groundwater and hence the resistivity decreases with greater amount of contained groundwater.

In addition, the resistivity is dependent upon the proportion of the rock volume that consists of pore space, the connectivity of pore space and the fraction of this volume occupied by water (Friedman, 2005). The resistivity of rock is therefore proportional to the resistivity of the dry material and the resistivity of the pore space. This is summarized in Archie's law

which states that, resistivity is inversely proportional to the fractional porosity raised to a power which varies between 1.2–1.8 based on the shape of the matrix grains (Archie, 1942; Lowrie, 2007).

The empirical formula for the resistivity of the rock, according to Archie (1942), relates to the resistivity of the water filling the pores and the volume of the pores as:

$$\rho = \frac{a\rho_w}{\phi^m S^n} \quad (2.30)$$

where porosity ϕ and saturation factor S are fractions between 0 and 1, ρ_w [Ωm^{-1}] is the resistivity of the groundwater, and the parameters a (tortuosity), m (cementation factor), and n (saturation exponent) are empirical constants that need to be determined for each case.

Generally, the accepted values for these constants are $0.5 \leq a \leq 2.5$, $1.3 \leq m \leq 2.5$ and $n \approx 2.0$ (Lowrie, 2007).

From equation (2.30), the water saturation S^n in the soil can be expressed as:

$$S^n = \frac{a\rho_w}{\rho\phi^m} \quad (2.31)$$

Unfortunately, equation (2.30) is only valid in clean porous media without considerable amount of clay (Friedman, 2005). Frohlich and Parke (1989) reported that great practical success of the law was only related to the assumed validity of the determined constants on a large range of soils except that of clayed soil. To overcome this challenge, Goyal et al. (1996) and Gupta and Hanks (1972) proposed another empirical relationship between the

resistivity and the water content as:

$$\rho_{(z,t)} = a + b\theta_{(z,t)} \quad (2.32)$$

where, a and b are empirical constants implicitly containing the soil and water characteristics which are assumed to be invariant with time. For that of clayed soil, the electrical current is not only dependent on the availability of free pore water but also by the absorbed water at the clay particle surface.

This led Rhoades et al. (1977) to introduce a new relationship which described the solid matrix resistivity as;

$$\frac{1}{\rho} = \frac{1}{\rho_w}(a\theta^2 + b\theta) + \frac{1}{\rho_s} \quad (2.33)$$

where ρ_s = solid matrix, ρ_w pore water resistivity, a and b are coefficients which depend on the solid phase characteristics related to the texture and mineralogy, and θ is the VWC (m^3m^{-3}). Kalinski and Kelly (1993) predicted the VWC with a standard error of 0.009 for water contents ranging from 0.20 to 0.50 m^3m^{-3} in soil containing 20% clay using equation (2.33). Figure 2.6 shows the laboratory calibration between the electrical resistivity and VWC for different soil types.

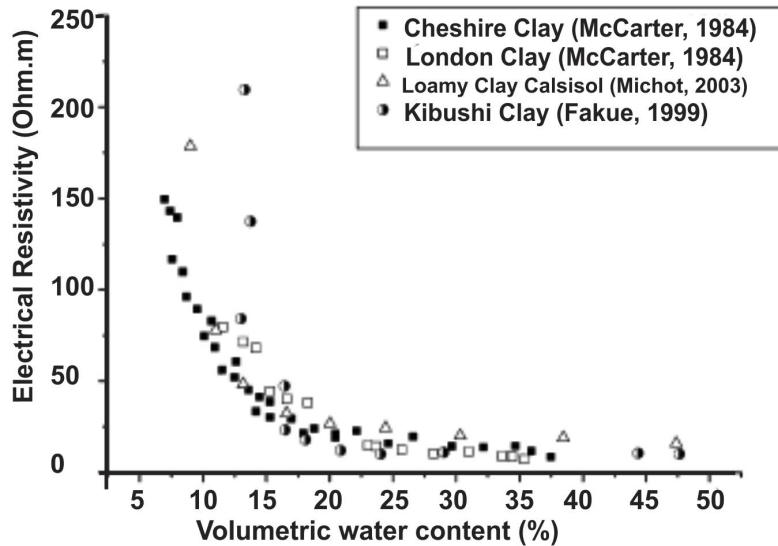


Figure 2.6: Relationship between the VWC and electrical resistivity for different soil types (obtained from Michot et al. (2003))

2.4 Depth of Current Penetration

Generally, in a homogeneous ground, the penetration of electrical current can be increased by increasing the separation of the current electrodes since flow of current tends to occur closed to the surface (Fig. 2.7). When $L = Z$, about 30% of the current flows below Z and when $L = 2Z$, about 50% of the current flows below Z (Kearey et al., 2002). In the field survey, the choice of an array is partly for their depth penetration although specific depths are difficult to define because the depth to which the current penetrates depends on the layering as well as on the separation between electrodes.

This therefore places practical limits on the depths of penetration attainable by normal resistivity methods due to the difficulty in laying long lengths of cable and the generation of sufficient power. Depths of penetration of about 1 km are the practical limit for normal equipment (Kearey et al., 2002).

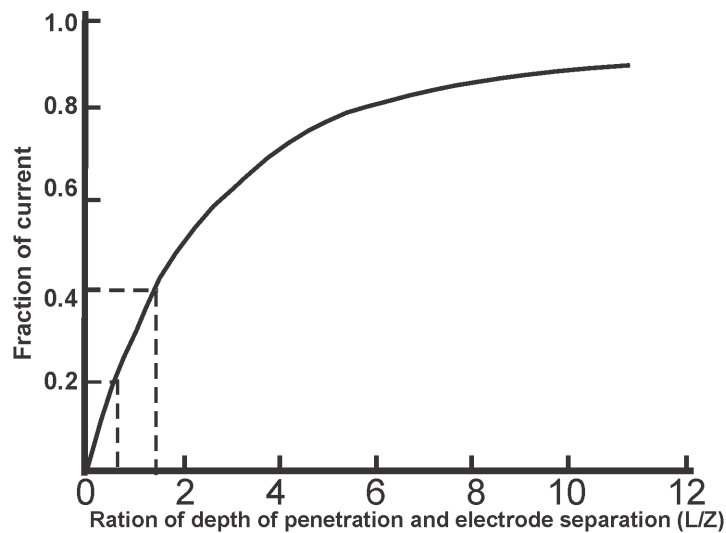


Figure 2.7: Fraction of current penetrating below a depth Z for current electrode separation L (Modified after Telford et al. (1990))

2.5 Modes of Electrical Resistivity Surveying

In practice, the two basic techniques used in electrical resistivity survey for field data acquisition are vertical electrical sounding (VES) and profiling. The VES is mostly employed for depth sounding for the purpose of determining the vertical variation of resistivity in the subsurface. The profiling, on the other hand, is for horizontal traversing (horizontal variation of resistivity) and also referred to as constant separation traversing (CST). Due to advancement in technology, another method which is known as continuous vertical electrical sounding (CVES) has become popular in recent times. It is a combined procedure which utilizes characteristics of both VES and CST to give continuous measurements.

In the case of soil science, a method which is commonly used is the time-lapse measurement and it employs the CVES technique for a 2D data acquisition enabling comparison of several data taken at different times.

2.5.1 Vertical Electrical Sounding (VES)

Vertical electrical sounding (VES) utilizes collinear arrays designed to output a 1D vertical apparent resistivity versus depth model of the subsurface at a specific observation point. In this method, a series of potential differences are acquired at successively greater electrode spacing while maintaining a fixed central reference point. This causes the current to go deeper into the subsurface to obtain information about the resistivities of the layer within the subsurface. The depth of penetration is determined by the array type and nature of each layer. Interpretation is done using RES1DINV, EarthImager and 1X1DInterpex modeling softwares or by plotting simple apparent resistivity on a log–log graph. One disadvantage of the VES method is that it does not consider horizontal variations in the layer resistivity but only with depth. However, in practical situations, the subsurface is heterogeneous and resistivity can change within a short distance laterally. The two most common arrays used for VES are the wenner and schlumberger arrays.

2.5.2 Profiling

Profiling uses collinear arrays to determine lateral variations in resistivity in the shallow subsurface at a more or less fixed depth of investigation. The current and potential electrodes are moved along the profile with constant spacing between electrodes. This gives information about horizontal variation within the subsurface but cannot detect vertical variations. Also, depth of investigation by this technique is constant and the data can be represented by a profile or contour map. Data interpretation is essentially qualitative. Dipole-dipole and pole-dipole arrays are mostly employed in CST surveys.

2.5.3 Continuous Vertical Electrical Sounding (CVES)

To obtain a better image of the subsurface requires a technique that gives information about both the lateral and vertical features. VES and CST are capable of performing either lateral or vertical measurements but not both tasks. A combination of the two (VES and CST), as in the case of CVES, can overcome this limitation to give better 2D or 3D imaging.

CVES is based on the insertion of controlled direct electrical current (DC) into the ground through electrodes. It is multi-electrode system whereby the spacing between electrodes is kept constant while the separation between the chosen potential electrodes and current electrodes varies based on the electrode configuration. The resistivity meter automatically determines the separation and which electrodes are to be used as current pair or potential pair. Based on the variation of the distances between the electrodes, the obtained apparent resistivity, either small or large, will be a property for shallow or deep volume, respectively (Fig. 2.8).

In the case in which there is limited number of electrodes and cables to extend horizontally to cover a survey length, a technique known as roll-along can be employed (Fig. 2.8b). This is done by moving the cable past one end of the line by several units of electrode spacing after a set of measurements. Measurements are normally faster than the first station because of the reduced number of data points measured as a result of data overlap and the fact that only data which do not overlap are measured.

Combining measurements of many different electrodes permutations along a line allows the calculation of 2D distribution of electrical resistivity at this transect. The patterns of the resistivity in the soil result from lithology, porosity, structure, temperature, root density and water content (Lowrie, 2007).

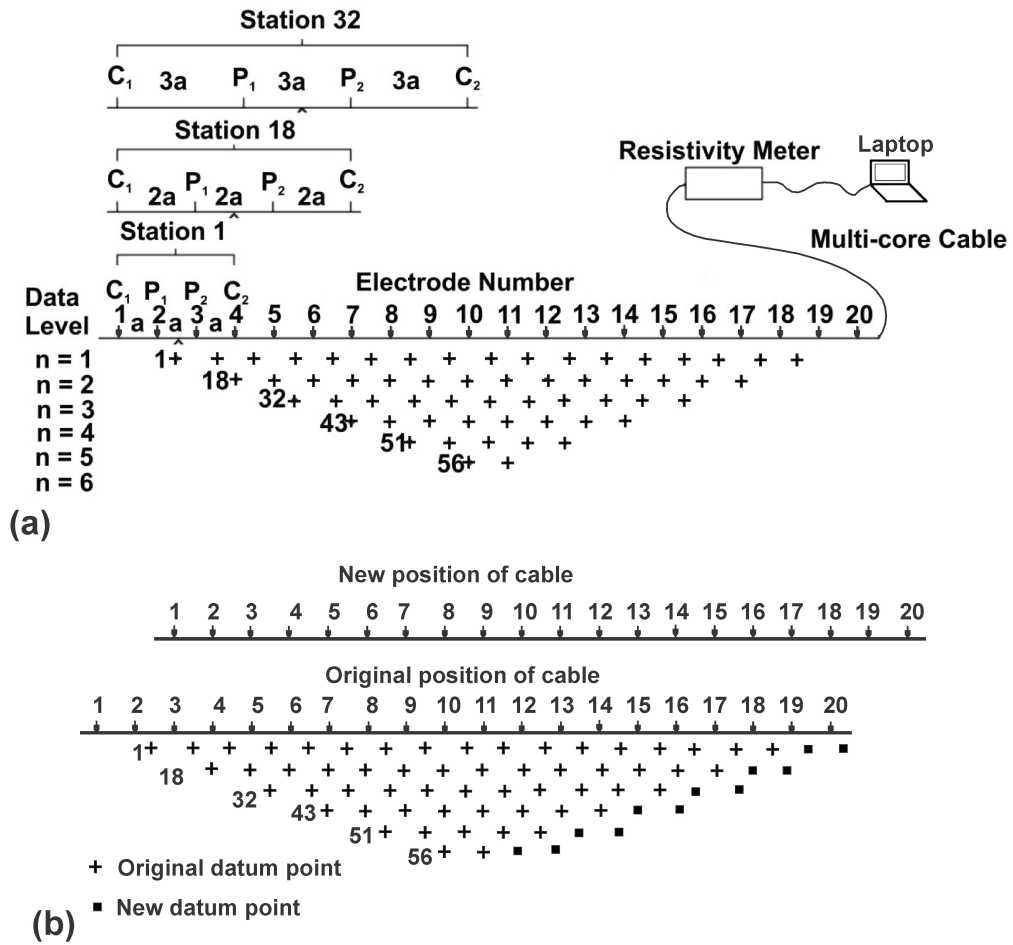


Figure 2.8: (a) Arrangement of electrodes for 2D electrical survey and the sequence of measurements used to build up a pseudosection (b) Roll-along technique to cover more area (Loke, 2001)

2.5.4 Time-lapse CVES Measurement

CVES measurements can be obtained at different time scales for comparison. This allows for the filtering of the signal by stationary characteristics of the soil and therefore highlights changes in soil moisture content (Nijland et al., 2010). Among the factors which influence the electrical resistivity of the subsurface, moisture content is considered as one of the most significant, varying frequently from time to time. It is therefore possible to use CVES measurements taken at different times for soil water content mapping. In addition, within

the investigated time frame of measurements, subsurface may also vary due to temperature changes which have been proposed to be about 2.2% per 1 °C (Friedman, 2005). Bottraud et al. (1984) pointed out that, a stable temperature can be assumed since measurement is done every day at the same time over a short period.

The moisture distribution is more easily determined by plotting the percentage in the subsurface resistivity of the inversion models for the data sets taken at different times, when compared with the initial model. Inversion of the data sets is then carried using a joint inversion technique, where the model obtained from the initial data set is used to constrain the inversion of the later time data sets (Loke, 1999).

2.6 Theoretical Background of Ground Penetrating Radar (GPR)

Ground Penetrating Radar (GPR) operates by generation of broadband electromagnetic waves by a transducer and the pulses are emitted into the ground by a transmitter. As the wave travels through the ground, it is reflected, deflected and absorbed at interfaces between materials of dissimilar dielectric constants. The signal that returns to the surface is then picked up by a receiver in the antenna which is processed by the radar unit. The change of amplitude between the transmitted and received signals is based on the conductivity and dielectric properties of the reflector.

2.6.1 Fundamentals of Electromagnetic Wave

Maxwell's equations are used to describe the relationship that exists between electric and magnetic fields and how they propagate in space. The four basic equations that formed Maxwell equations are Faraday's law (Eqn. 2.34), Ampere's law (Eqn. 2.35), Gauss's law for electric field (Eqn. 2.36) and Gauss's law for magnetic flux density (Eqn. 2.37).

$$\nabla \times \mathbf{E} = -\frac{\partial(\mathbf{B})}{\partial(t)} \quad (2.34)$$

$$\nabla \times \mathbf{H} = \mathbf{J} + \frac{\partial(\mathbf{D})}{\partial(t)} \quad (2.35)$$

$$\nabla \cdot \mathbf{D} = q \quad (2.36)$$

$$\nabla \cdot \mathbf{B} = 0 \quad (2.37)$$

where \mathbf{E} is the electric field strength vector [Vm^{-1}], \mathbf{H} is the magnetic field intensity vector [Am^{-1}], $\mathbf{J} = \sigma\mathbf{E}$ is the electric current density vector (flux) in [Am^{-2}], $\mathbf{D} = \varepsilon\mathbf{E}$ is the electric displacement current vector in [Cm^{-2}], $\mathbf{B} = \mu\mathbf{H}$ is the magnetic flux density vector [Tm^{-2}], q is the electric charge density [Cm^{-3}], t is time (s), σ is electrical conductivity, ε is the magnetic permittivity, μ is the permeability and ∇ is the spatial vector derivative operator. From the equations (2.34) – (2.37), the electromagnetic wave equation for the electric field and magnetic field can be written as:

$$\nabla^2 \mathbf{E} - \mu\varepsilon \frac{\partial^2 \mathbf{E}}{\partial t^2} - \mu\sigma \frac{\partial \mathbf{E}}{\partial t} = 0 \quad (2.38)$$

$$\nabla^2 \mathbf{B} - \mu\varepsilon \frac{\partial^2 \mathbf{B}}{\partial t^2} - \mu\sigma \frac{\partial \mathbf{B}}{\partial t} = 0 \quad (2.39)$$

In the electromagnetic theory, the electric and magnetic fields depend on each other. At all times, the electric field, magnetic field and their direction of propagation are always perpendicular to each other to form a right-handed orthogonal set.

The pointing vector \mathbf{P} , which gives the direction of propagation is equal to the local energy flow per unit area (Mala, 2001) and can be expressed as:

$$\mathbf{P} = \mathbf{E} \times \mathbf{B} \quad (2.40)$$

The vector amplitudes of \mathbf{E} and \mathbf{B} contain both real and complex values. Real values of \mathbf{E} and \mathbf{B} are obtained when the wave is linearly polarized and complex vector amplitudes are obtained when propagation is elliptically polarized.

Now, considering a single-frequency, linearly polarized, EM plane wave travelling in the z direction; from Maxwell's equations, the following expressions for the complex electric \mathbf{E} and magnetic \mathbf{B} field vectors are derived (Knight, 2001);

$$\mathbf{E}(z, t) = \mathbf{E}(Z)e^{-i\omega t} \quad (2.41)$$

Substituting equation (2.41) into equation (2.38) and rearranging to obtain Helmholtz equation describing the plane wave harmonic solution:

$$\nabla^2 \mathbf{E} + K^2 \mathbf{E} = 0 \quad (2.42)$$

The propagation constant, K , is given as:

$$K^2 = \omega^2 \mu \epsilon + i\omega \mu \sigma \quad (2.43)$$

where, the symbols have their usual meaning and the $\sqrt{K^2} = k$. The solution to equation (2.43) is given as:

$$E = E_0 e^{-i(\omega t - kz)} \quad (2.44)$$

and

$$k = a + ib \quad (2.45)$$

where, a = phase coefficient and b = attenuation coefficient. Substituting equation (2.45) into (2.44):

$$E = E_0 e^{-i(\omega t - az)} e^{-bz} \quad (2.46)$$

The above equation contains two parts, first exponential expresses an unattenuated wave propagation whilst the second exponential accounts for an attenuated wave with depth z .

Also, the general expression for a harmonic wave travelling in the z direction with a phase velocity v is given as:

$$a = a_0 e^{-i\omega(t - \frac{z}{v})} \quad (2.47)$$

Comparing the first exponential part of equation (2.46) with that of equation (2.47), the phase velocity of the electromagnetic wave can be expressed as:

$$v = \frac{\omega}{a} \quad (2.48)$$

And the phase coefficient a , and the attenuation coefficient b is given as:

$$a = \omega \sqrt{\mu\epsilon \left(\frac{1 + \sqrt{1 + (\sigma/\omega\epsilon)^2}}{2} \right)} \quad (2.49)$$

$$b = \omega \sqrt{\mu\epsilon \left(\frac{1 - \sqrt{1 + (\sigma/\omega\epsilon)^2}}{2} \right)} \quad (2.50)$$

where σ is the conductivity, $\epsilon = \epsilon_0\epsilon_r$ is dielectric permittivity, $\mu = \mu_0\mu_r$ is the magnetic permeability, ϵ_r is the relative dielectric permittivity and μ_r the relative magnetic permeability and the $(\sigma/\omega\epsilon)$ is the material loss tangent, $\tan(\delta)$ of the medium.

From equation (2.44), the velocity is then expressed as:

$$v = \frac{1}{\sqrt{\mu_0\epsilon_0}} \frac{1}{\sqrt{\mu\epsilon \left(\frac{1 + \sqrt{1 + (\sigma/\omega\epsilon)^2}}{2} \right)}} \quad (2.51)$$

However, the speed of light in vacuum, c is given as;

$$c = \frac{1}{\sqrt{\mu_0\epsilon_0}}$$

Hence, the velocity $v(\omega)$ can be expressed as:

$$v = \frac{c}{\sqrt{\mu\epsilon \left(\frac{1 + \sqrt{1 + (\sigma/\omega\epsilon)^2}}{2} \right)}} \quad (2.52)$$

where $c = 3 \times 10^8 \text{ ms}^{-2}$, the relative permittivity ϵ_r is the ratio of the permittivity of ϵ of the host medium to the permittivity of free space $\epsilon_0 = 8.854 \times 10^{-12} \text{ Fm}^{-1}$, μ_r is the ratio of the magnetic permeability of the host medium $\mu \text{ (NA}^{-2}\text{)}$ relative to that of free space $\mu_0 = 4\pi \times 10^{-7} \text{ NA}^{-2}$, $\sigma/\omega\epsilon$ is the material loss tangent, $\omega = 2\pi f$ and f is the linear frequency. Davis and Annan (1989) proposed that, in a low-loss medium, $(\sigma < 0.1 \text{ Sm}^{-1})$ and over a frequency range of 0.01–1 GHz, the influence σ is negligibly small with $\sigma/\omega\epsilon \ll 1$. It is also negligible for non-magnetic materials at radar frequencies where $\mu_r = 1$ (Daniels,

1996).

The radar velocity $v(\omega)$ and the attenuation of the wave are practically independent of the angular frequency ω when all these conditions are satisfied and hence equation (2.52) can be written as:

$$v = \frac{c}{\sqrt{\epsilon_r}} \quad (2.53)$$

And, that of the attenuation of the wave B in dBm^{-1} is expressed as;

$$B = 1636 \frac{\sigma}{\epsilon_r} \quad (2.54)$$

From equation (2.53), it is evident that the velocity of an electromagnetic wave in a low loss medium is mainly controlled by the relative dielectric permittivity. For that of water, the value of ϵ_r is about 80 (in the MHz–GHz frequency range) and that of air is 1 while that of most common geological materials lies in the range of 3–10 (Davis and Annan, 1989; Daniels, 1996). The large permittivity contrasts within this frequency range permit the application of electromagnetic methods in determining the VWC. The soil water content can be estimated by empirical relationship developed by (Topp et al., 1980). The third-degree polynomial of the Topp equation which was used in the calculation of the VWC in this work is given as:

$$\theta_v = -5.3 \times 10^{-2} + 2.92 \times 10^{-2} \epsilon_r - 5.5 \times 10^{-4} \epsilon_r^2 + 4.3 \times 10^{-6} \epsilon_r^3 \quad (2.55)$$

where, θ_v is the VWC and ϵ_r is the relative dielectric permittivity.

By determining the length of the travel path of an electromagnetic wave-front and estimating its velocity from the two-way travel time (TWTT) of the reflected wave, equation (2.55) can be used to retrieve the volumetric water of the soil.

2.6.2 Reflection of Electromagnetic Waves

The reflection strength of an electromagnetic wave incident normally in a medium depends on the magnitude of change in the electrical and magnetic properties. If we assume that there is a low-loss non magnetic medium, the reflection coefficient R is expressed as:

$$R = \frac{Z_2 - Z_1}{Z_2 + Z_1} = \frac{\sqrt{\epsilon_{r1}} + \sqrt{\epsilon_{r2}}}{\sqrt{\epsilon_{r1}} - \sqrt{\epsilon_{r2}}} = \frac{v_2 - v_1}{v_2 + v_1} \quad (2.56)$$

where Z_1, Z_2 , $\epsilon_{r1}, \epsilon_{r2}$ and v_1, v_2 are respectively the impedances, the relative dielectric permittivities and the velocities of soil layers 1 and 2 immediately above and below the discontinuity $Z = \sqrt{\mu_0/\epsilon_0\epsilon_r}$. R determines how sharp a boundary reflection might be. A sudden change in ϵ_r with depth gives a sharp reflection signal, whereas pulse widening results from a gradual change in ϵ_r . From equation (2.56), it is clear that the phase of the electromagnetic wave at a boundary remains unaltered when $v_2 > v_1$. However, a phase shift of 180 °C occurs when $v_2 < v_1$. In all cases, R has values between +1 and -1.

2.6.3 Dielectric Coefficient of Geological Materials

The dielectric coefficient is a measure of the extent to which a material traversed by an electromagnetic field becomes polarized and it describes the frequency response of the material (Preko, 2007). It depends upon the physical properties of the material which includes shape and size of the sample, humidity, temperature, frequency and the field of measurements. This means that an electromagnetic wave packet is dispersed due to the frequency dependence of the phase velocity of its spectral components as it propagates through the medium. The dielectric coefficient is complex but Schmugge (1985) pointed out

that, for many materials of geological relevance, only the real part of the dielectric coefficient is of practical importance.

The real part is expressed as:

$$\varepsilon_r = \frac{\varepsilon_{ef}}{\varepsilon_0} \quad (2.57)$$

And it is related to the radar wave velocity as:

$$\varepsilon_r = \frac{c^2}{v^2} \quad (2.58)$$

where ε_{ef} is the effective permittivity of the medium and c is the speed of light in vacuum.

The dielectric coefficient is a function of the composition of porous granular materials as well as the amount of water within it. In addition, its values help in interpreting GPR soil data. Table 2.2 shows the dielectric coefficients of most geological materials.

Table 2.2: Materials attenuation and relative permittivity measured at 100 MHz (Daniels, 1996)

| Material | Attenuation (dBm ⁻¹) | Relative permittivity (ϵ_r) |
|------------------|----------------------------------|--|
| Air | 0 | 1 |
| Asphalt: dry | 2 – 5 | 2 – 4 |
| Asphalt: wet | 2 – 20 | 6 – 12 |
| Clay | 10 – 100 | 2 – 40 |
| Coal: dry | 1 – 10 | 3.5 – 9 |
| Coal: wet | 2 – 20 | 8 – 25 |
| Concrete: dry | 2 – 12 | 4 – 10 |
| Fresh water | 0.1 | 80 |
| Fresh water ice | 0.1 – 2 | 4 |
| Granite: dry | 0.5 – 3 | 5 |
| Granite: wet | 2 – 5 | 7 |
| Limestone: dry | 0.5 – 10 | 7 |
| Limestone: wet | 10 – 25 | 8 |
| Permafrost | 0.1 – 5 | 4 – 8 |
| Rock Salt: dry | 0.01 – 1 | 4 – 7 |
| Sand: dry | 0.01 – 1 | 4 – 6 |
| Sand: saturated | 0.03 – 0.3 | 10 – 30 |
| Sand stone: dry | 2 – 10 | 2 – 3 |
| Sand stone: wet | 10 – 20 | 5 – 10 |
| Seawater | 1000 | 81 |
| Seawater ice | 10 – 30 | 4 – 8 |
| Shale: saturated | 10 – 100 | 6 – 9 |
| Soil: firm | 0.1 – 2 | 8 – 12 |
| Soil: sandy dry | 0.1 – 2 | 4 – 6 |
| Soil: sandy wet | 1 – 5 | 15 – 30 |
| Soil: loamy dry | 0.5 – 3 | 4 – 6 |
| Soil: loamy wet | 1 – 6 | 10 – 20 |
| Soil: clayed dry | 0.3 – 3 | 4 – 6 |
| Soil: clayed wet | 5 – 30 | 10 – 15 |

2.6.4 The Guided Wave Method

The propagation of GPR signal through soil is mainly controlled by electrical properties such as electric conductivity σ , the dielectric permittivity $\epsilon = \epsilon_0 \epsilon_r$ and the magnetic permeability $\mu = \mu_0 \mu_r$, where ϵ_r is the relative dielectric permittivity and μ_r is the relative magnetic

permeability.

In TDR and GPR applications, the guided waves propagate with the phase velocity of the free electromagnetic wave in the medium surrounding the wave guide. Preko and Wilhelm (2012) explored the validity of this assumption by analyzing the propagation velocity of the guided waves using cylindrical soil model with a metal rod of radius a in its centre (Fig. 2.9).

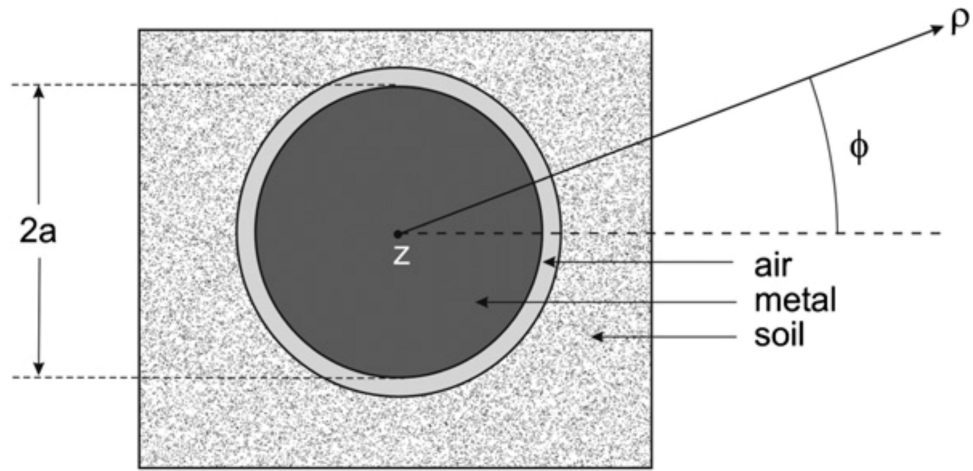


Figure 2.9: Cylindrical soil model with a metal rod of radius a at the centre surrounded by a thin packet of air (Preko and Wilhelm, 2012)

Preko and Wilhelm (2012) showed that, the phase velocity of the guided wave ω/α , the phase velocity of free wave in the outer region, $\omega/Re(k_a)$ and the velocity used in TDR applications $c/\sqrt{\epsilon_a}$ remain practically identical for the conductivity range $\sigma_a < 1 \text{ Sm}^{-1}$ and that of the propagation $1/\beta$ width decreases for increasing conductivity σ_a (Table 2.3). Hence, it is practically accepted to determine the dielectric permittivity of the host medium as done in the case of TDR.

Table 2.3: Attenuation effects of the electromagnetic wave propagation for different conductivities of the embedding dielectric (Preko and Wilhelm, 2012)

| σ_a (Sm ⁻¹) | $\frac{Re(k_a)}{\alpha} - 1$ | $\frac{\nu_{ph} \sqrt{\epsilon_a}}{c} - 1$ | $\frac{1}{\beta}$ (m) |
|--------------------------------|------------------------------|--|-----------------------|
| 1×10^{-3} | -1.91×10^{-5} | -2.61×10^{-5} | 15.9 |
| 3×10^{-2} | -1.99×10^{-5} | -2.11×10^{-3} | 0.531 |
| 5×10^{-2} | -2.04×10^{-5} | -4.93×10^{-3} | 0.320 |
| 0.1 | -2.16×10^{-5} | -1.87×10^{-2} | 0.162 |
| 0.5 | -2.43×10^{-5} | -2.14×10^{-1} | 0.0405 |
| 1 | -2.98×10^{-5} | -3.75×10^{-1} | 0.0255 |

NB: The conductivity of the cylindrical conductor $\sigma_i = 10^7$ Sm⁻¹, radius $a = 0.02$ m, radar frequency $f = 5 \times 10^8$ Hz, $\epsilon_i = 1$ Fm⁻¹, $\epsilon_a = 9$ Fm⁻¹, $k_i^2 = \frac{\epsilon_i \omega^2}{c^2} + i\omega\mu_0\sigma_i$ and $k_a^2 = \frac{\epsilon_a \omega^2}{c^2} + i\omega\mu_0\sigma_a$.

2.7 Summary of Background to Methods

This chapter outlines the main fundamental theories behind electrical resistivity method and ground penetrating radar. The Continuous Vertical Electrical Sounding (CVES) of the electrical method which is based on Ohm's law measures the apparent resistivity of the soil which is controlled largely by the soil moisture content. Variations in the apparent resistivity of the soil therefore indirectly suggests variations in soil moisture content. For the GWS technique of the GPR, the dielectric permittivities of the medium obtained can be inverted into the soil moisture content by using an appropriate model such as the Topp's model (Topp et al., 1980). It is therefore possible to determine the soil moisture variations.

CHAPTER 3

MATERIALS AND METHODS

3.1 Project Site Description

The site for this research work is located at KNUST Agricultural Research Station (ARS)–Anwomaso, Kumasi. It is about 10 km from the main University campus and has a total land area of about 555 (ha). Most of the land is suitable for livestock/crop production, fish farming, etc though only about 10% of the arable land is developed into oil palm and citrus plantations. The station shares its boundaries with Anwomaso, Domiabra, Kwamo, Fumesua and Bebre settlements (Fig. 3.1a).

The main area where the monitoring of the water content was done is a maize farm centered on latitude 6°41'838" N and longitude 1°31'533" W. The land is used for monitoring maize growth by the College of Agriculture, KNUST, and therefore was very suitable for carrying out this research. It was divided into four plots based on the different land preparation modes which includes Ploughed-Harrowed, Ploughed, Hoed and No-till (Fig. 3.1b). Also, each of these four plots have been subdivided into four parts based on the land treatment such as No Fertilizer, 1/2 Poultry Manure + 1/2 NPK, 100% Poultry Manure and 100% NPK (Fig. 3.1b) respectively. Four profiles were then laid on each of the different fields with the subdivision 'No Fertilizer' for the measurement. The length of each profile was 8 m but the inter-profile separation was variable due to 'No Fertilizer' location. At the end of the plots, run off gutters

were dug for monitoring water run-off from the fields but were rather incomplete due to lack of funds. A local rain gauge (made of a cylindrical rubber) was also mounted at the eastern side of the field for measuring rainfall (Fig. 3.1b).

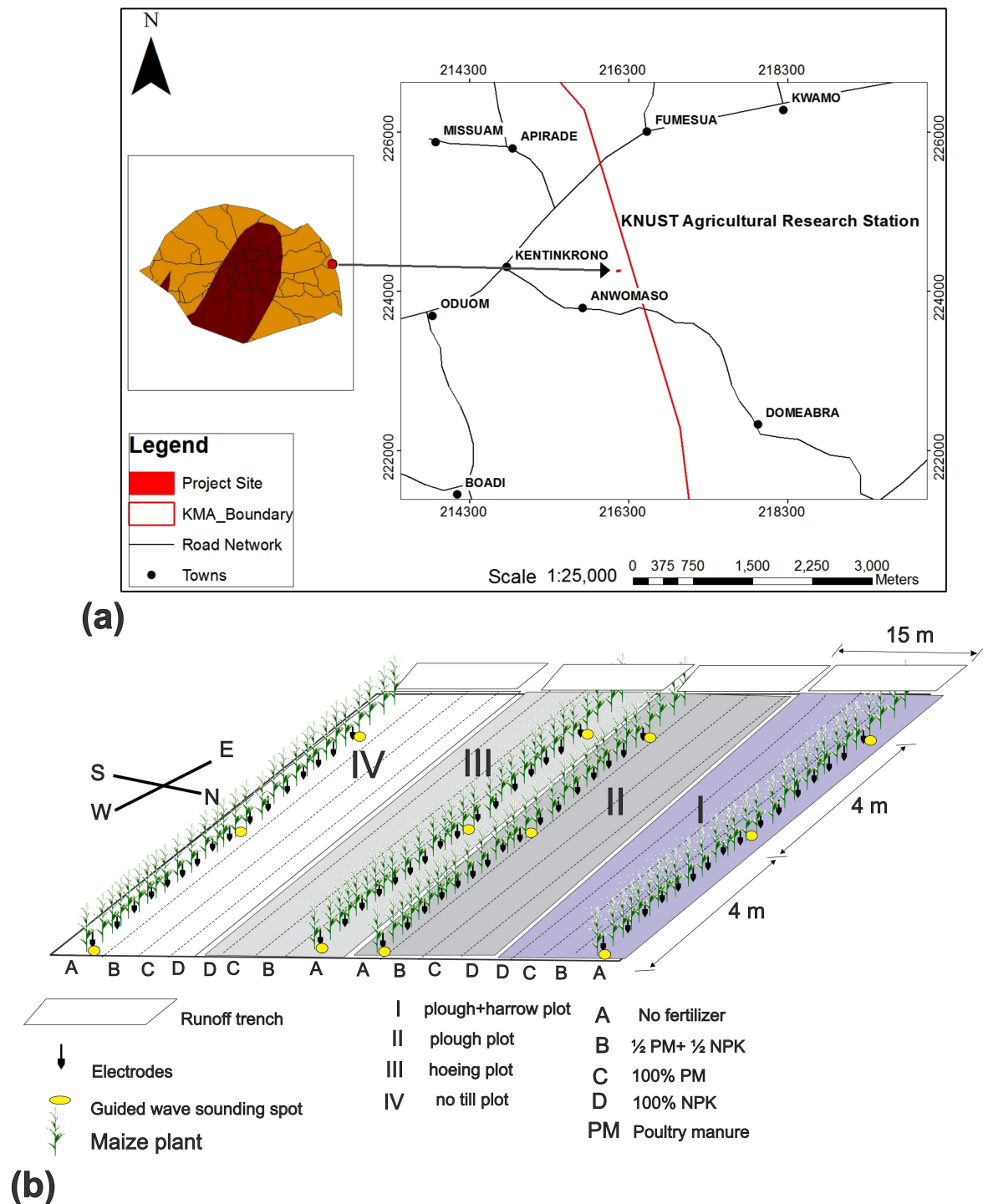


Figure 3.1: (a) Project Site (b) Layout of Survey Profiles at the site

3.1.1 Geological Setting of the Project Area

This research was undertaken at the KNUST Agricultural Research Station (ARS), Anwomaso – Kumasi. The area is within the Kumasi metropolis in Ghana and centered on latitude 6°41'838" N and longitude 1°31'533" W. The Kumasi metropolis is composed mainly of middle Precambrian rocks and forms part of the Eburnean Plutonic Suite. These were formed approximately within the upper and lower age 2.172 and 2.116 million years ago (Andrews et al., 2013). The Precambrian rocks and Eburnean Plutonic suite also composed of biotite granite and minor granodiorite and K–feldspar porphyritic rocks (Fig. 3.2).

The Birimian sequences in the area are portrayed by a transition in the sedimentary facies from the centre of the basin; there is a thick sequence of dark grey to black argillites which are interbedded with subordinate silica-clastic metasediments. The argillites grade laterally away from the basin centre into a thick sequence of interbedded argillite/volcaniclastic units and to volcanoclastics interbedded with subordinate argillites, talus and volcanic. There is the occurrence of narrow belt of about 3 km wide underlain by interbedded volcanoclastic and coarse arenaceous sediments such as greywackes, arkose, conglomerate, quartzite among others (Moon, 1962).

The Kumasi granitoid complex (Kesse, 1972) dominates much of the basin area and contains large roof pendants of metasedimentary schists. This massive intrusive complex is basin–type granitoid, which ranges in composition from intermediate (granodiorite/tonallite) to more felsic (granite) phases. The very existence of the Precambrian rock has led to the development of the construction industry in the metropolis.

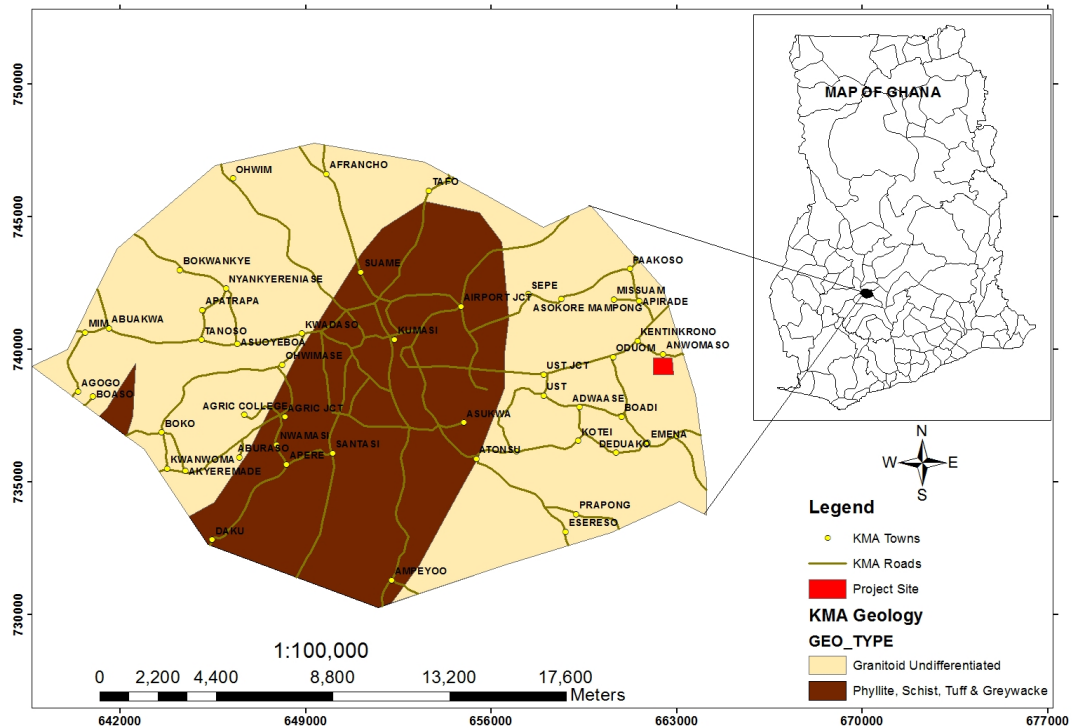


Figure 3.2: Geological map of Kumasi Metropolis showing the study area in red (Ghana, Geological Survey, 2009)

3.1.2 Major Soil Types

Local classification of soils in Ghana is based on the major soil climatic differences that in turn have given rise to two major distinct vegetation belts, namely, Forest and Savannah (Obeng, 2000). The Kumasi Metropolis falls under the Forest Belts and the major soil type is the Forest Ochrosol. This type of soil has high accumulation of organic matter in the surface horizon due to the abundant leaf-fall from vegetation cover and also the slower rate at which humus is being oxidised. They consist principally of weathering products of metamorphosed and basic intrusive rocks, principally, granites, phyllites, quartzites, sandstones and epidiorites, greenstones, basalt and Upper Birimian phyllites. The study site is therefore highly dominated by sandy-loam soil which is very suitable for plants growth. Such soils, under natural conditions, contain adequate nutrients that are tied-up with the

organic layers in their topsoils. They can, therefore, sustain good crop growth.

3.1.3 Location and Accessibility

Accessibility in the Kumasi Metropolis is very good with all major towns and villages connected by an extensive network of paved and dirt roads as well as footpaths and tracks. The project site shared boundaries with Anwomaso, Domiabra, Kwamo, Fumesua and Bebre. A tarred road branches from the main Kumasi – Accra road through the Anwomaso township to the easting side closed to the entrance of the station. This has made the station easily accessible for both researchers and workers of the University community. The plot where the four profiles were located were monitored daily for weeds, animals, rainfall, thieves etc and there was no need for clearing of profiles lines hence geophysical work was easily carried out without hindrance.

3.1.4 Physiography

The Kumasi Metropolis as indicated by Griffis et al. (2002) is characterized by dissected plateau, probably representing a mid to late Tertiary peneplain, with elevations in the range 225 – 300 m above mean sea level. There are also a number of rounded and flat-topped hills that crest at elevations of 400 – 460 m above sea level which appears to represent an earlier (mid to early Tertiary) regional erosional surface (Griffis et al., 2002). Most of the area is covered by secondary forest and cultivated farms, which are widespread due to the relatively dense population. Due to the small size of the project site, the topographic changes were so small that it was considered as flat land.

3.1.5 Climatic Conditions and Vegetation

The Kumasi Metropolis falls under the sub-equatorial type. Most of the area is covered by secondary forest and cultivated farms, which are widespread due to the relatively dense population. The annual rainfall is generally in the 1500 – 2000 mm range and falls in the main wet season (March – July) and minor wet season (September – November). Daily high temperatures are common in the low to mid 30s whereas the lows are usually in the mid 20s (Griffis et al., 2002). The predominant species of trees found are *Ceiba*, *Triplochlon*, *Celtic*, with exotic species. The rich soil has also promoted agriculture in the periphery. In addition to its scenic beauty as tourist centre, the Kumasi Metropolis has aided in wild life preservation like the Kumasi Zoological and KNUST Botanical Gardens. Apart from these, the area is dominated by patches of vegetation cover scattered over the peri-urban areas of the metropolis. However, the erratic nature of rainfall in the country as well as the Metropolis and high population growth has led to research into sustainable agricultural practices such as irrigation management to ensure all year round crop production.

3.2 Materials and Equipment used for Data Collection

The materials used in this project include:

The ABEM LUND Imaging system.

Improvised Electrodes.

The RAMAC GPR System.

Access Tubes and Wave guide.

3.2.1 The ABEM LUND Imaging system

The equipment used for the electrical resistivity data collection was ABEM LUND Imaging System which includes the Terrameter SAS4000. The ABEM LUND is an automatic electric imaging system, suited for automatic continuous resistivity profiling as well as sounding. It is a state-of-the-art data acquisition instrument with inbuilt Lund Imaging System which can be used for electrical resistivity, self potential and induced polarization surveys.

In addition to the Terrameter SAS400 and electrode selector, the setup for geoelectrical survey includes car battery, improvised electrodes, tape measure, cable joints, cable jumpers, hammer and the pegs (Fig. 3.3).



Figure 3.3: Set of Terrameter for CVES measurement (a) Drum (b) Terrameter (c) Selector (d) Battery (e) Jumper (f) Cable (g) Stand

3.2.1.1 Modification of Electrodes/Improved Electrodes

The ABEM LUND imaging system consists of steel electrodes and four cables which are usually used for measurement. The four cables measured about 40 m in length and each had 21 cable take-out. For the nature of this work, these steel electrodes were not used since they

have to be left at the mercy of rainfall and thieves during the three month period of study.

To overcome this challenge, 400 improvised electrodes were made for this project. Copper wires were cut into 25 cm in length and the rubber covers were peeled off. These copper wires were then bend (1 cm in length) at two places separated by a distance of 6 cm (Fig. 3.4). Also, several pieces of wood (hard wood) were also cut at 20 cm in length and one of the ends were sharpened pointed (pointed portion is 2 cm) in order to be easily driven into the soil. Two holes separated by a distance of 6 cm were then created at 12 cm from the pointed edge of the wood. The thickness of the wood was about 1 cm for all sizes (Fig. 3.4).

With the help of pliers, the copper wires were then wrapped around the wood with the bent part passing through the two holes created while allowing parts to extend beyond the wood to about 3 cm from the top.

The copper wires served as the conducting medium for the current as well as the potentials and the wood helped to support the wires in the ground. At the end of the design, a complete set of 400 improvised electrodes (Fig. 3.4) were obtained for the measurement.

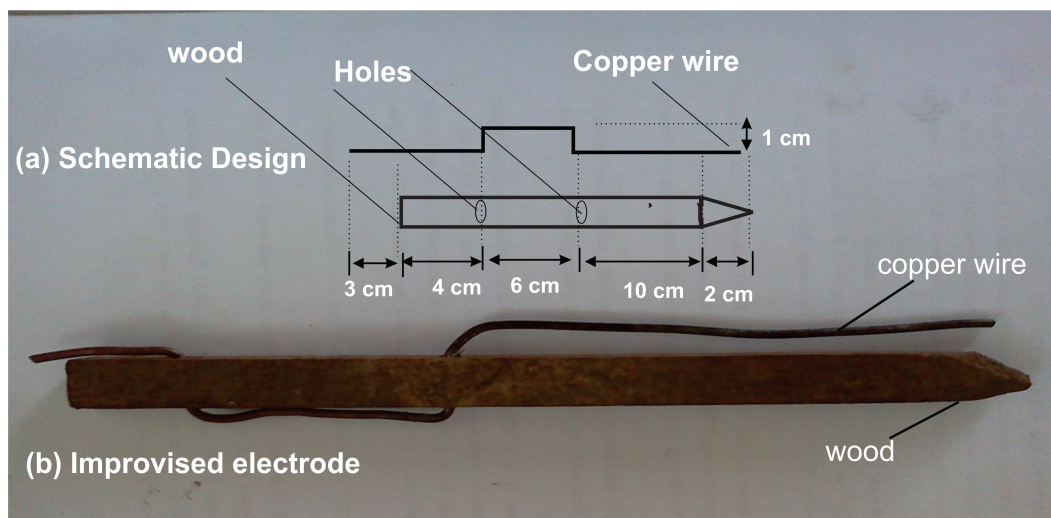


Figure 3.4: (a) Schematic design of electrode (b) Improvised electrode

3.2.2 The RAMAC GPR System

The RAMAC GPR system (Fig. 3.5) made by the MALA Company was used for this work. The system comprises the MALA ProEX control unit, the XV monitor and antenna unit. The XV monitor is powered by a 12 V standard Li-Ion Batteries. A shielded monostatic antenna of central frequency of 800 MHz was used for the measurements. This antenna was chosen because of its high near surface resolution. Moreover, the shielded nature of it prevents the radar waves from scattering hence much of it can be focused on the target.



Figure 3.5: MALA GPR System (a) 800 MHz Shielded antenna (b) XV Monitor (c) MALA ProEX control unit

3.2.3 Access Tubes and Wave Guide

Apart from RAMAC GPR System, twelve (12) access tubes and a metal wave guide were also used. The access tubes were cut from PVC pipes of equal length of about 0.80 m

and 0.022 m external diameter (Fig. 3.6a). For that of the wave guide, a hollow metal rod graduated with holes at 0.01 m separation, 1.0 m in length and an external diameter of 0.020 m was used (Fig. 3.6b). As the name suggests, the PVC tubes served as access for the metal rod and the metal rod served as a guide for the propagating electromagnetic waves emitted from the GPR transmitter (Fig. 3.6).



Figure 3.6: (a) PVC pipes (b) Metal rod

3.3 Data Acquisition

Two integrated techniques were employed in data collection in this research work. These included Continuous Vertical Electrical Sounding (CVES) and Guided Wave Sounding (GWS) techniques. The field measurement lasted approximately three months starting from 10th June, 2013 and ending on 16th August, 2013. This coincided with growing stages of the maize (i.e. from the vegetative stage, through reproductive up to harvesting of the maize). Data were taken on each day except on weekends.

For the CVES technique, four profiles were traversed each day on the field for the whole period and each profile had 36 data points, thus totaling 142 data sections. In the case of the GWS, three stations were located on each of the four profiles totaling up to 12 stations in all. Data were continuously taken for twelve (12) days for each station from the 22nd July, 2013 to 23rd August, 2013. This brought the number of data for the GWS to 144 for all the twelve holes.

Finally, the height of selected maize plants was also recorded on weekly basis whilst rainfall information was noted. The purpose of these measurements was to help in the data interpretation.

3.3.1 Reconnaissance Survey

Before the main geophysical work was carried out, a desk study and reconnaissance visit were carried out to have prior information about the study areas. Among the factors that were considered include accessibility, cost, suitable locations, survey length, protocols, period to carry out the study etc. The Agricultural Research Station was therefore not chosen on mere coincidence but rather after carefully satisfying most of the conditions. First and foremost, accessibility was not a problem since the stations had a major road. Also, the chosen field (Maize) was a project field for a doctoral student, hence special care was given to the maize plants. It was also possible to easily obtain information such as soil type in the field, rainfall data, and maize type among others. Finally, the project pioneered partnership between the Faculty of Agriculture and the Physics Department of the KNUST – Kumasi in a collaborative research work.

3.3.2 Data Acquisition Using ABEM Terrameter

The multi-electrode ABEM Lund resistivity imaging system was used to carry out the electrical resistivity measurements on four profiles located on the maize farm at the ARS. The four profiles were of equal length of 8 m (Fig. 3.1b). The system operated automatically to build up a pseudo-section once the geometrical parameters (array type, electrode separation and minimum current) were set (Fig. 3.7).

For the first data point, electrodes 1, 2, 3 and 4 were used where 1,4 and 2,3 were used as the current and potential electrodes respectively. The second data point was achieved by using 2 and 5 as current electrodes and 3 and 4 as potential electrode. This is repeated along the traverse until all electrodes were used. When this is done, a new level with electrode separation '2a' was used. Here, the first data point used electrode 1, 7 as current electrodes and then 3, 5 as potential electrodes. Other levels were built up using electrode separation of '3a', '4a', '5a' and '6a' (Fig. 3.7).

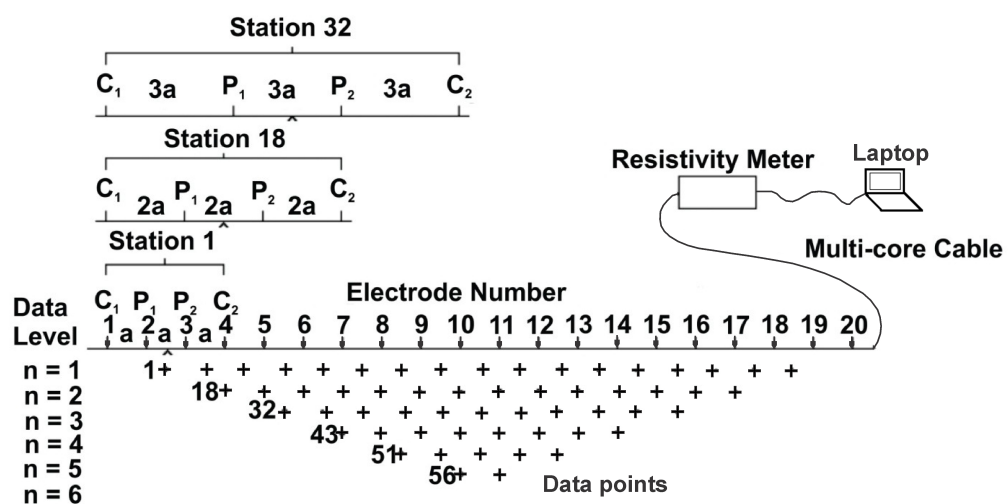


Figure 3.7: Sketch of the electrodes for the 2D electrical resistivity survey and sequence of measurements for building the pseudo-section (Loke, 2001)

The WEN32SX wenner array protocol, using 41 electrodes connected to two 40 m long multi-core cables with electrode separation of 0.2 m was used for the measurements. The 41 specially designed electrodes were driven gently into the ground close to the maize plants with the help of a small hammer in all the four profiles. Each of the electrodes was then numbered according to its take-out with a permanent pen marker. This made the connection of the jumpers very fast and helped avoid skipping of electrodes. The cables were laid and the jumpers were connected from the copper part of the electrodes to their respective cable take-outs (Fig. 3.8b). All the electrode take-outs were connected in the WEN32SX protocol. Each electrode position is uniquely identified at a take-out on the cable which helped in identifying the required current and potential pairs during the measurement at various data levels (Aning et al., 2014). The resistivity meter automatically switched the electrodes on to serve as current or potential pairs. The selection of the protocols and the other inputs were done prior to going to the field.

The ABEM terrameter, the electrode selector ES 10–64C and the 12 V car battery were then connected between cables 1 and 2 of the set-up. The electrode resistance test was run first before the measurements to ensure that all the 41 electrodes were connected and conducting. In some cases the electrode test failed and a small amount of water had to be poured under those electrodes and they were hammered deeper to ensure better conductive coupling with the ground.

When measurement for the first profile was completed, the terrameter, the electrode selector ES 10-64C, the 12 V car battery and jumpers were then moved quickly to the second profile. The procedure described for the first set of measurements was repeated to acquire the data for all the four profiles.

It is worth pointing out that the electrodes on each profile in the farm were maintained at the same position and measurements were taken using the same protocols on 24-hr interval

throughout the study period of three months (10th June, 2013 to 16th August, 2013).



Figure 3.8: (a) Laying of cables (b) Cable-jumper- electrodes connection (c) Set-up of system

3.3.3 Data acquisition using Guided Wave Sounding Technique

Data for the guided wave sounding technique was taken with the help of the MALA ProEX Ground Penetrating Radar (GPR) equipment. A shielded monostatic antenna of central frequency of 800 MHz was used in the measurements. Figure 3.10 shows the set-up of the GWS data acquisition on the field.

The measurements were taken with the help of vertical tubes (Fig. 3.6) which were pre-installed in the soil at three locations on each profile (Fig. 3.1b). In all twelve access tubes were installed on the four profiles. These tubes served as a passage for the metal rod of

about 1.0 m in length and with an external diameter of 0.02 m graduated at 0.01 m intervals. The 800 MHz shielded antenna was then positioned closed (about 0.01 m) to the access tube with the metal rod midway between the receiver and the transmitter which was maintained throughout the whole experiment.

As the metal rod was gradually lowered into the access tube at intervals of 0.01 m, guided waves from the transmitter propagating along the metal rod were reflected from the lower end of this rod and then received by the receiver. The lower end of the metal served as a reflector for these waves. Also, the reflection of these waves was due to impedance contrast between the metal rod end and the medium below (Fig. 3.9). The same procedure was used for all the twelve stations in the four profiles and was then repeated for a period of one month (from 22nd July, 2013 to 23rd August, 2013).

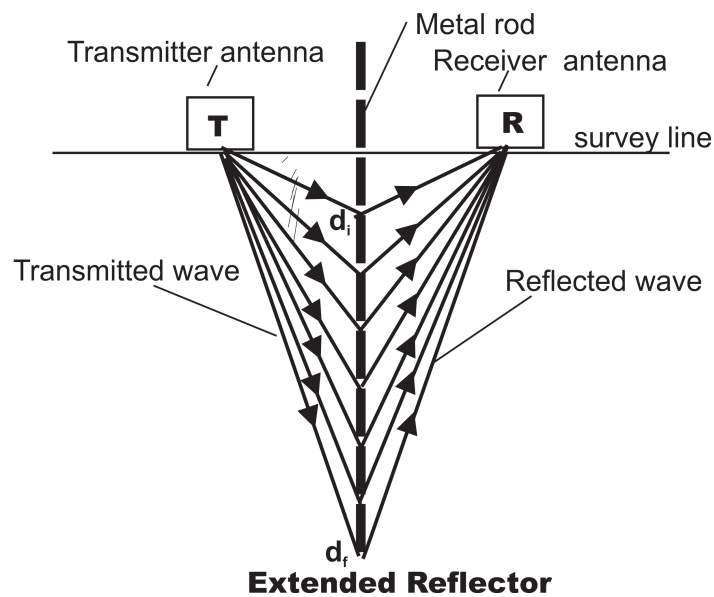


Figure 3.9: Schematic diagram showing reflected waves from the end of the metal rod

When the rod was lowered down from the initial depth d_i to the depth d_f , the interval velocities were calculated from the differences between the guided wave travel times t_i and

t_f , respectively, as;

$$v_{i,f} = \frac{2(d_f - d_i)}{t_f - t_i} = \frac{2d}{t} \quad (3.1)$$

where i and f stands for the initial and final, respectively.

Preko and Wilhelm (2012) observed that, the interval velocities calculated with equation (3.1) were very sensitive to the position and times of the reflection picks. Hence, there was the need to run harmonic mean velocities, H , by the equation (3.2);

$$H = \bar{v} = \left(g_i \sum_{j=1}^n \frac{s_j}{v_j} \right)^{-1} \quad (3.2)$$

and

$$g_i = \left(\sum_{i=1}^n s_i \right)^{-1} \quad (3.3)$$

where s_i is the total distance between arbitrary points, v_i is the interval velocities, n is the number of intervals. The harmonic mean velocity H was related to the permittivity of the soil using equation (2.58), while Topp's equation (Topp et al., 1980) was used to calculate the volumetric water content (VWC). Sample calculation is shown in Appendix A.2.

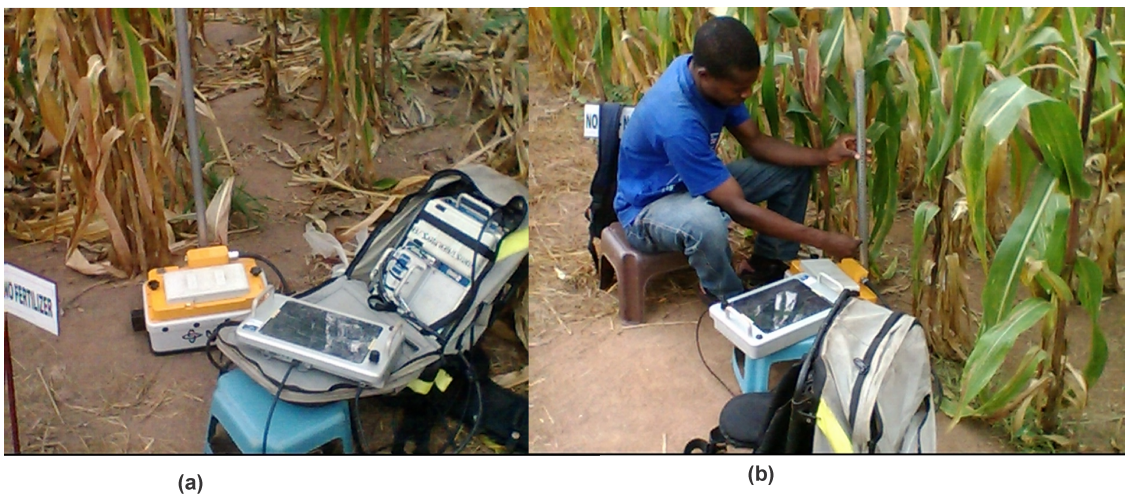


Figure 3.10: (a) Set-up of GWS measurement (b) Operator taking GWS measurement

3.4 Processing of Field Data

The data from the continuous vertical electrical sounding technique and the guided wave sounding method were processed separately. In the case of the resistivity data, the RES2DINV was used whilst REFLEXW was used for that of the guided waves data. Other softwares such as MatLab programming, Grapher, Surfer, CorelDraw and Microsoft paint were also used to enhance the results.

3.4.1 2D Resistivity Data Processing with RES2DINV

After the data collection, transformation of the apparent resistivity pseudo-section into a model of the subsurface resistivity distribution was achieved using the method proposed by Loke and Barker (1996), using the RES2DINV software. Elevation corrections were not carried out because the area was almost flat (Appendix A.3).

The data was first filtered to remove bad data points which were easily viewed as they stand out since the values were displayed in the form of profiles for each data level (Fig. 3.11). These bad data points could be due to the failure of the relays at one of the electrodes, poor electrode-ground contact due to dry, sandy or stony ground, attaching electrodes to wrong connectors, or shorting across the cables due to very wet ground conditions (Loke et al., 2003).

The L_1 -norm (robust) inversion technique was employed to allow the modeling of relatively sharp changes in resistivity because the inversion algorithm aims to minimize the absolute value of data misfit (Loke et al., 2003). In addition, the L_1 -norm also gives more stable results (Zhou and Dahlin, 2003). The Gauss-Newton method was used in calculating the resistivity matrix for all the iterations. To get optimum results, the Inversion/Model refinement was

used which allowed the user to choose models with widths of half electrode spacing. This was necessary because failure to resolve the near surface variations could lead to distortions in the lower portion of the model as the program attempted to reduce the misfit. In addition to the inversion routine, the user defined logarithmic contour interval was applied to all the four profile lines in order to have even contour values and spacing for easier comparison of the profiles lines. The final 2D models were then enhanced using Golden Software Surfer and CorelDraw.

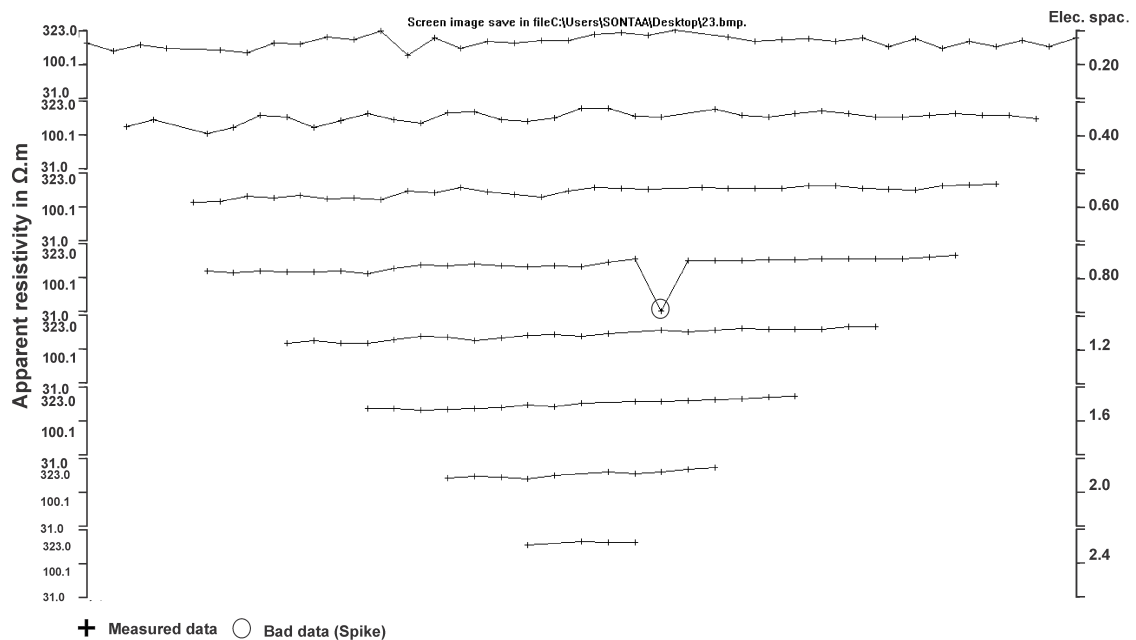


Figure 3.11: Pseudo-section showing bad data points with a spike

3.4.2 2D Time-lapse Data Processing with RES2DINV

In order to investigate the changes in the subsurface resistivity with time during the survey, time-lapse inversion of the apparent resistivity was carried out. The following diagram (Fig. 3.12) shows the processes involved;

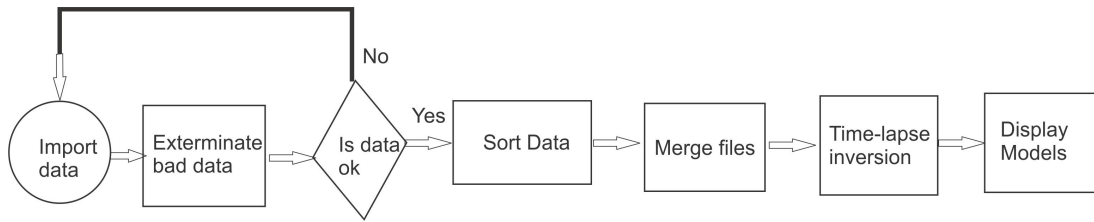


Figure 3.12: Flow diagram for time-lapse data processing

3.4.2.1 Editing of Data

With the help of the RES2DINV, the edited data from Section 3.4.1 was used. There was therefore no need to read in the data to the RES2DINV software. The purpose of using the edited data was to ensure that bad data points (which were easily viewed spikes), as the values were displayed in the form of profiles for each data level were exterminated (Fig. 3.11).

3.4.2.2 Sorting of Data

Data from the resistivity survey are mostly confronted with missing data points from some electrodes. These could be due to malfunction of electrodes in the field whereby the readings were skipped under those electrodes or read negative and were removed when converting to RES2DINV form. Sorting was therefore carried out on each data file from the profiles by running a shell script on Linux terminal to compare two files from the same profile but with different time-lapse (Appendix A.4). The output from the script indicates the position of missing data which was manually corrected. Also, the editing ensured that all the data files from the same profile were of equal length and with same coordinates.

3.4.2.3 Concatenation/Merging of Files

After sorting of the data, another shell script was compiled to merge the individual files into a single file for time-lapse inversion processing. This made it flexible to merge any desired number of files for processing. The merged files were then saved into new names for inversion (Appendix A.4).

3.4.2.4 Inversion of Files

Time-lapse inversion was carried out using RES2DINV software to transform the apparent resistivity pseudo-section into a model of the subsurface resistivity distribution, as described in Section 3.2.1. The data format was similar to that of the normal single data set processed in Section 3.2.1 but with extra header which describes the number of time sections (Appendix A.4). L_1 -norm (robust) inversion techniques, Gauss – Newton method, inversion/model refinement and user defined logarithmic contour interval were all carried out as describe by Loke and Barker (1996). The final models consisted of percentage change in resistivity and percentage desaturation.

For the percentage change in resistivity, the models displayed the change in resistivity obtained from the inversion of a later tie data set compared with the reference model from the inversion of the first data set. In the case of percentage desaturation, the models obtained employed Archie's law given in (Equation 2.31) since it was valid with areas with low clay content. Here, the constant $a = 1$ and $m = 2$ were chosen to determine the change in the fluid saturation or fluid resistivity with time.

3.5 Processing of GWS Data using REFLEXW

Data from the guided wave sounding survey were processed with the Reflexw software (Sandmeier, 2007). A single trace was recorded from the end of the metal rod at a given depth. A complete survey from the base of the metal rod comprised of about 58 to 60 observation points and these were merged into a single radargram.

The first processing step was *Static correction*, which was carried out to correct for static errors whilst *background removal* and *f-k filtering* (Yilmaz and Doherty, 1987) were performed to remove steeply dipping diffraction hyperbola tails (Lunt et al., 2005) arising from the 1.0 cm interval graduation holes bored in the metal rod. In carrying out the *f-k filtering*, an apparent velocity filter range of $0.05 - 0.015 \text{ ms}^{-1}$ was chosen to filter out the spurious signals from the f-k spectrum. This velocity range is reasonable for most electromagnetic wave propagation in geological structures (Preko and Wilhelm, 2012).

In order to eliminate very low and very high frequency noise in the data, *Band pass Butterworth* filter, with a lower cut-off of 266 MHz and an upper cut-off of 1066 MHz was applied. Finally, *gain function* was performed to enhance the amplitudes. All these processing steps were aimed at increasing the signal-to-noise ratio.

After going through the above processing steps, it was then possible to pick *Zero-crossing* distance-time picks from the radargram (Fig. 3.13; Fig. 3.14) and they were loaded in an ASCII-format. The interval velocities (over every 0.005 m) and subsequently harmonic velocities (of every 3 interval velocities) were calculated. Equation (2.58) was used to calculate the corresponding relative dielectric permittivities and the (Topp et al., 1980) calibration equation (Equation 2.55) was eventually used to determine the VWC.

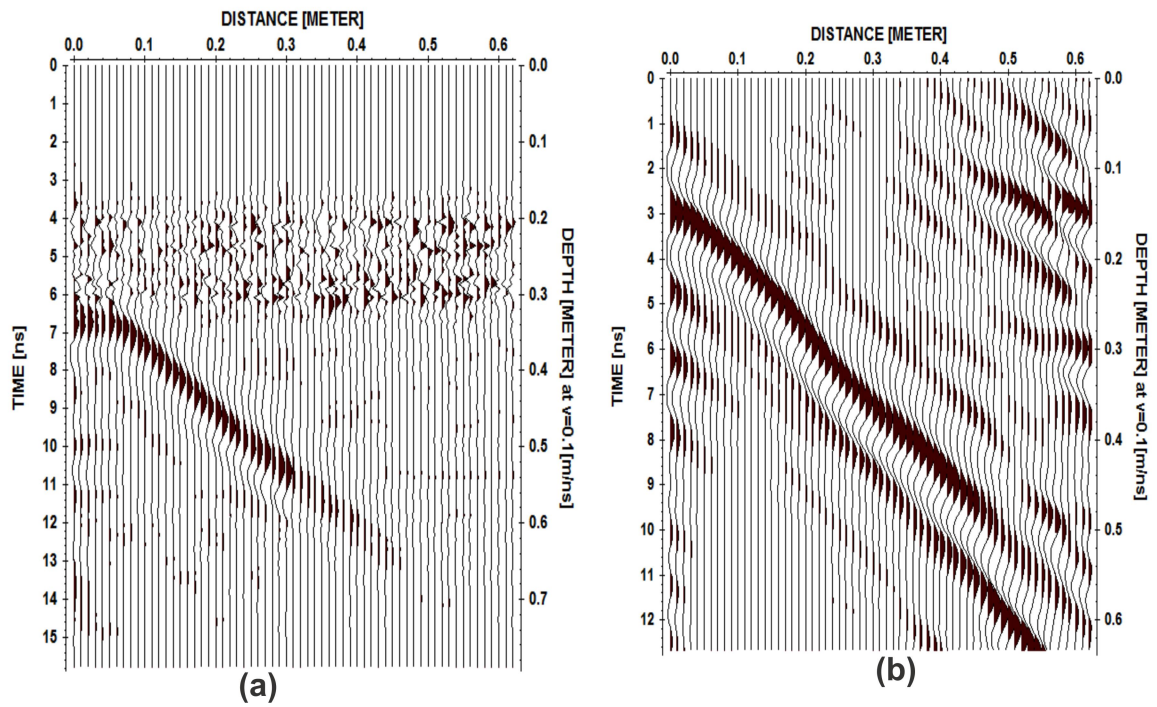


Figure 3.13: (a) Raw data with no processing performed. (b) after background removal, bandpass frequency, dynamic correction, static correction and f-k filter were carried out.

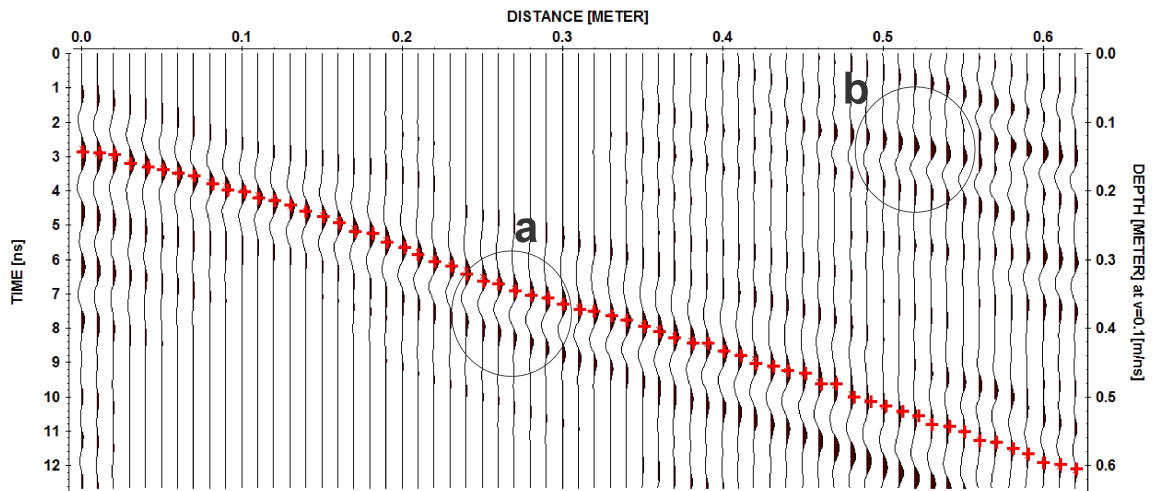


Figure 3.14: (a) Picks from the reflections arising from lower end of metal (b) reflections from graduations in metal rod

CHAPTER 4

RESULTS AND DISCUSSIONS

4.1 Introduction

This chapter contains a description of figures displaying resistivity distribution as a result of variation of the water content in 2D inverse models, percentage change in resistivity models obtained from the inversion of the apparent resistivity data. It takes a critical look at the temporal and spatial variation of the water content in each of the plots, comparative analysis of the four plots and finally quantification of the soil water content in the farm available for plants uptake. In the case of the percentage models, positive variation of the electrical resistivity with time reflects a decrease in water content, and soil water uptake by the plant roots as well as evaporation during that period while a negative variation indicates an increase in soil water content.

4.2 Spatial and Temporal Variation of Soil Moisture Content

In this section, the spatial and temporal variation of the soil moisture content in the four different preparation modes namely ploughed-harrowed, ploughed, hoed and no-till plots are

discussed in details.

4.2.1 Spatial and Temporal Variation of Soil Moisture Content in Ploughed-harrowed Plot

The models in Figure 4.1 display data that were taken from 10th to 24th June, 2013. In this plot, the land has been ploughed and harrowed to break the lumps, loosen the soil and to level up the top soil. Two distinctive zones are indicated in the models i.e, the top layer with a depth of up to 0.34 m and second zone which extends from 0.34 m to the exploration depth of 1.34 m.

On the 10th of June, the topmost part of the soil recorded high resistivity values of about 400 Ω m at different spots across the profile on this plot. A lot of water was extracted at areas where the maize crops were planted. Below this depth lies the second layer which hosted much moisture as indicated by the low nature of its resistivity values. On this layer (Fig. 4.1a), two very low resistivity patches are located at a depth of 0.35 m and 0.50 m, respectively and can be traced to the 1.6 m and 3.20 m mark on the surface of the profile and were interpreted as clay saturated zones.

After 24 hours without rainfall, the resistivity at the top layer especially at the base of the maize crop increases and widens up as much water is lost (Fig. 4.1b). The middle layer which served as the water storage zone also begins to lose water to the surroundings and hence with an increased resistivity values. With little precipitation on the third day at about 00:00 GMT, the topmost layer was recharged reducing the resistivity from about 500 Ω m to about 283 Ω m as, showed in Figure 4.1c. Unfortunately, there was not much variation within the second layer though a little infiltration into the clay saturated zones occurred.

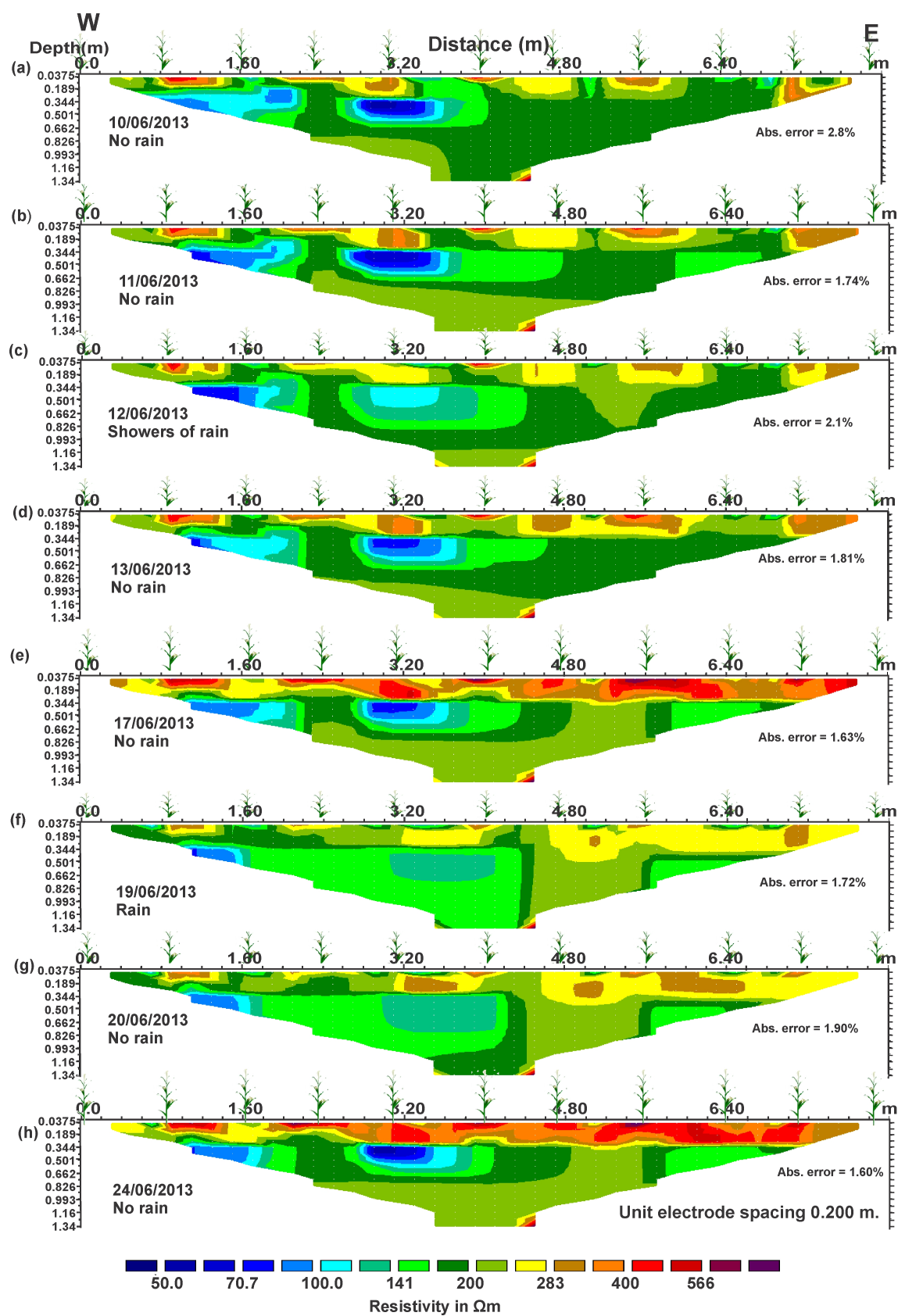


Figure 4.1: Ploughed-harrowed plot resistivity models from 10th – 24th June; (a) 10/06/13 (b) 11/06/13 (c) 12/06/13 (d) 13/06/13 (e) 17/06/13 (f) 19/06/13 (g) 20/06/13 (h) 24/06/13

Two days after this downpour, most of the water at the surface got depleted as well as evaporated rendering it very dry as indicated in the high resistivity values recorded on the 17th of June (Fig. 4.1e). It was also observed that plants have absorbed the moisture within their surroundings which was indicated with very high resistivity values of about 566 Ωm . The dryness in the soil was experienced even at deeper depths which served as the storage zones as there was an increased in resistivity.

However, there was a drastic reduction in resistivity values both spatially and temporally within the plot on the 19th of June model (Fig. 4.1f) as a result of precipitation on the 17th and 19th. The high resistivity values which were distributed within the loosed top soil now recorded values less than 283 Ωm . Some amount of infiltration also occurs within the lower portions, reducing the resistivity values.

Finally, after four days of no recharge, moisture within the top most layer got depleted and consequently very high resistivity values were recorded (Fig. 4.1h).

To assess the temporal changes in resistivity values, time-lapse models were plotted. These are shown in Figure 4.2. The models are compared with the data obtained on the 10th of June. A percentage change scale of -40% to +170% was used in analyzing these models since there was high variation within the surface.

Generally, there was a progressive change of resistivity values within the plot as indicated in all the percentage models. The top layer experienced positive changes during prolong dryness and negative changes when the surface is recharged through precipitation. For that of the lower portion, changes are minimal with instances of no change in resistivity values. Changes were only significant during prolong dryness when most of the moisture was lost through crop extraction, evaporation and percolation into deeper zones.

Initially, after 24 hours of no precipitation, percentage changes within the top layer were more pronounced especially within the location of the maize crops. These changes in

resistivity values ranged from about 40 to 50 while the bottom layer experienced averagely no change in most part, as recorded on 11th June model (Fig. 4.1b).

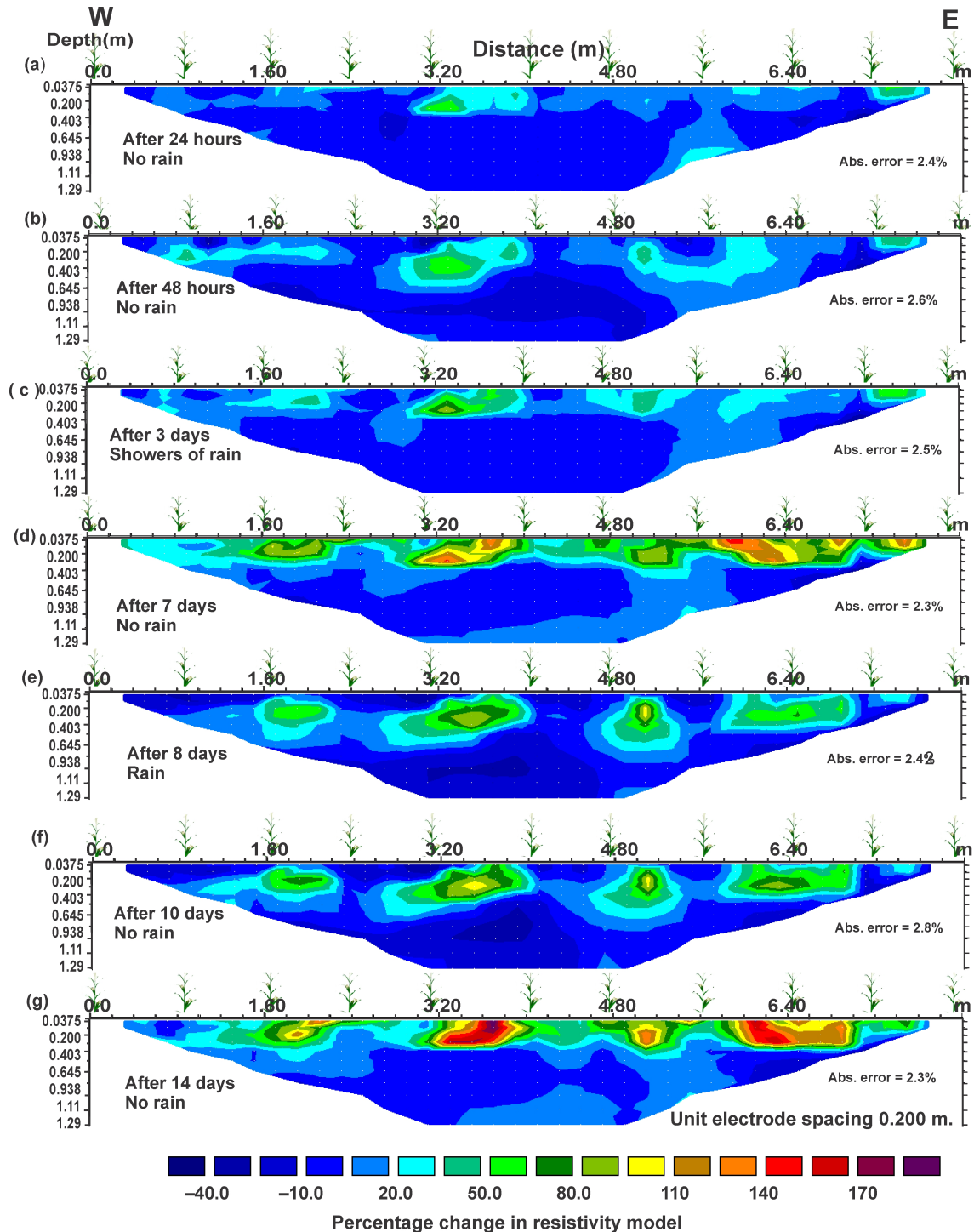


Figure 4.2: Ploughed-harrowed plot percentage change in resistivity models from 11th – 24th June; (a) 11/06/13 (b) 12/06/13 (c) 13/06/13 (d) 17/06/13 (e) 19/06/13 (f) 20/06/13 (g) 24/06/13

After 48 hours and still no precipitation, most of the moisture was lost and the percentage changes attained higher values and even entered the bottom layer. However, a negative change was recorded at the locations of the patches due to infiltration of moisture from the surroundings.

On the 7th day (17/06/13), percentage changes as high as about 20 to 140% (Fig. 4.2d) were recorded, as compared to the model taken on 11th June (Fig. 4.2a). However, these changes were short lived due to antecedent precipitation on the 18th of June, whereby the loose top soil became moistened; as indicated by the negative percentage changes in resistivity. Moreover, there was infiltration of water into the lower portion of the soil and hence negative percentages were recorded.

Finally, just as in the case of the 24th June model (Fig. 4.1h), where high resistivity values were recorded on the near surface as well as the other portions, the percentage change model quantifies these changes in resistivity to be as high as 20 to 170% on the surface and 0 to 15% at the bottom. Most of these high percentage changes and resistivity variations were recorded below the locations where the maize crops were planted, which indicated water consumption by the crops, evaporation, evapotranspiration among, others.

4.2.2 Spatial and Temporal Variation of Soil Moisture Content in Ploughed Plot

Profile 2 was located on the ploughed land where harrowing was not done to break the soil lumps. It also indicates three distinctive zones i.e. the topmost zone measuring to a depth of 0.20 m, a middle low resistive zone which extends from 0.20 m to about 0.60 m and the bottom high resistive zone ranging from a depth of 0.60 m to the exploration depth of 1.3 m

(Fig. 4.3).

Generally, extraction of water by the maize crops was observed in this plot as in the case of the ploughed-harrowed plot with very high resistivity values beneath the maize crops. Spatial moisture variation within the top surface was non-uniform due to the uneven nature of the land as a result of the ploughing. However, recharging of the topmost zone was more pronounced than the ploughed-harrowed plot although infiltration into deeper sections was poor. The middle portion which seems to have a high retention and storage capabilities served as the reservoir for the plants water uptake. These zones had variable depth as it increased when there was precipitation and decreased in depth during prolong dryness. It also hosted a low resistive zone located beneath the 4.80 m mark on the profile which widens during antecedent precipitation and shrinks during prolong dryness.

On the 10th of June (Fig. 4.3a), the resistivity survey revealed low resistivity values of about 200 Ωm and below at the topmost layer, except the depletion zones of the maize crops where water was extracted. The storage zone, thus the middle portion, also recorded resistivity values of 141 Ωm and below. It is also broader with a large portion merging with the topmost layer indicating infiltration paths (Fig. 4.3a). The high resistivity layer recorded resistivity values of about 283 Ωm .

After 24 hours with no precipitation, there is much moisture variation within the topmost layer while that of the high resistivity zone extended upwards to the middle portion (Fig. 4.3b). However, the measurement which was recorded on the third day with antecedent precipitation shows slight reduction in the high resistivity distribution within the topmost and middle layers. The interpreted clay saturated patch was recharged whilst the lower high resistive zone shrunk in size as a result of infiltration of water from the middle portion (Fig. 4.3c).

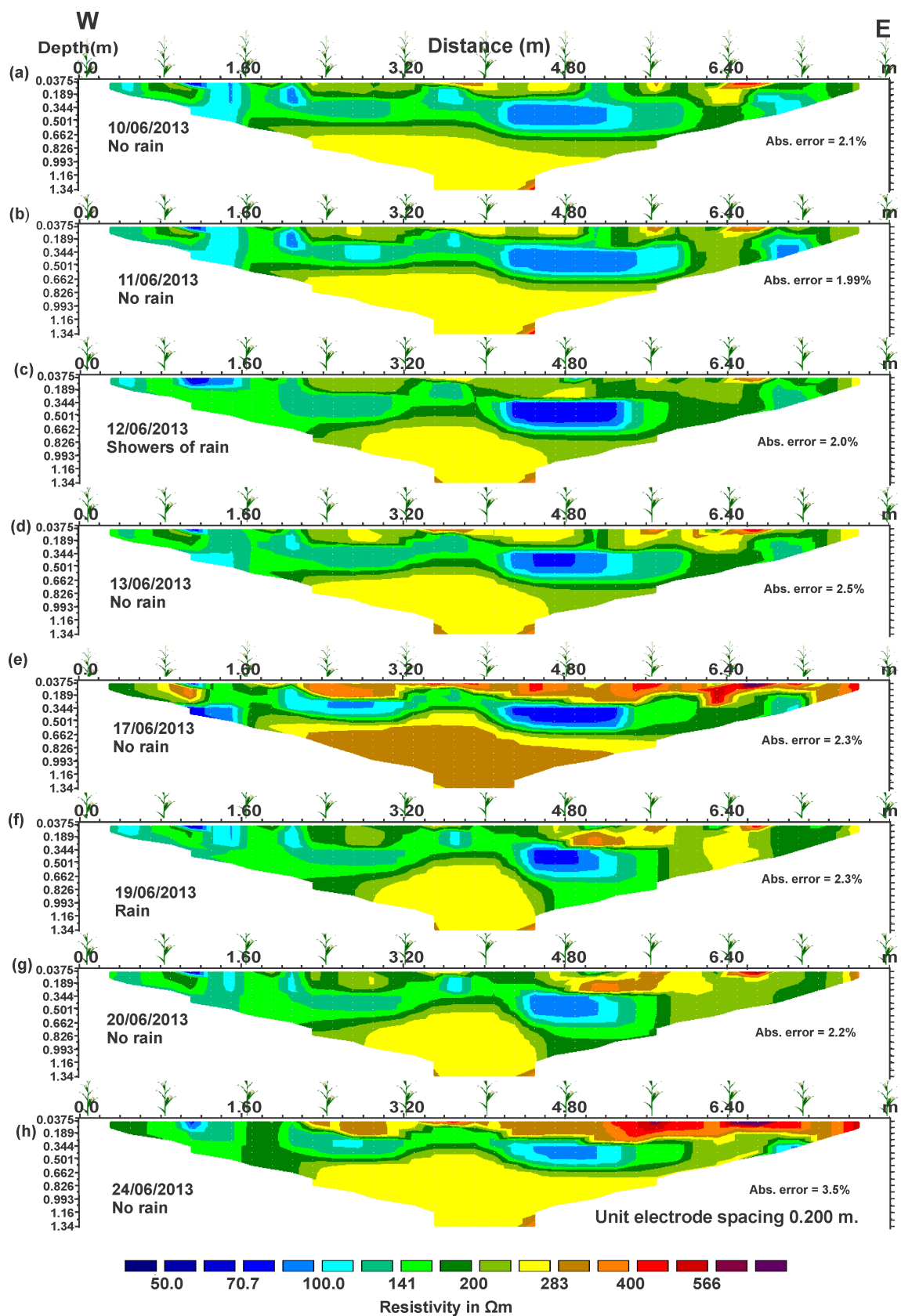


Figure 4.3: Ploughed plot resistivity models from 10th – 24th June; (a) 10/06/13 (b) 11/06/13 (c) 12/06/13 (d) 13/06/13 (e) 17/06/13 (f) 19/06/13 (g) 20/06/13 (h) 24/06/13

Four days without precipitation, higher resistivity values of about 400 Ωm and above were observed on the topmost layer due principally to evaporation and extraction of moisture by the maize crops. In addition, the storage zone shrunk in size as a result of extension of the high resistivity lower portion with resistivity values of about 283 to 300 Ωm (Fig. 4.3e).

A drastic reduction of resistivity variation within the profile was, however, recorded two days (Fig. 4.2e) after the soil was wetted by precipitations on the 17th and 19th of June. Most of the topmost layer returns to normal and merged with the storage zone while that of the high resistive zone shrunk with reduction in resistivity values to about 283 Ωm as a result of infiltration of water.

This pattern was retained for the next two days, though some areas within the topmost layer began to dry up with consequent increased resistivity values. Five days later, the soil experienced dryness due to extraction of water by the maize plants, evaporation, evapotranspiration and percolation.

Finally, it was clearly observed in all the days that the western part of the ploughed land retained a lot of moisture as compared to the eastern side. This could be ascribed to the fact that this zone had high ability to retain precipitation and infiltration water because of its sloping nature. Moreover, due to lack of leveling, the distribution of running water was poorer as runoff water collected at the immediate sections of the plot.

Figure 4.4 shows the percentage changes in resistivity within the models taken over the period with a scale of -20% to +50%. Initially, after 24 hours of no precipitation, the percentage changes within the soil was minimal with the exception of some few spots where about 10% and below was observed, just as in the case of the resistivity model in Figure 4.3b. After showers of rainfall on the third day of measurement, some changes were recorded on the topmost layer as well as the bottom layer (Fig. 4.4c).

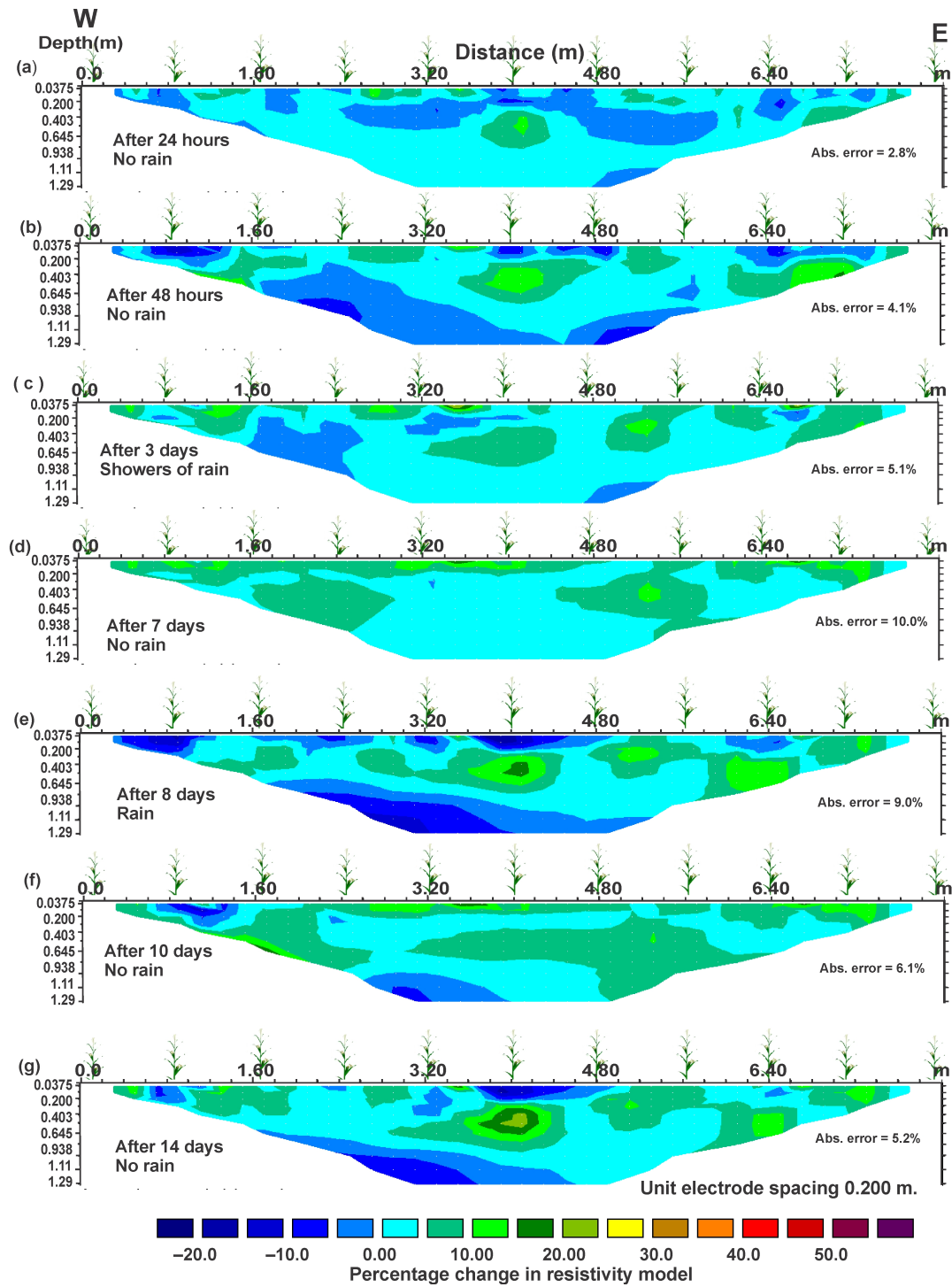


Figure 4.4: Ploughed plot percentage change in resistivity models from 11th – 24th June; (a)11/06/13 (b) 12/06/13 (c) 13/06/13 (d) 17/06/13 (e) 19/06/13 (f) 20/06/13 (g) 24/06/13

After seven days without much significant precipitation, the soil suffered lack of water and positive percentage changes in resistivity of about 5 to 11% were recorded at the

surfaces. The ploughed land, therefore, seemed to retain much water as compared to the ploughed-harrowed since most of the middle portion recorded minimal changes in the absence of precipitation.

4.2.3 Spatial and Temporal Variation of Soil Moisture Content in Hoed Plot

The preparation of this land was done using the traditional method of hoeing, which did not perturb deeper depths, as in the case of ploughing. Unlike the ploughed land, this plot was characterized by two major zones i.e. the topmost layer with a depth up to 0.27 m and the second layer extending from 0.27 m to the exploration depth of 1.34 m (Fig. 4.5). Two patches of very low resistivity values were located beneath 2.40 m and 4.40 m, respectively, at a depth of about 0.34 m. The most resistive zone within the plot was found right on top of the two low resistive clay saturated patches. This could be due to a porous zone within the surface which is susceptible to evaporation of moisture but not enough to penetrate to the deeper section where the water is stored. In addition, infiltration of water from the other sections to the saturated area seemed to increase after antecedent precipitation and reduced in response to prolong dryness.

Generally, a lot of moisture was lost from the top surface through evaporation, extraction by the maize crop as well as infiltration into deeper sections, as compared to the compacted second layer. Here too, loss of moisture beneath the maize crop was characterized by high resistivity values. The soil also exhibited both spatial and temporal changes in moisture variation, as indicated by the heterogeneous distribution in resistivity values shown in Figure 4.5a.

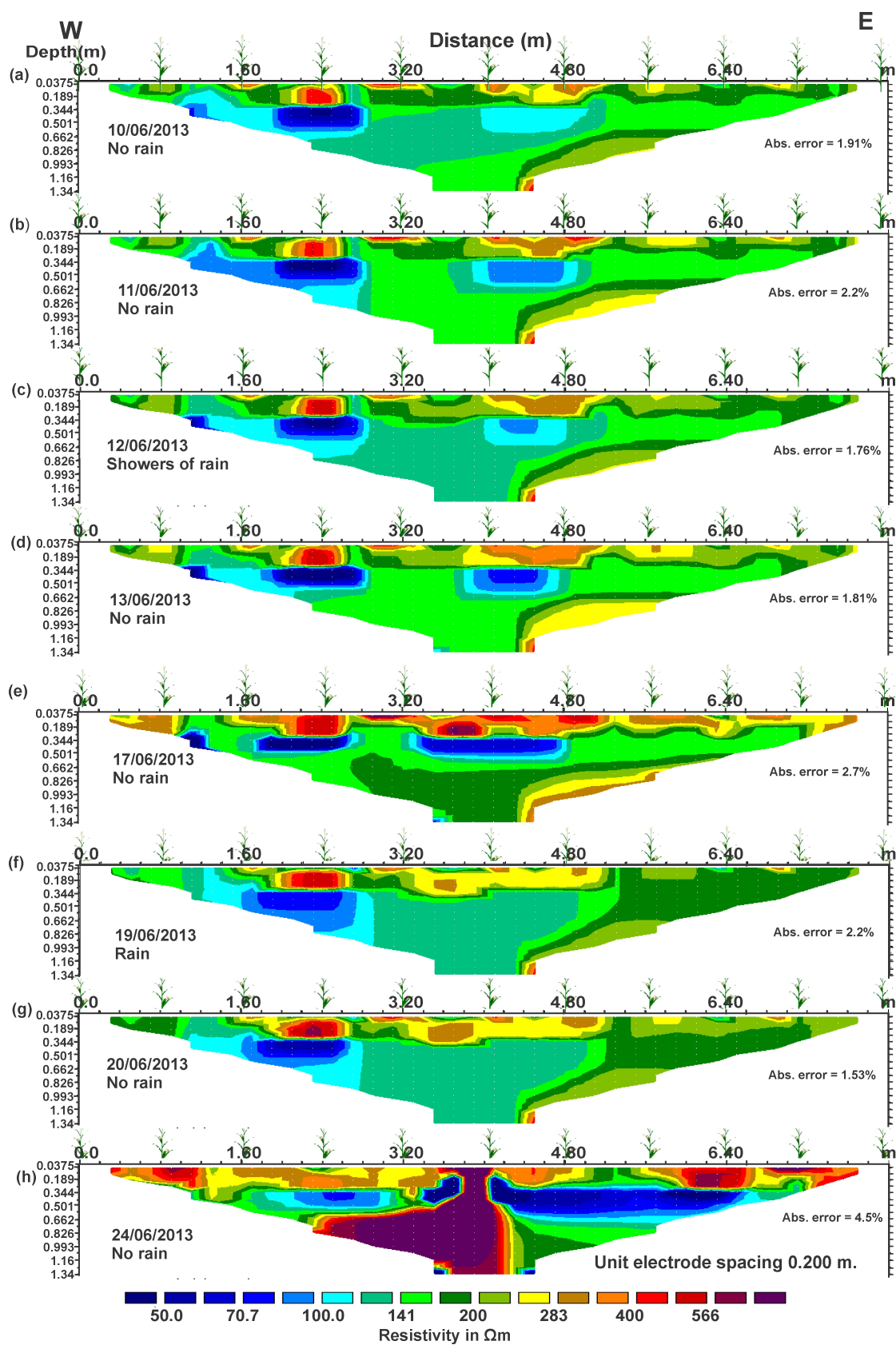


Figure 4.5: Hoed plot resistivity models from 10th – 24th June; (a) 10/06/13 (b) 11/06/13 (c) 12/06/13 (d) 13/06/13 (e) 17/06/13 (f) 19/06/13 (g) 20/06/13 (h) 24/06/13

From the start of the survey on 10th June, the top layer showed higher water content variation especially beneath the maize crop, as shown in Figure 4.5a. Resistivity values of about 200 Ωm to as high as 566 Ωm were recorded on this day. For that of the lower portion, the resistivity was about 141 – 300 Ωm . The whole plot continued to experience an increase in resistivity as result of increasing moisture loss (with the exception of the saturated zones) until the third day (12/06/13) when antecedent precipitation occurred to wet the surface soil. There was infiltration of water into the second layer, indicated by an decrease in resistivity values (Fig. 4.5c).

Two days after this precipitation, high peaks of resistivity values of about 283 to 600 Ωm were recorded in the topmost layer, while resistivity values within the bottom layer increased to 283 Ωm and above. This was, however, short-lived due to precipitations on the 17th and 19th of June (Fig. 4.5f). A large portion of the profile on this plot was recharged by this downpour rendering the electrical resistivity values low.

Finally, after two days elapsed without any precipitation, the soil lost its moisture content both within the surface and the bottom layers. This made measurement very difficult and introduced a lot of errors into the measured apparent resistivity values (Fig. 4.5h).

In the case of the percentage change in resistivity models shown in Fig. 4.6, a low a scale of -30 to +40% was chosen to quantify the changes in the resistivity models with time. Generally, for the first three days, the percentage changes in the models were between 0 and 10% and negative changes of about -10% within the saturated zones due to infiltration of moisture from the immediate vicinities. These changes rose to about 10% after seven (7) days without any significant precipitation in the area. An antecedent precipitation which occurred a day after caused the top layer to have a negative change of about 10% in resistivity.

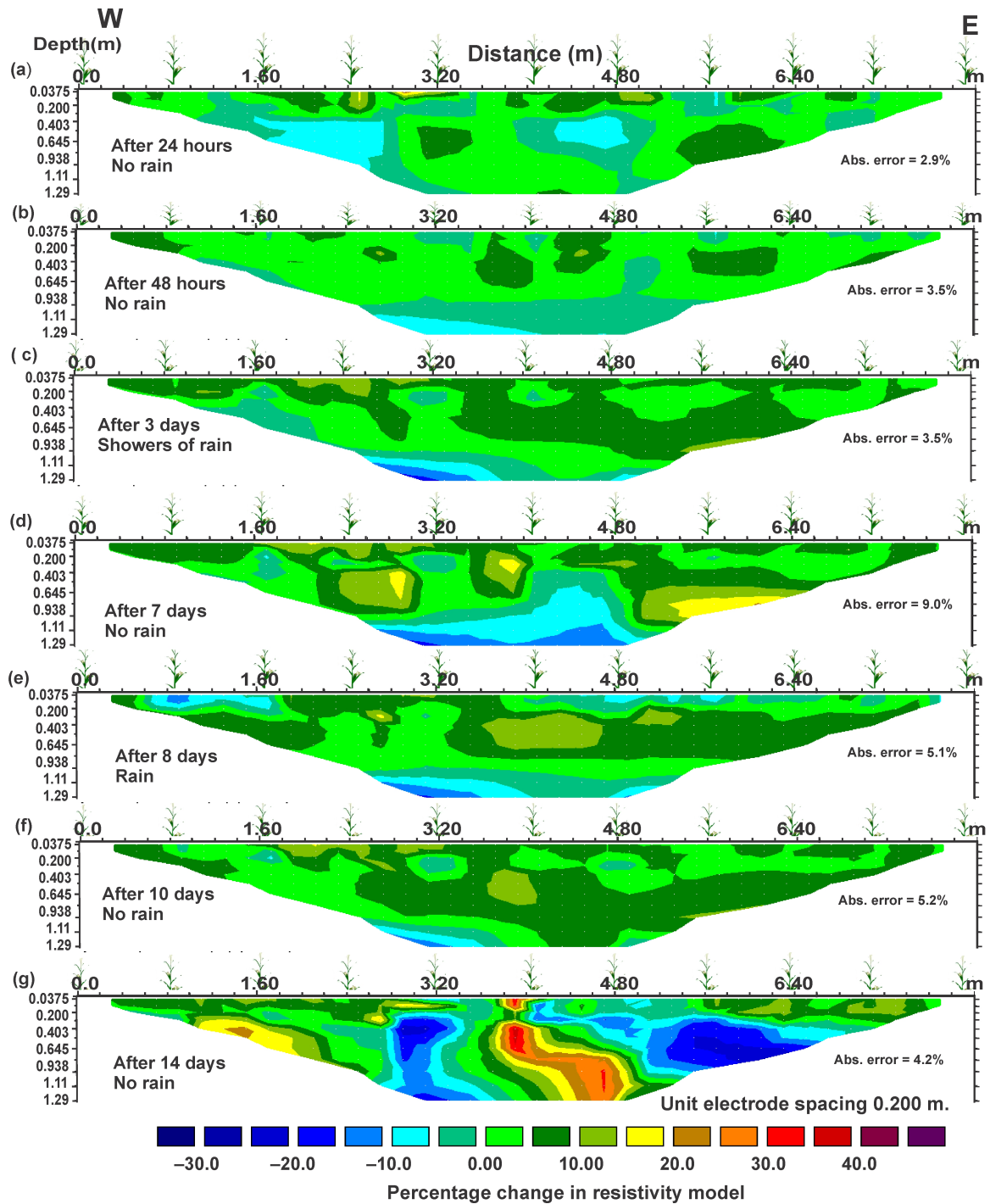


Figure 4.6: Hoeing plot percentage change in resistivity models from 11th – 24th June; (a)11/06/13 (b) 12/06/13 (c) 13/06/13 (d) 17/06/13 (e) 19/06/13 (f) 20/06/13 (g) 24/06/13

It is worth mentioning that, the compacted nature of the soil makes it less susceptible to moisture variations within the second layer, except in the cases of extreme dryness or heavy

downpour in which infiltration occurred as exhibited by the models. In addition, the hoed plot retained a lot of moisture for plants' uptake, due to the broad nature of the low resistive second layer.

4.2.4 Spatial and Temporal Variation of Soil Moisture Content in No-till Plot

Figure 4.7 shows the models that were recorded from the fourth profile located on the no-till plot. In this plot, only weeds were cleared without loosening the surface soil and left to serve as mulch for the soil. In view of this, the top soil layer was clearly well defined with two other layers based on the different resistivity ranges. The topmost layer with moderate resistivity values of about 141 to 283 Ωm lies from the top to about 0.28 m, a middle low resistive zone at a depth of 0.28 – 0.50 m and a very high resistive layer extending from 0.50 m to the exploration depth of 1.34 m. Three low resistive patches were located within the middle portion which influenced the resistivity values in that vicinity. These patches were interpreted as clay saturated zones.

Generally, the no-till plot seemed to have higher water content retention capability by maximizing surface sealing and thereby reducing soil water evaporation. Areas of high resistivity were located beneath the maize crops where extraction occurred, just as in the case of the other plots.

From the start of the study, the results indicated moderate resistivity values of about 250 Ωm and below at the surface; except at two spots located at the 1.60 and 4.0 m mark respectively where resistivity values of 400 and 280 Ωm were recorded. For that of the lower section, the models showed resistivity values of about 280 to 570 Ωm (Fig. 4.7a).

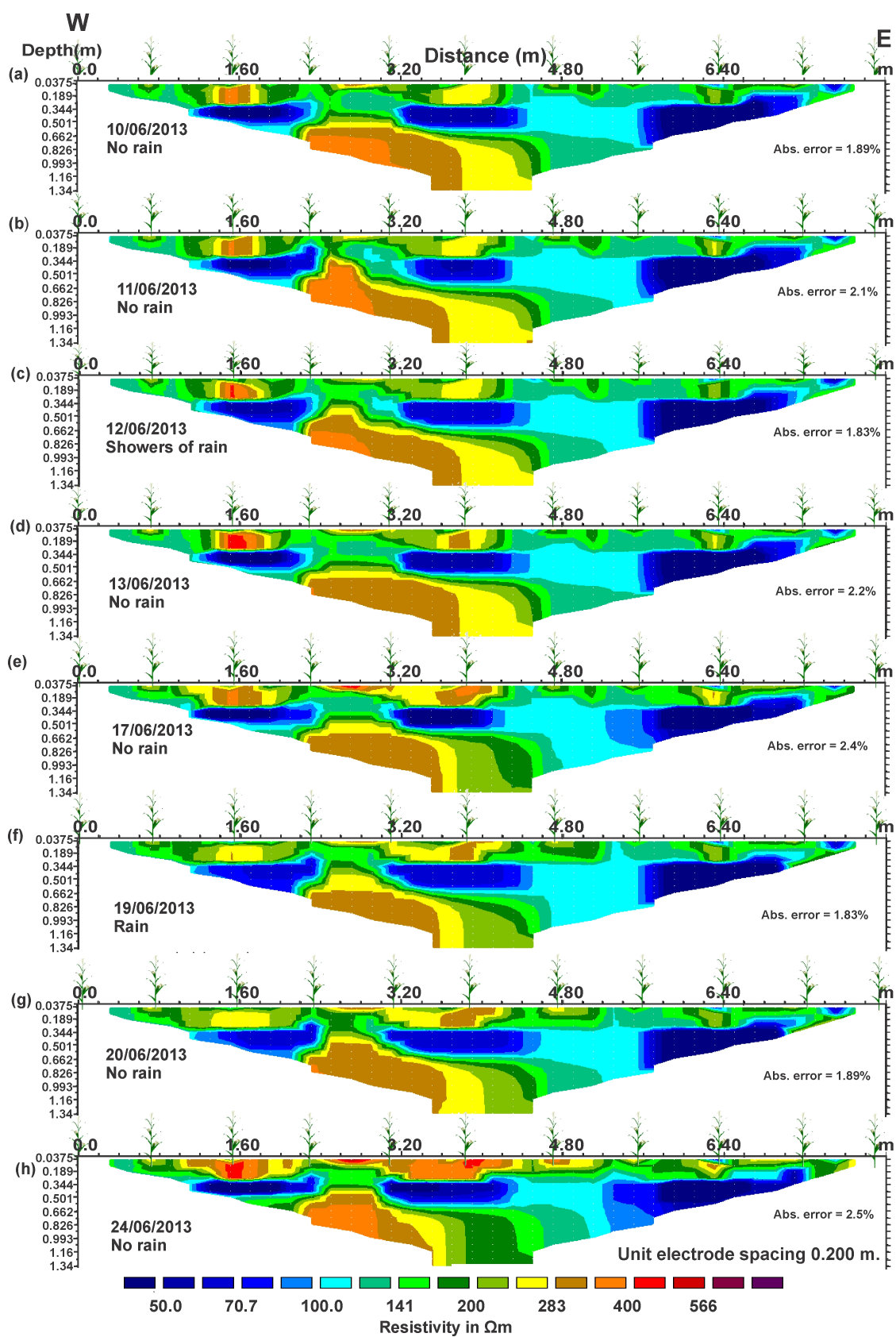


Figure 4.7: No-till plot resistivity models from 10th – 24th June; (a) 10/06/13 (b) 11/06/13 (c) 12/06/13 (d) 13/06/13 (e) 17/06/13 (f) 19/06/13 (g) 20/06/13 (h) 24/06/13

This pattern was repeated even after three days without any antecedent precipitation, indicating high retention of water in the hoed plot.

However, after four days without precipitation, the top soil began to lose some amount of water through evaporation, extraction by the maize plants and infiltration into deeper section (Fig. 4.7e). Two days later, the soil water content at the surface was recharged by precipitation, although there was only little infiltration into deeper sections. This distribution did not last for long as moisture was lost within the surface; with high resistivity distribution occurring while the lower low resistive clay saturated zones shrunk in size (Fig. 4.7h)

For the percentage changes in resistivity with time, Figure 4.8 shows the models obtained. A scale of -30 to +26% was used. This low scale was chosen in order to be able to detect subtle changes in resistivity due to the retentive nature of the plot. Within the first four days, the percentage changes were as low as -14 to +10% with most areas showing no loss of moisture. But after seven days without any significant precipitation (Fig. 4.8d), the temporal moisture variation indicated by the percentage change in resistivity rose to positive changes between 0 – 18% which; was more pronounced within the surface (Fig. 4.8d). Nonetheless, precipitation on the eighth day wetted the soil with some little amount of infiltration, as was indicated in the resistivity model in Figure 4.7f.

After four consecutive days without rainfall, the top soil lost moisture to absorption and evaporation among others, leading to positive percentage changes within the model (Fig. 8g).

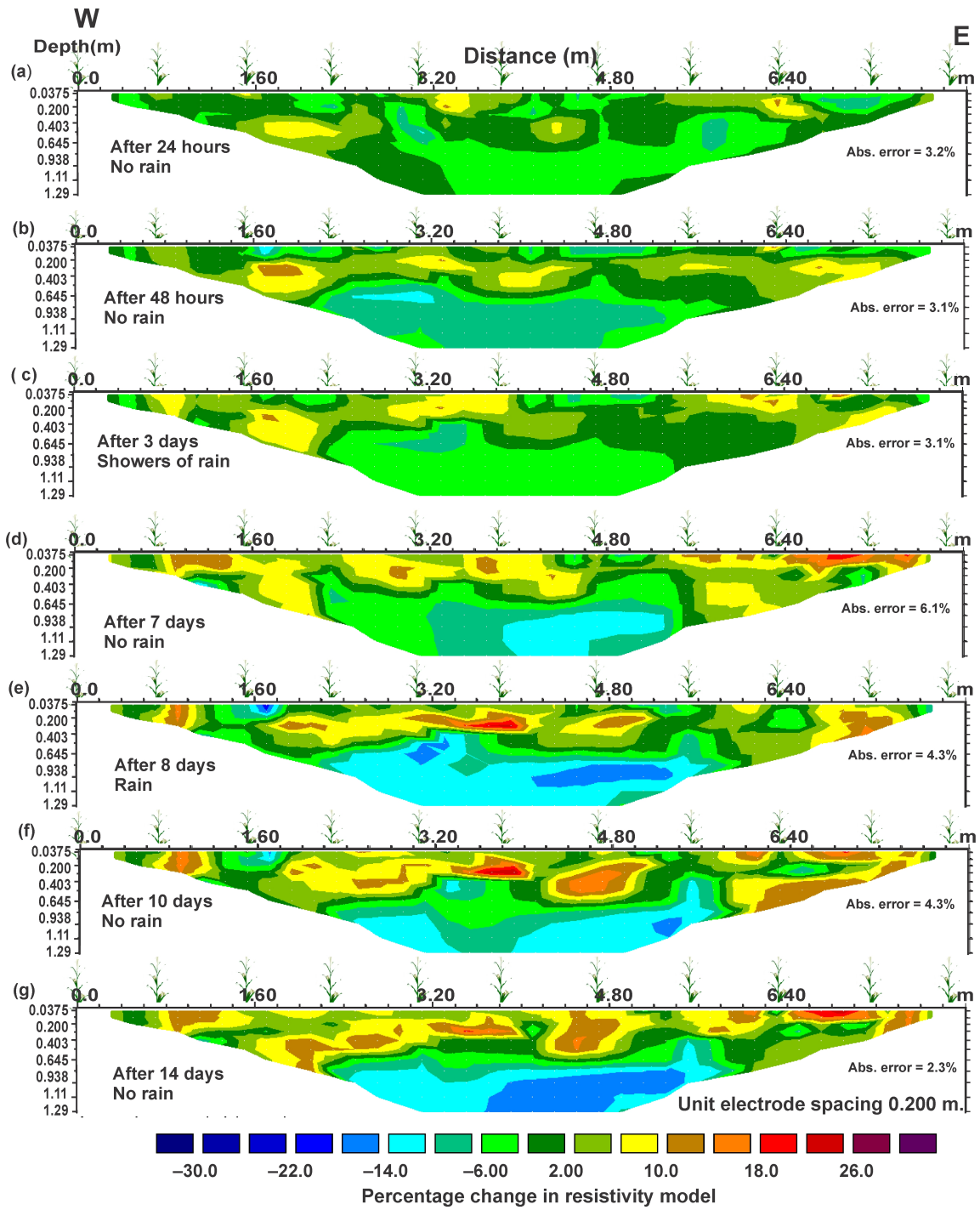


Figure 4.8: No-till plot percentage change in resistivity models from 11th – 24th June; (a) 11/06/13 (b) 12/06/13 (c) 13/06/13 (d) 17/06/13 (e) 19/06/13 (f) 20/06/13 (g) 24/06/13

4.3 Comparative Analysis of Soil Moisture Content Variation Based on Land Preparation Modes

Figures 4.9 and 4.10 show the resistivity models that were obtained from the four profiles in the field. Figure 4.9 was recorded on the 19th of June after an antecedent rainfall in order to investigate the variation of the soil water content distribution in the soil as an effect of rainfall. In the case of Figure 4.10, the data was taken on the 16th of August during dry weather conditions, which also helped to investigate the retention ability of the soil during prolong dryness. The main purpose of this was to do comparative analysis of the soil moisture content variation as a result of the different land preparation modes in response to rainfall and dry weather conditions.

Generally, all the four plots showed soil moisture variation, both spatially and temporally, within the soil. Moreover, it was clear that areas where the maize crop were planted showed presence of soil water extraction by the plant characterized by high resistive values. Clay saturated zones with very low resistivities were present in all the plots which served as the storage zone of moisture.

In the ploughed-harrowed plot (Fig. 4.9a), there was uniform distribution of moisture within the subsurface. This could be ascribed to the leveling and disaggregation that was carried out by the land preparation mode. Also, the top layer easily loses much water (poor retention ability) although there was enough moisture below 0.30 m of the soil. From the resistivity model, this top surface was characterized by resistivity values of about 200 Ωm and above whiles the lower section recorded less than 200 Ωm . As compared to the other plots, this land is considered to have high infiltration rate due to the loosed soil within the top layer. However, the ploughed-harrowed plot is susceptible to high rate of evaporation of

moisture at the surface, as shown in Figure 4.10a, which was recorded after prolong dryness. Comparatively, it recorded the highest resistivity values of about 566 Ωm within the surface during this period.

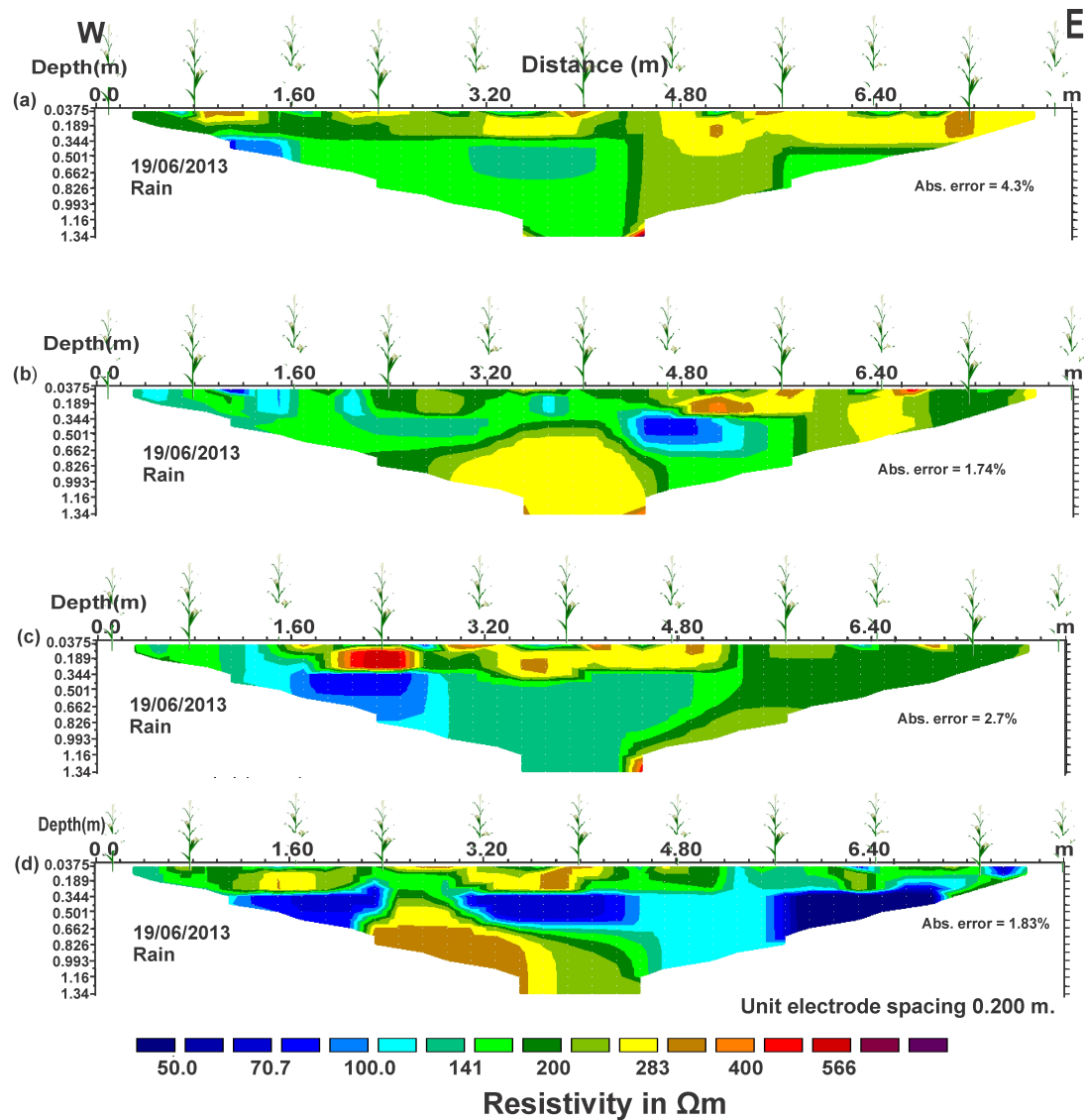


Figure 4.9: Resistivity models obtained on 19/06/13; (a) Ploughed-harrowed plot (b) Plough plot (c) Hoed plot (d) No-till plot

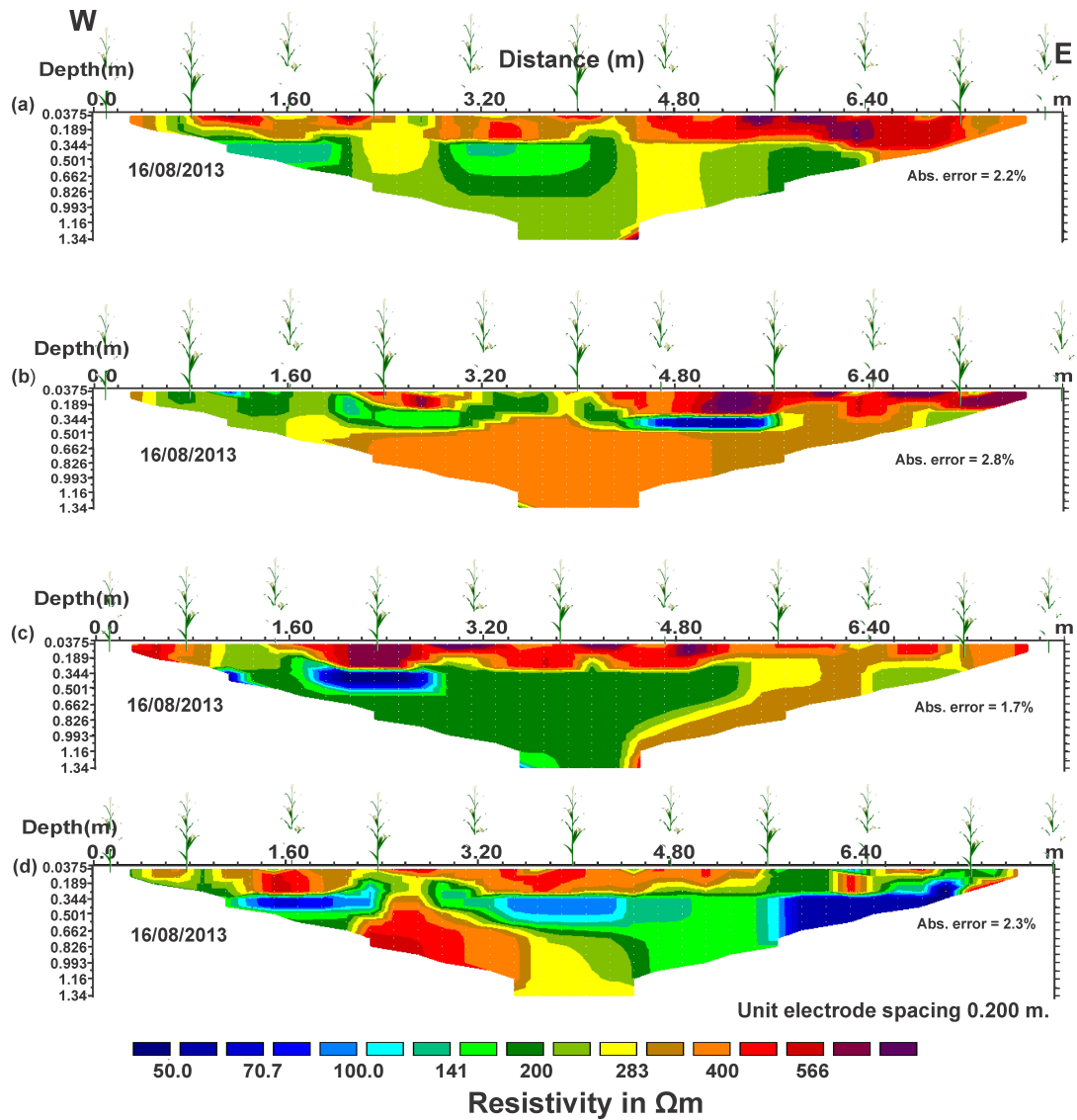


Figure 4.10: Resistivity models obtained on 16/08/13; (a) Ploughed-harrowed plot (b) Plough plot (c) Hoed plot (d) No-till plot

For that of ploughed only plot (Fig. 4.9b), variations of soil water content on the topmost layer was not as uniform as that of the ploughed-harrowed plot. There is retention of water as well as good infiltration within the top surface up to a depth of about 0.40 m. As shown in the model (Fig. 4.9b), the top layer displayed resistivity values of about 100 to 283 Ωm while a very resistive zone of 283 Ωm was located at 0.50 m depth which stretched to 3 m wide on the plot. In the absence of rainfall, the ploughed plot lost moisture at the top surface and

beneath (Fig. 4.10b). As compared to the other plots, the bottom had poor storage capability because of the high resistive zone located beneath with resistivity of about 400 Ωm (Fig. 4.10b) recorded.

In the case of the hoed plot (Fig. 4.9c), moisture was lost at the surface but was less than that of ploughed-harrowed plot. This was attributed to the fact that the traditional hoeing of land does not penetrate deep enough to loosen the deeper sections of the soil. It is therefore more compacted than lands which are either ploughed or harrowed. Moreover, the lower parts (below 0.34m depth) of this profile on the plot serves as a good storage of water for crops uptake. It is characterized by low resistivity values of 200 Ωm and less and covers the entire land (Fig. 4.9c).

During prolong dryness, soil in this plot also loses water within the top layer up to 0.20 m depth but still retains significant amount of moisture below this depth. The top soil exhibited resistivity values of about 400 Ωm and above at most areas whilst lower sections had 200 Ωm and less (Fig. 4.10c).

Profile 4, located on the no-till plot (Fig. 4.9d), showed minimal variation of soil water content within the surface as a result of its compacted nature which led to lesser ability to accept infiltration although it has good retention ability. It also maximized surface sealing and directly reduces soil water evaporation within the surface which increased the retention, as stated earlier. As shown in Figure 4.9d, the top zone has resistivity distribution of about 200 Ωm and below except at the 1.60 m and 3.40 m marks located on top of the saturated clay zones; which recorded resistivity values of about 200 and 300 Ωm , respectively. Also, three saturated zones with very low resistivity which were maintained in the natural formation due to the absence of hoeing or ploughing served as the recharged zone for the immediate surroundings.

For the no-till plot, even during dry weather conditions, the resistivity recorded in the surface

was not as high as the other three plots. There was retention of some amount of moisture within most part of the surface at these periods for plant consumption with the exception of the high zone beneath (Fig. 4.10d).

4.4 Quantification of the Soil Water Content Available for Plant Uptake

In order to quantify the water content in the plots which gave rise to changes in the resistivities, the Guided Wave Sounding technique was employed in the field. Data was recorded at the 0 m, 4.0 m and 8.0 m marks on each profile on the resistivity models (Figs. 4.11 – 4.14). The figures showed VWC graphs and temporal VWC distribution contour maps of a particular hole. For the case of the VWC graphs, daily measurements were plotted on the same graph and indicated with the letter a, b, c, d, e, f, g, h, i and j to represent the days from 22nd June to 23rd August, 2013. Also, the individual legends of the graphs were labelled with 'P_xh_y_mm/dd/yy' where 'P' stands for profile, 'h' stands for hole, the subscript 'x' and 'y' represent the profile and hole number, respectively, and 'mm/dd/yy' stands for the date in which measurements were recorded. The results of a single hole were used in each of the profile for this analysis while the results of the other holes are attached in Appendix A.1.

4.4.1 Volumetric Water Content Distribution in Ploughed-harrowed plot

Figures 4.11a and 4.11b showed graphs of volumetric water content (VWC) and its temporal distribution, respectively, measured at 8 m mark of the ploughed-harrowed plot.

Generally, three zones are indicated on the graphs; the top soil layer (0 – 0.15 m), the middle portion (0.20 – 0.45 m) and the bottom layer (0.45 – 0.60 m), as shown on Figures 4.11a and 4.11b. There was uniform variation of VWC within the top soil layer, as well as an increased in VWC whenever antecedent precipitation occurred which could be due to the loosed nature of the soil on the surface. This trend is clearly shown in the temporal model (Fig. 4.11b), where the VWC rose up on 24/07/13, 26/06/13 and 09/08/13 after antecedent precipitations and with a drop on 24/07/13, 05/08/13 and 23/08/13 around a depth of 0.1 m. For instance, on the 22nd of June (labeled 'a'), the VWC recorded at the surface after an antecedent precipitation was about $0.25 \text{ m}^3\text{m}^{-3}$ while that of the 24th July was lower at the same depth. Two days later, another occurrence of rainfall increased the VWC above that of the 24th graph. This trend was repeated on all the graphs for the three locations on this plot (Appendix A.1). Also, it was observed that the water content within the top layer increased with depth due to infiltration. Averagely, this zone had a volumetric water content of about $0.24 \text{ m}^3\text{m}^{-3}$ during the period of the measurements.

From this zone, most of the water infiltrated into the middle portion located at the depth of 0.20 m to about 0.44 m, with a maximum accumulation occurring at 0.20 m and 0.45 m depth. At this spot, the distribution of VWC in response to precipitation was not as quick as the top layer. This could be due to infiltration of water into deeper depths being depended on the amount of rainfall. Moreover, although the top soil could get wet after precipitation, most of the water either evaporated or was extracted by plants without infiltrating into deeper

depths. For instance, the graph VWC labelled 'a' recorded a value of about $0.30 \text{ m}^3\text{m}^{-3}$, as compared to the graph labeled 'c' with VWC of $0.35 \text{ m}^3\text{m}^{-3}$, at same depth of 0.30 m even though there was antecedent precipitation on both days before the measurements were made. In addition, Figure 4.11 indicated a constant change of VWC with depth (except on the 5th and 9th August) and quantify the average VWC to be about $0.35 \text{ m}^3\text{m}^{-3}$. This zone also stored moisture for the plants water uptake as was the case of the resistivity models. The lower portion experienced a sharp drop of VWC right after the storage zone, which could be due to an impervious layer encountered or poor resolution of the GPR signals (Fig. 4.11b). The average water content at this zone was quantified to be about $0.25 \text{ m}^3\text{m}^{-3}$.

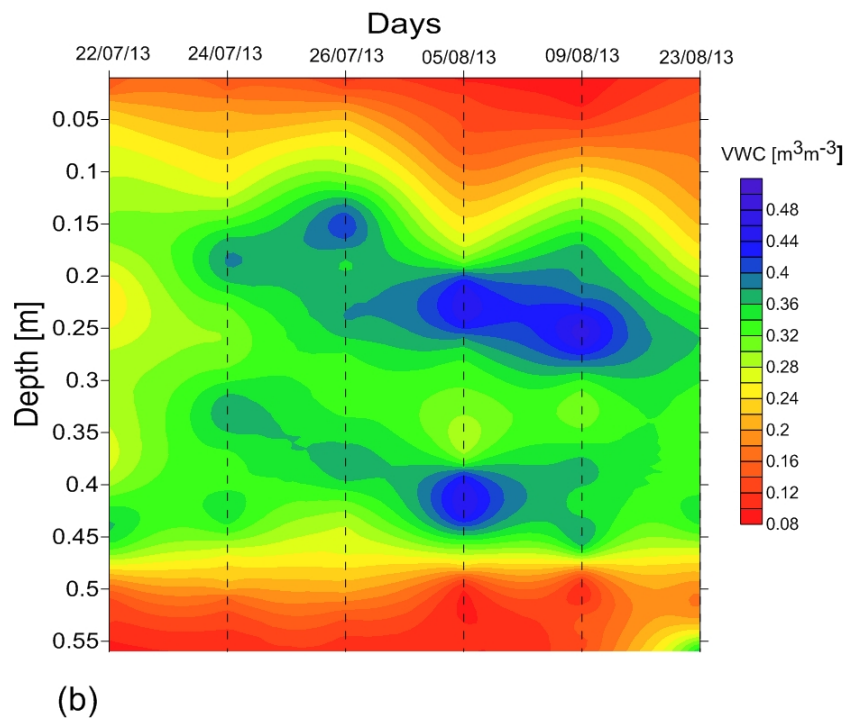
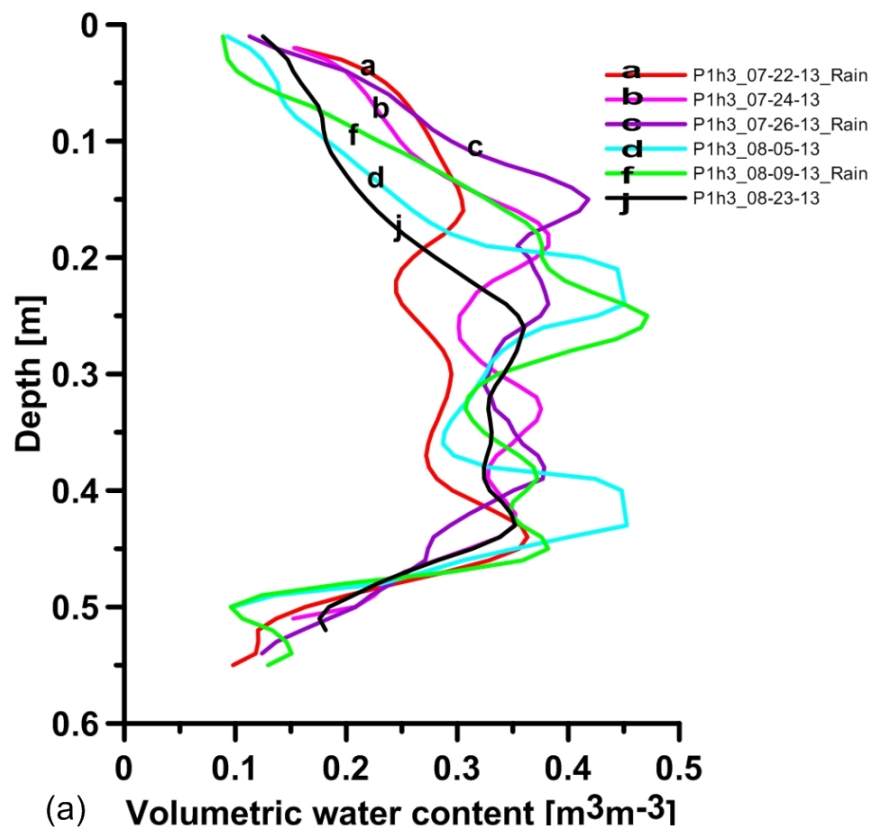


Figure 4.11: Ploughed-harrowed plot VWC distribution (a) VWC graphs from 22/07/13 – 23/08/13 (b) Temporal VWC distribution from 22/07/13 – 23/08/13

4.4.2 Volumetric Water Content Distribution in Ploughed Plot

For that of ploughed profile, Figures 4.12a and 4.12b show the trend of volumetric water content (VWC) with soil depth and its temporal distribution, respectively, measured at 0 m position of the ploughed plot. Unlike the ploughed-harrowed plot in which there was uniform distribution of VWC at the surface, there was non-uniform distribution of soil water content in the ploughed plot. This property was exhibited in the resistivity models in Figure 4.3 and was attributed to the uneven nature of the top surface created by the ploughing.

From 22nd, 24th and 26th of July, the VWC distribution within the top surface was high but dropped to low values on later days (Fig. 4.12b). The graphs labeled (a) – (j) in Figure 4.12b shows a gradual increased of VWC from $0.14 \text{ m}^3\text{m}^{-3}$ to about $0.45 \text{ m}^3\text{m}^{-3}$ within $0 - 0.35 \text{ m}$, with an average amount of $0.35 \text{ m}^3\text{m}^{-3}$.

Much of the water was accumulated at 0.28 m depth of the soil, with a maximum VWC of about $0.45 \text{ m}^3\text{m}^{-3}$ serving as the storage zone for crop water uptake. Below this depth lay a very resistive zone which was delineated by the resistivity measurement (Fig. 4.3). There was a sharp decrease of the VWC at this transition zone due to probably an impervious high resistive zone. At this point, the average VWC was about $0.25 \text{ m}^3\text{m}^{-3}$ and the graph does not follow any trend with respect to antecedent precipitation or drought.

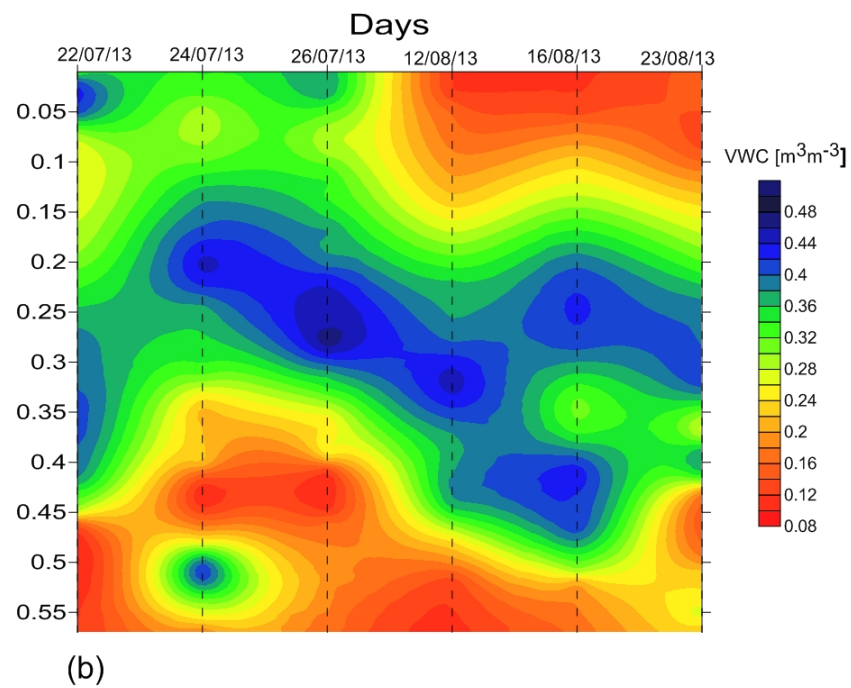
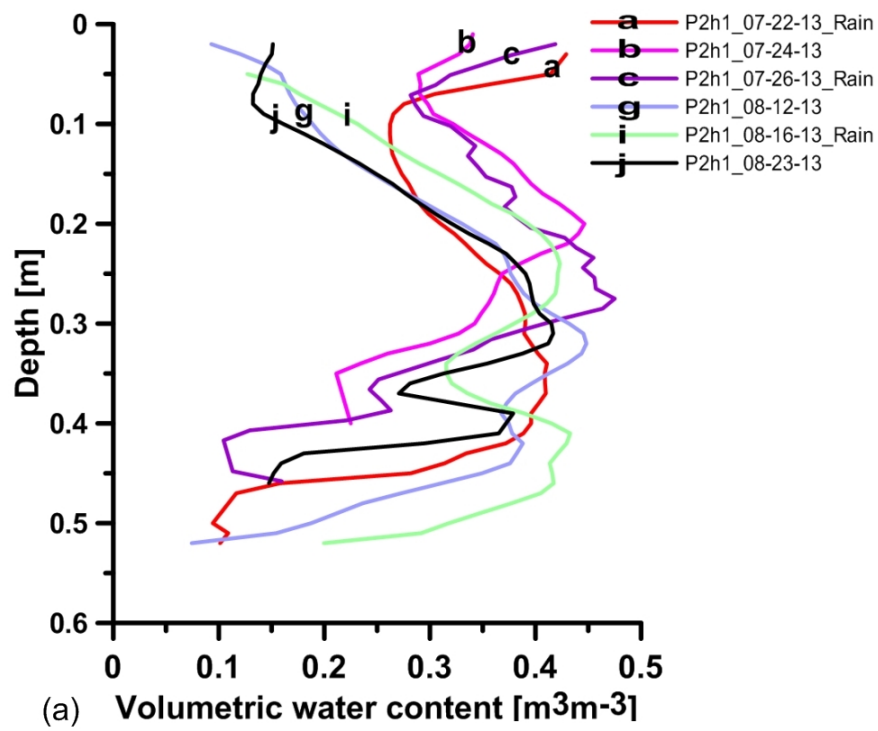


Figure 4.12: Ploughed plot VWC distribution (a) VWC graphs from 22/07/13 – 23/08/13 (b) Temporal VWC distribution from 22/07/13 – 23/08/13

4.4.3 Volumetric Water Content Distribution in Hoed Plot

The volumetric water distribution in the hoed plot from the 22nd July to 23rd August are shown on Figures 4.13a and 4.13b . VWC data was measured at 4.0 m mark. On this plot, three zones of interest are shown by the graph i.e. the top soil layer (0 – 0.15 m), the middle layer (0.15 – 0.45 m) and the bottom layer (0.45 – 0.55 m). Although there was antecedent precipitation on the 22nd of July, it was not heavy enough to increase the VWC graph (Fig. 13a). However, with heavy downpour on the 26th of July, there was a rise in the VWC recorded as compared to the 24th and 22nd at both the surface and at deeper depths (Fig. 4.13b). Averagely, about $0.25 \text{ m}^3\text{m}^{-3}$ of VWC was recorded at the top soil layer.

In addition, there was a general increase of VWC with depth due to infiltration. As the water infiltrated down, the surface got dryer (05/08/13, 16/08/13 and 23/08/13) while a greater portion of the water accumulated at the middle portion (Fig. 4.13b). Here a mean VWC of about $0.35 \text{ m}^3\text{m}^{-3}$ was measured (Fig. 4.13b) and the graphs showed a constant change in VWC with depth (Fig. 4.13a). The hoed plot seemed to also retain a lot of water as compared to the other two plots. Spots of VWC as high as $0.45 \text{ m}^3\text{m}^{-3}$ were observed on all the days that measurements were taken.

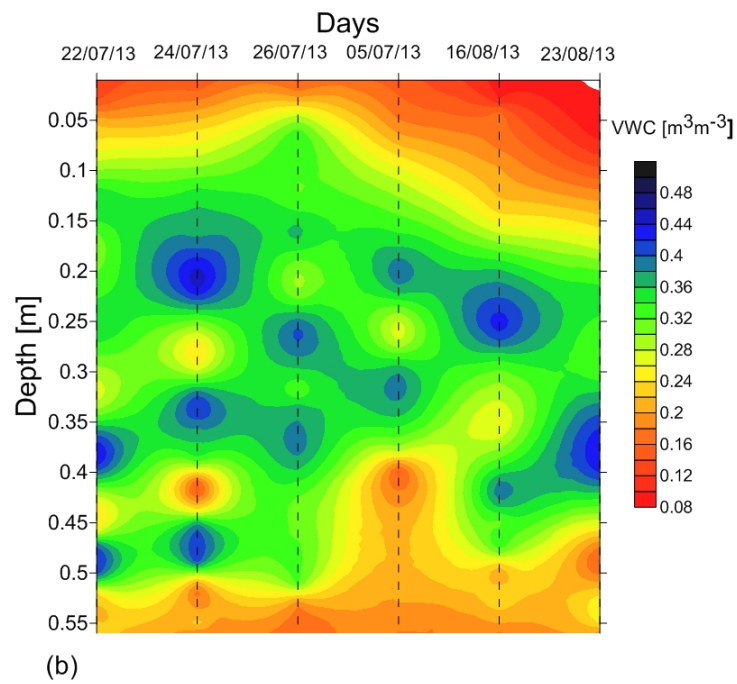
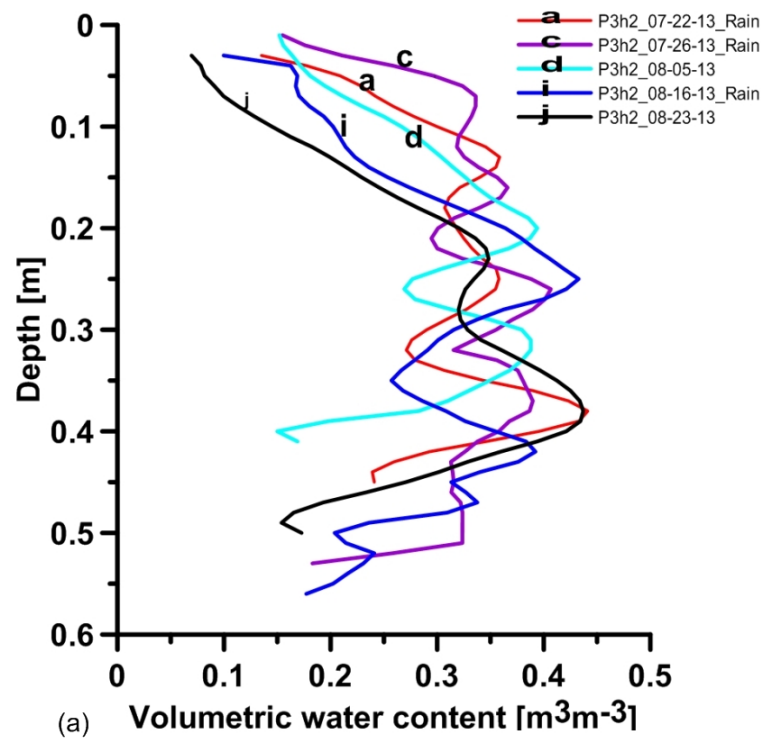


Figure 4.13: Hoed plot VWC distribution (a) VWC graphs from 22/07/13 – 23/08/13 (b) Temporal VWC distribution from 22/07/13 – 23/08/13

4.4.4 Volumetric Water Content Distribution in No-till Plot

The VWC graphs and its temporal distribution were measured at the middle (4.0 m mark) of the no-till plot.

From Figure 4.14, the temporal distribution shows a gradual drop of VWC at the surface with time. At the initial stages (22/07/13), the VWC was high at the top, up to 0.01 m, but continue to show a progressive decrease at later days (26/07/13 – 23/08/13). Within this top soil layer, the variation of VWC showed a uniform trend similar to that of the ploughed-harrowed plot (Fig. 4.14a). With antecedent precipitations on the 22/07/13, 26/07/13 and 16/08/13, the VWC in the hole rose to shallower depths and drops when there was no rainfall (24/07/13, 12/08/13 and 23/08/13) (Fig.4.14b). It was observed that the accumulation of water occurred at a depth of 0.20 m, which is shallow in comparison with the ploughed-harrowed, ploughed and hoed plots. This was due probably to the compacted nature of the top soil since the land was not tilled. Also, the plant residue retained on the surface increased water storage at shallow depths by reducing soil water evaporation. This spot recorded a high VWC of about $0.45 \text{ m}^3\text{m}^{-3}$.

A gradual drop of VWC occurred below the accumulation depths with minimal variations occurring between 0.25 – 0.60 m depths suggesting the retentive capability of this plot. Averagely, the amount of VWC recorded on within this depth range (0.25 – 0.60 m) was $0.35 \text{ m}^3\text{m}^{-3}$ and this appeared to be the storage zone for the plants' uptake (Fig. 4.14b).

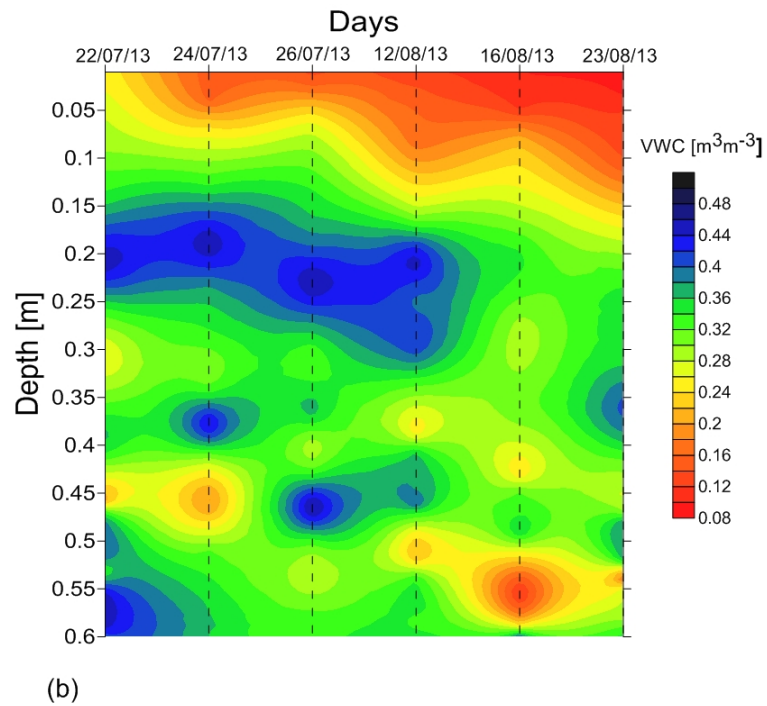
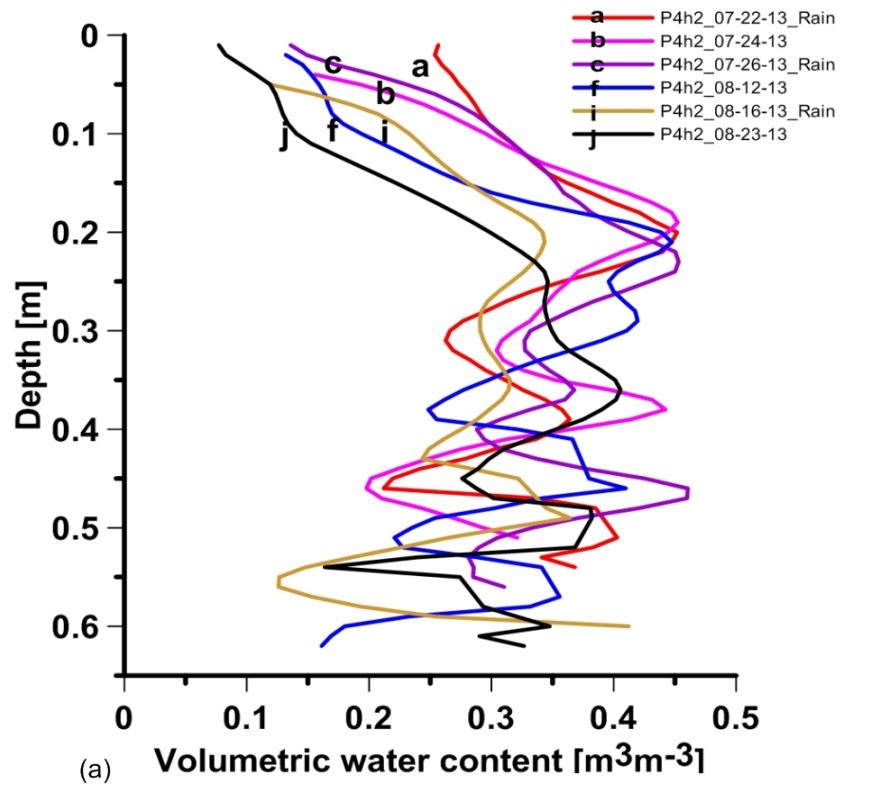


Figure 4.14: No-till plot VWC distribution (a) VWC graphs from 22/07/13 – 23/08/13 (b) Temporal VWC distribution from 22/07/13 – 23/08/13

4.5 Comparison of CVES and GWS Results

To validate the results of the resistivity, the models were compared with that of the VWC distribution maps (Fig. 4.15 – Fig. 4.18). GWS data which were sampled at 0.0 m, 4.0 m and 8.0 m locations on the profiles were used to plot spatial VWC distribution maps.

The general spatial and temporal patterns of water content in the resistivity models and the VWC maps were in good correlation since both methods are very efficient. High VWC distribution resulted in low resistivity values, and vice versa, due to the conduction of water. Although the two results agreed, they were some few exceptions in which the results from the two methods deviated. As was observed by Kachanoski et al. (1988), when clay content was low, the VWC had greater impact on the resistivity of the area, whereas disparities occurred when the clay content was high. The clay in the soil greatly affected the electrical resistivity due to the exchangeable cation and associated water film in the grain matrix. In addition, attenuation of the GPR signal at deeper depths as well as lack of data at the edges of the resistivity models caused these differences.

4.5.1 CVES and GWS Results of Ploughed-harrowed Plot

Figures 4.15a and 4.15b show the ploughed-harrowed plot resistivity models and spatial VWC distribution map obtained on 24/07/13 without antecedent precipitation. The two results showed substantial similarities to each other especially at the top surface. In Figure 4.15a, high resistivity distribution of about 283 – 600 Ωm at the surface was characterized by low water content of $0.16 \text{ m}^3\text{m}^{-3}$. At 4.0 m mark, a high resistivity zone of 400 Ωm (Fig. 4.15a) was caused by low VWC of $0.20 \text{ m}^3\text{m}^{-3}$ (Fig. 4.15b).

Notwithstanding this, some few differences were observed in the two results. For instance,

the resistivity method delineated low resistivity zones at deeper depths, which were quite shallower in the case of the GWS technique. Additionally, at a depth of 0.40 m up to 0.60 m, a low resistivity zone was rather caused by low VWC at same depth (Fig. 4.15b). These differences were partly attributed to the high clay content at deeper depths, as well as attenuation of GPR radar waves.

Even though these disparities existed, the two methods provided useful and consistent information on the spatial and temporal distribution of water content in this plot.

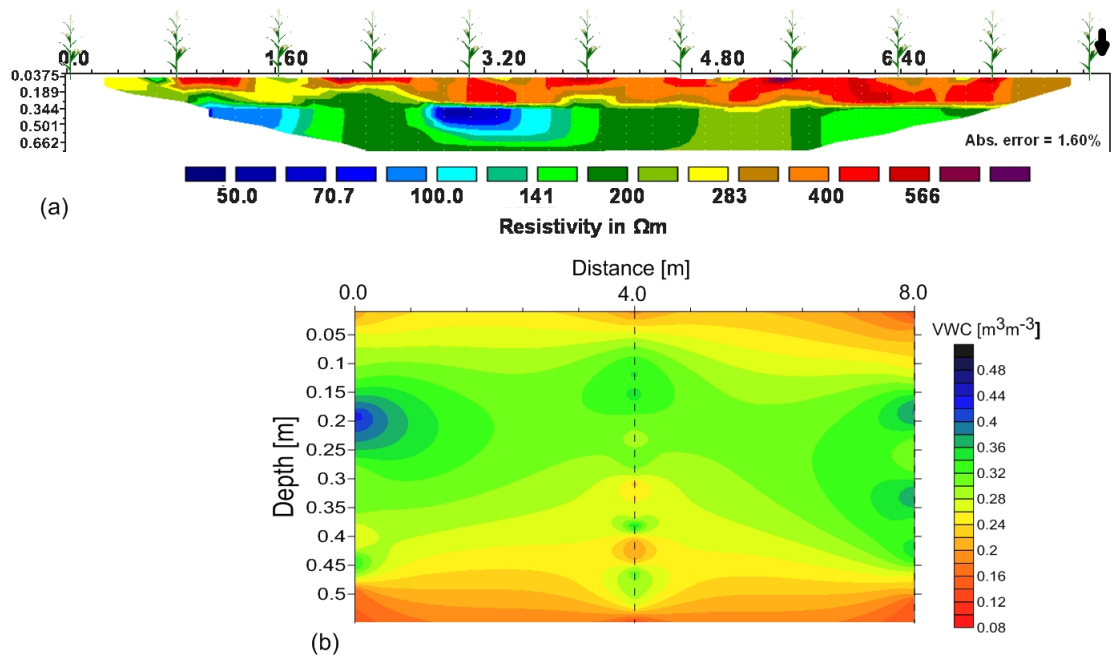


Figure 4.15: Ploughed-harrowed plot CVES and GWS results measured on 24/07/13 (a) Resistivity model (b) Spatial VWC distribution map

4.5.2 CVES and GWS Results of Ploughed Plot

The resistivity models in Figure 4.16a showed a good correlation with the VWC spatial distribution map in Figure 4.16b. The two results were obtained on the 24/07/13, on the 'ploughed only' plot during which the soil was dry. Spatially, both models revealed that

the western side from 0.20 m to about 2.0 m had much water content as compared to the other sections. A low VWC of about $0.08 \text{ m}^3 \text{m}^{-3}$ increased the resistivity distribution at the surface. The middle section at a depth of 0.25 m with high VWC reduced the resistivities to about $200 \Omega\text{m}$ and less. In addition, a very high resistivity of about $283 \Omega\text{m}$ occurred at a depth of 0.4 m and spread across the whole profile was due to a VWC distribution of about $0.08 - 0.20 \text{ m}^3 \text{m}^{-3}$.

As was expected, some disparities were observed. There were depth differences in which particular zones were delineated. Also, a low clay saturated zone occurring at 4.80 m in Fig. 4.16a was absent in the VWC distribution map (Fig. 4.16b).

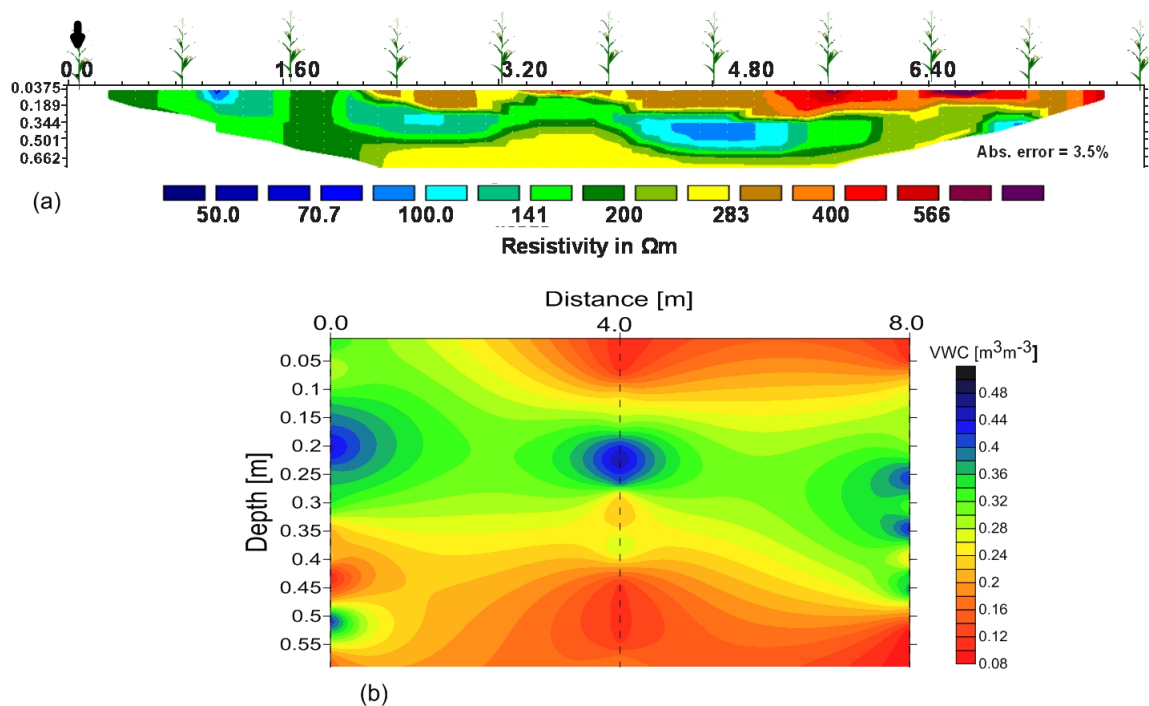


Figure 4.16: Ploughed plot CVES and GWS results measured on 24/07/13 (a) Resistivity model (b) Spatial VWC distribution map

4.5.3 CVES and GWS Results of Hoed Plot

The resistivity and GPR results of the hoed as plot shown on Figure 4.17, displayed some similarities as well some few disparities. The VWC distribution maps showed low water content of about $0.08 - 0.24 \text{ m}^3\text{m}^{-3}$ on the surface, which gave rise to high resistivity distribution (Fig. 4.17a). Also, high water content was generally observed on a large section of Fig. 4.17b. Unfortunately, this did not correlate well with the results of the resistivity (Fig. 4.17a), where only the western section up to 4.80 m was in good agreement. Moreover, the low resistivity patterns observed beneath the maize plants on the surface at 5.40 m, 6.40 m and 7.20 m (Fig. 4.17a) were absent in the VWC model. This was probably due to the extrapolation of data over the larger inter-hole spacing of 4.0 m.

From the two models, though the correlation was poorer, the overall temporal trends in other models showed a significant amount of consistency between the methods.

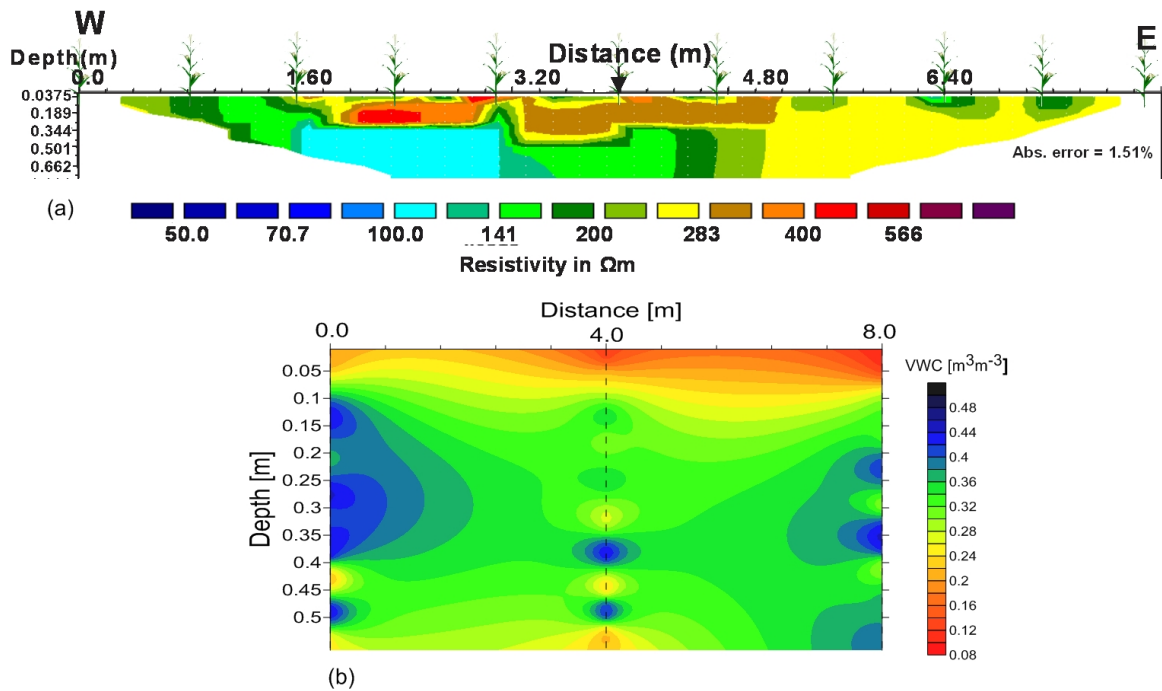


Figure 4.17: Hoed plot CVES and GWS results measured on 24/07/13 (a) Resistivity model (b) spatial VWC distribution map

4.5.4 CVES and GWS Results of No-till Plot

In the case of the no-till plot, Figure 4.18 displayed results of the two methods. Measurements were obtained on the 24/07/13 during which day, the soil was very dry. The spatial water distribution in both results showed the eastern section to contain more moisture than western side. This area was located at the down slope side of the land (Appendix A.3). Additionally, the clay saturated zone in the middle of the plot (Fig. 4.18a) was characterized by VWC of about $0.44 \text{ m}^3\text{m}^{-3}$ (Fig. 4.18b). Unfortunately, there was an appreciable discrepancy between results of the two methods. Two other clay saturated zones located at 1.60 m and 6.40 m on the resistivity model were not delineated by the GWS technique. Moreover, the VWC distributions were as low as $0.08 - 0.16 \text{ m}^3\text{m}^{-3}$ at 0.55 m depth but could not be ascertained on the resistivity model due to lack of data. The high clay content in the soil on the no-till plot greatly influenced the results of both methods.

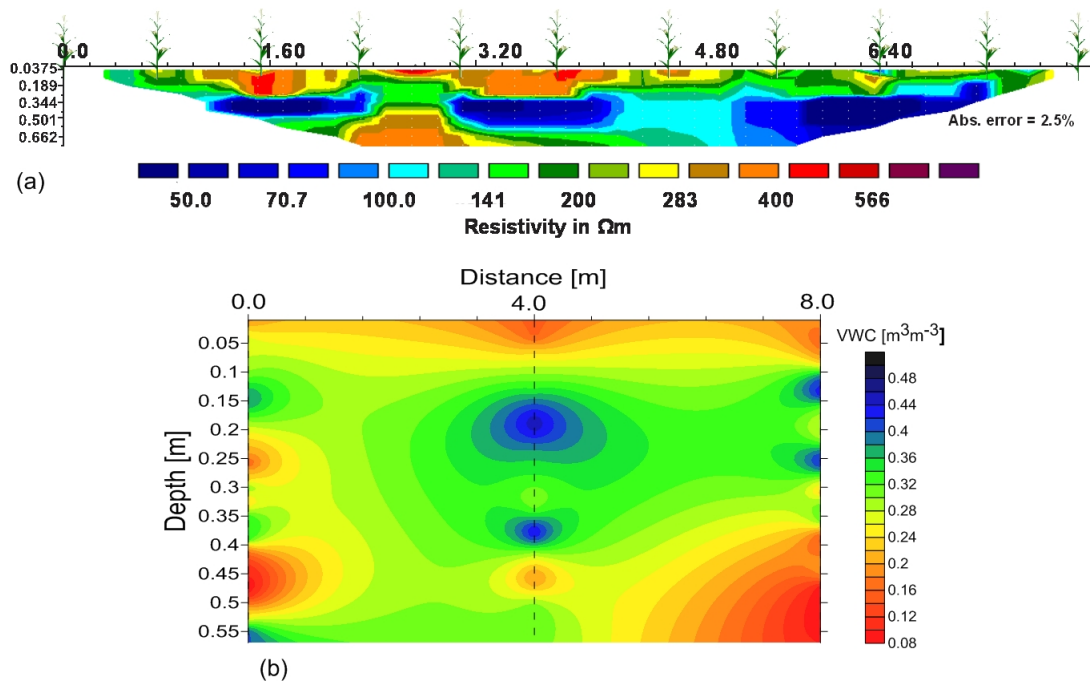


Figure 4.18: No-till plot CVES and GWS results measured on 24/07/13 (a) Resistivity model (b) Spatial VWC distribution map

CHAPTER 5

CONCLUSION AND RECOMMENDATIONS

5.1 Conclusion

The continuous vertical electrical sounding (CVES) technique effectively offered temporal and spatial resistivity variations as result of changes in soil moisture content in the plots. It is efficient and has wider data coverage as compared to the conventional soil sampling methods.

The guided wave sounding (GWS) technique further proved to be very efficient in estimating shallow soil water content which validated the results of the CVES. The two integrated methods (CVES and GWS) were successful in monitoring soil moisture content in the field. Interestingly, the research also explored the applicability of using the improvised electrodes made of wood and copper wire as an alternative to the steel electrodes in monitoring soil water content for agricultural purposes. These electrodes were easy to construct, economical and effectively conduct current within the near surface.

It was assumed that, during the period of the survey there were no changes in lithology and all variations within the soil were as a result soil water content changes. In addition, rainfall played a significant role in the soil water content variations in the plots. The range of resistivity values obtained were between 40 – 600 Ωm which is within that of sandy-loam soil (Loke and Lane Jr, 2004).

Generally, all four plots (ploughed-harrowed, ploughed, hoed and no-till) showed a heterogeneous depletion of soil water content by the maize crop with low/high electrical resistivity (thus soil water content) variations at the surface. Very low resistivity zones apparently due to saturated clay were present in all the plots. The top soil (vadose zone) in all cases experienced much evaporation during prolonged dryness and also hosted majority of the maize roots during the vegetative stage. The roots extracted water either directly from rainfall events or the stored water in the second layer.

The ploughed-harrowed plot showed much soil water content variations within the top soil. Spatially, there is high water content at the Western side of the plot. It had high infiltration rate but very susceptible to evaporation as compared to the ploughed, hoed and no-till plots. This high permeability of the soil was ascribed to the loose soil on its surface which resulted from ploughing and harrowing as well as enhanced activities of earthworms (Beven and Germann, 1982). In addition, the top soil had mean VWC of about $0.25 \text{ m}^3\text{m}^{-3}$ while water available for maize absorption was within the range 0.20 – 0.40 m with maximum occurring at 0.30 m. Temporally, the ploughed-harrowed plot required regular irrigation in order to sustain water for plant use on the top surface. Moreover, it was also suitable for plants with roots above 0.20 m (eg. at the reproductive stage of maize) since most of the low resistive zones lay below this depth and could support vegetable crops during raining season. This type of land preparation is not recommended for early (vegetative) stages of the maize during dry weather conditions due to high evaporation rate.

The spatial distribution of soil moisture in the ploughed plot was non-uniform at the surface with high water content at the Western side. It had minimal evaporation of moisture content as compared to the ploughed-harrowed plot. Water which infiltrated into the deeper sections was conserved, retained and was characterized by low resistivities from the top surface to depths of about 0.54 m. Soil water accumulated at a depth of 0.28 m with mean VWC of

about $0.35 \text{ m}^3\text{m}^{-3}$. The location of this zone made it suitable for shallow rooted plants since they could easily extract water from this depth. The maize crops on this plot could also extract water all times of the growing period. A high resistive zone of about $283 \text{ } \Omega\text{m}$ was found below 0.50 m and extended upwards during dry weather condition. The VWC graphs showed a sharp drop of moisture content at this location. Temporally, the top soil displayed low rate of evaporation, hence scheduling of irrigation in this plot could be done with at regular intervals.

Spatial distribution of soil moisture in the hoed plot was non-uniform with high water content at Western side. It was characterized by two major zones ie the topmost layer with a depth up to about 0.27 m and the second zone extending from 0.27 m to the exploration depth of 1.34 m. The temporal distribution of soil moisture reveals that this plot also had low evaporation rate as compared to the first two plots and could support maize crops during the vegetative stage. Two patches of very low resistive zones were located beneath 2.4 m and 4.40 m, respectively and occurred at a depth of about 0.34 m. Infiltrated water accumulated at the middle portion with mean soil water content of $0.35 \text{ m}^3\text{m}^{-3}$ and served as the recharge zone for the maize crops at all times of the growing season. The hoed plot did not require daily irrigation during the dry season but at regular intervals of about three days to sustain plant water requirements.

In the case of the no-till plot, spatial distribution of soil moisture at the surface was uniform. The soil had higher water content retention capability by maximizing surface sealing and thereby reducing soil water evaporation. In addition, the eastern part of the plot showed low resistivity distribution and in essence had more water content. Maximum accumulation of soil water occurred at a shallow depth of 0.20 m with a mean value of $0.45 \text{ m}^3\text{m}^{-3}$. The soil is suitable for both shallow and deep rooted crops especially during the vegetative stage of maize. The no-till technology therefore conserved moisture by reducing evaporation,

temperature fluctuations and runoff as was observed by Goddard et al. (2008). High infiltration of water could be enhanced if the weeds were retained on the surface. Temporally, the plot did not require regular water supply in the dry weather conditions since conservation was efficient. It is therefore suitable for the maize crops in all in both wet and dry weather conditions.

Finally, CVES and GWS techniques were efficient in monitoring shallow soil water content in the field and results from the measurements could be used to optimize irrigation scheduling and to assess the potential for variable-rate irrigation.

5.2 Recommendations

- To successfully quantify the water uptake by plants, there is need to install a weather station for measuring the right amount of rainfall in the field and also to construct runoff gutters at ends of the plots for calculation of runoff water.
- There is the need to carry out further research with the CVES and GWS methods on different types of soil such as sandy, clayed and loamy with known porosities, cementation, water saturation, and all other factors that affect soil water content.
- There is the need for regular irrigation when practicing the ploughed-harrowed, ploughed only and hoed modes of land preparation in order to sustain crop growth. The no-till method of land preparation conserved a lot of moisture and is therefore suitable for crops during the rainy and dry season.
- There is also the need for long term study (dry and wet seasons) to appreciate long term variations.

- Based on the successfulness of this research, CVES and GWS can be used as geophysical imaging techniques for monitoring soil moisture content in the field in order to enhance better irrigation scheduling.

References

1. Andrews, N. D., Aning, A. A., Danuor, S. K., and Noye, R. M. (2013). Geophysical investigations at the proposed site of the KNUST teaching hospital building using 2D and 3D resistivity imaging techniques. *Int. Res. Jour. Geol. Min*, 3(3):113–123.
2. Aning, A. A., Sackey, N., Jakalia, I. S., Sedoawu, O., Tetteh, E. H., Hinson, G., Akorlie, R. K., Appiah, D., and Quaye, E. K. (2014). Electrical Resistivity as a Geophysical Mapping Tool; A Case Study of the New Art Department, KNUST. *International Journal of Scientific and Research Publications*, 4(1).
3. Aning, A. A., Tucholka, P., and Danuor, S. K. (2013). 2D Electrical Resistivity Tomography ERT Survey using the Multi-Electrode Gradient Array at the Bosumtwi Impact Crater, Ghana. *Journal of Environment and Earth Science*, 3(5):12–27.
4. Archie, G. E. (1942). The electrical resistivity log as an aid in determining some reservoir characteristics. *Trans. AM. Inst. Min. Metal. Pet. Eng.*, 146(1):45–62.
5. Barner, M., Hauser, E., and Wolfe, P. (2001). The use of non-invasive geophysics to assess damage by burrowing animals to earthen levees near Dayton, Ohio. In *Proceedings of the Symposium on the Applications of Geophysics for Engineering and Environmental Problems (SAGEEP)*.
6. Becker, R., Brandelik, A., Hübner, C., Schädel, W., Scheuermann, A., and Schlaeger, S.

- (2002). Soil and snow moisture measurement system with subsurface transmission lines for remote sensing and environmental applications. In *EGS General Assembly Conference Abstracts*, volume 27, page 5812.
7. Benderitter, Y. and Schott, J. J. (1999). Short time variation of the resistivity in an unsaturated soil: the relationship with rainfall. *Eur J Environ Eng Geophys*, 4:37–49.
 8. Bevan, B. W. (2000). An early geophysical survey at Williamsburg, USA. *Archaeological prospection*, 7(1):51–58.
 9. Beven, K. and Germann, P. (1982). Macropores and water flow in soils. *Water resources research*, 18(5):1311–1325.
 10. Binley, A., Cassiani, G., Middleton, R., and Winship, P. (2002). Vadose zone flow model parameterisation using cross-borehole radar and resistivity imaging. *Journal of Hydrology*, 267(3):147–159.
 11. Bottraud, J. C., Bornand, M., and Servat, E. (1984). Mesures de résistivité et étude du comportement agronomique du sol. *Sci Sol*, 4:295–308.
 12. Brunet, P., Clément, R., and Bouvier, C. (2010). Monitoring soil water content and deficit using Electrical Resistivity Tomography (ERT)—A case study in the Cevennes area, France. *Journal of hydrology*, 380(1):146–153.
 13. Celano, G., Palese, A. M., Ciucci, A., Martorella, E., Vignozzi, N., and Xiloyannis, C. (2011). Evaluation of soil water content in tilled and cover-cropped olive orchards by the geoelectrical technique. *Geoderma*, 163(3–4):163–170.
 14. Cousin, I., Besson, A., Bourennane, H., Pasquier, C., Nicoullaud, B., King, D., and

- Richard, G. (2009). From spatial-continuous electrical resistivity measurements to the soil hydraulic functioning at the field scale, *Comptes Rendus. Geoscience*, 341:859–867.
15. Dai, A., Trenberth, K. E., and Karl, T. R. (1999). Effects of clouds, soil moisture, precipitation, and water vapor on diurnal temperature range. *Journal of Climate*, 12(8):2451–2473.
16. Daniels, J. D. (1996). Surface-penetrating radar. *Electronics & Communication Engineering Journal*, 8(4):165–182.
17. Davis, J. L. and Annan, A. P. (1989). Ground-penetrating radar for high-resolution mapping of soils and rock stratigraphy. *Geophysical prospecting*, 37(5):531–551.
18. Friedman, S. P. (2005). Soil properties influencing apparent electrical conductivity: A review. *Computers and electronics in agriculture*, 46(1):45–70.
19. Frohlich, R. K. and Parke, C. D. (1989). The electrical resistivity of the vadose zone—Field Survey. *Ground water*, 27(4):524–530.
20. Gardner, M. K. C., Robinson, D., Blyth, K., and Cooper, J. D. (2008). Soil water content monitoring on a dike model using electrical resistivity tomography. *Near Surface Geophysics*, 6(2):123–132.
21. Ghana, Geological Survey (2009). *Geological map of Kumasi Metropolis*.
22. Goddard, T., Ellis, Y. W., and Watson, S. (2008). World Association Soil and Water Conservation (WASWC). *No-tillage Farming system*.
23. Goyal, V. C., Gupta, P. K., Seth, S. M., and Singh, V. N. (1996). Estimation of temporal changes in soil moisture using resistivity method. *Hydrological processes*, 10(9):1147–1154.

24. Graham, K. M., Preko, K., and Antwi-Boasiako, B. K. (2013). Estimating the Volumetric Soil Water Content of a Vegetable Garden using the Ground Penetrating Radar. *International Journal of Scientific and Research Publications*, 7(3).
25. Griffis, R. J., Barning, K., Agezo, F. L., and Akosah, F. K. (2002). Gold Deposits Of Ghana. *Minerals Commission Report*, pages 7–12, 19–37, 163–169.
26. Gupta, S. C. and Hanks, R. J. (1972). Influence of water content on electrical conductivity of the soil. *Soil Science Society of America Journal*, 36(6):855–857.
27. Habberjam, G. M. (1979). *Apparent resistivity observations and the use of square array techniques*, volume 9. Balogh Scientific Books.
28. Jackson, P. D., Northmore, K. J., Meldrum, P. I., Gunn, D. A., Hallam, J. R., Wambura, J., Wangusi, B., and Ogutu, G. (2002). Non-invasive moisture monitoring within an earth embankment –a precursor to failure. *Ndt & E International*, 35(2):107–115.
29. Kachanoski, R. G., Wesenbeeck, I. J. V., and Gregorich, E. G. (1988). Estimating spatial variations of soil water content using noncontacting electromagnetic inductive methods. *Canadian Journal of Soil Science*, 68(4):715–722.
30. Kalinski, R. J. and Kelly, W. E. (1993). Estimating Water Content of soils from electrical resistivity. *Geotech. Test. J.*, 16:323–329.
31. Kearey, P., Brooks, M., and Hill, I. (2002). *An introduction to geophysical exploration*. Blackwell Science.
32. Kearey, P., Brooks, M., and Hill, I. (2009). *An Introduction to Geophysical Exploration*. John Wiley & Sons.
33. Kesse, G. O. (1972). *The geology of sheet 165, Sekodumasi sw*. Ghana Geol. Survey. Bull.

34. Knight, R. (2001). Ground penetrating radar for environmental applications. *Annual Review of Earth and Planetary Sciences*, 29(1):229–255.
35. Loke, M. H. (1999). Time-lapse resistivity inversion. In *Proceedings of the 5th Meeting of the Environment and Engineering Geophysical Society European Section, Em1*.
36. Loke, M. H. (2001). Tutorial:2D and 3D electrical imaging surveys. Penang, Malaysia, Universiti Sains Malaysia. *Unpublished course notes*, <http://www.geoelectrical.com>.
37. Loke, M. H., Acworth, I., and Dahlin, T. (2003). A comparison of smooth and blocky inversion methods in 2D electrical imaging surveys. *Exploration Geophysics*, 34(3):182–187.
38. Loke, M. H. and Barker, R. D. (1996). Rapid least-squares inversion of apparent resistivity pseudosections by a quasi-Newton method. *Geophysical prospecting*, 44(1):131–152.
39. Loke, M. H. and Lane Jr, W. J. (2004). Inversion of data from electrical resistivity imaging surveys in water-covered areas. *Exploration Geophysics*, 35(4):266–271.
40. Lowrie, W. (2007). *Fundamentals of Geophysics*. Cambridge University Press.
41. Lunt, I. A., Hubbard, S. S., and Rubin, Y. (2005). Soil moisture content estimation using ground-penetrating radar reflection data. *Journal of Hydrology*, 307(1):254–269.
42. Mala (2001). Mala Geoscience, "RAMAC/GPR" Software Manual. <http://www.mala.com>, pages 7–18.
43. Michot, D., Benderitter, Y., Dorigny, A., Nicoullaud, B., Kind, D., and Tabbagh, A. (2003). Spatial and Temporal monitoring of soil water content with an irrigated corn crop cover using electrical resistivity tomography. *Water Resour. Res.*, 39(1):43–53.
44. Milsom, J. (2003). *Field Geophysics*. John Wiley and Sons Ltd.

45. Moon, A. P. (1962). *The geology of sheet 165, Sekodumasi nw.* Ghana Geol. Survey. Bull.
46. Nadler, A., Dasberg, S., and Lapid, I. (1991). Time domain reflectometry measurements of water content and electrical conductivity of layered soil columns. *Soil Science Society of America Journal*, 55(4):938–943.
47. Nijland, W., Van der Meijde, M., Addink, E. A., and De Jong, S. M. (2010). Detection of soil moisture and vegetation water abstraction in a Mediterranean natural area using electrical resistivity tomography. *Catena*, 81(3):209–216.
48. Obeng, H. (2000). Soil Classification in Ghana. CEPA 2000. *Selected Economic Issues*, (3).
49. Olsen, P. A., Binley, A., Henry-Poulter, S., and Tych, W. (1999). Characterizing solute transport in undisturbed soil cores using electrical and X-ray tomographic methods. *Hydrological Processes*, 13(2):211–221.
50. Preko, K. (2007). *Volumetric soil water determination using ground penetrating radar (GPR)*. PhD thesis, Geophysical institute, University of Karlsruhe.
51. Preko, K. and Rings, J. (2007). Volumetric water content measurements of a dike model using electrical and electromagnetic techniques Innovative Moisture Meas. *Res. Pract*, 3:75–82.
52. Preko, K., Scheuermann, A., and Wilhelm, H. (2009). Comparison of invasive and non-invasive electromagnetic methods in soil water content estimation of a dike model. *Journal of Geophysics and Engineering*, 6(2):146.
53. Preko, K. and Wilhelm, H. (2006). Volumetric soil water content monitoring of a dike model using GPR techniques Innovative Moisture Meas. *Res. Pract*, 2:65–71.

54. Preko, K. and Wilhelm, H. (2012). Detection of water content inhomogeneities in a dike model using invasive GPR guided wave sounding and TRIME-TDR® technique. *Journal of Geophysics and Engineering*, 9(3):312.
55. Reynolds, J. M. (1997). *An introduction to Applied and Environmental Geophysics*. Wiley.
56. Rhoades, J. D., Kaddah, M. T., Halvorson, A. D., and Prather, R. J. (1977). Establishing soil electrical conductivity-salinity calibrations using four-electrode cells containing undisturbed soil cores. *Soil Science*, 123(3):137–141.
57. Rings, J., Scheuermann, A., Preko, K., and Hauck, C. (2008). Soil water content monitoring on a dike model using electrical resistivity tomography. *Near Surface Geophysics*, 6(2):123–132.
58. Samouëlian, A., Cousin, I., Richard, G., Tabbagh, A., and Bruand, A. (2003). Electrical resistivity imaging for detecting soil cracking at the centimetric scale. *Soil Science Society of America Journal*, 67(5):1319–1326.
59. Samouëlian, A., Cousin, I., Tabbagh, A., Bruand, A., and Richard, G. (2005). Electrical resistivity survey in soil science: a review. *Soil and Tillage Research*, 83(2):173–193.
60. Sandmeier, K. J. (2007). Reflexw manual, version 4.5. www.sandmeier-geo.de.
61. Scheuermann, A., Schlaeger, S., Hübner, C., Brandelik, A., and Brauns, J. (2001). Monitoring of the spatial soil water distribution on a full-scale dike model. In *Proceedings of the Fourth International Conference on Electromagnetic Wave Interaction with Water and Moist Substances, Weimar, MFPA*, pages 343–350.
62. Schmalholz, J., Stoffregen, H., Kemna, A., and Yaramanci, U. (2004). Imaging of water

- content distributions inside a lysimeter using GPR tomography. *Vadose Zone Journal*, 3(4):1106–1115.
63. Schmugge, T. J. (1985). *Remote Sensing of Soil Moisture "Hydrological Forecasting" edited by M. G. Anderson and T. B. Burt*. John Wiley, New York.
 64. Scollar, I., Tabbagh, A., Hesse, A., and Herzog, I. (1990). *Archaeological prospecting and remote sensing*. Cambridge University Press.
 65. Slater, L., Binley, A. M., Daily, W., and Johnson, R. (2000). Cross-hole electrical imaging of a controlled saline tracer injection. *Journal of Applied Geophysics*, 44(2):85–102.
 66. Srayeddin, I. and Doussan, C. (2009). Estimation of the spatial variability of root water uptake of maize and sorghum at the field scale by electrical resistivity tomography. *Plant and soil*, 319(1-2):185–207.
 67. Tabbagh, A. (1985). The response of a three-dimensional magnetic and conductive body in shallow depth electromagnetic prospecting. *Geophysical Journal of the Royal Astronomical Society*, 81(1):215–230.
 68. Telford, W. M., Geldart, L. P., and Sheriff, R. E. (1990). *Applied Geophysics*. Cambridge University Press, second edition.
 69. Teuling, A. J. and Troch, P. A. (2005). Improved understanding of soil moisture variability dynamics. *Geophysical Research Letters*, 32(5).
 70. Topp, G. C., Davis, J. L., and Annan, A. P. (1980). Electromagnetic determination of soil water content: Measurements in coaxial transmission lines. *Water Resources Research*, 16(3):574–582.

71. Topp, G. C., Davis, J. L., and Annan, A. P. (1982). Electromagnetic determination of soil water content using TDR: I. Applications to wetting fronts and steep gradients. *Soil Science Society of America Journal*, 46(4):672–678.
72. Whalley, W. R. and Bull, C. R. (1991). An assessment of microwave reflectance as a technique forestimating the volumetric water content of soil. *Journal of agricultural engineering research*, 50:315–326.
73. Yilmaz, Ö. and Doherty, S. M. (1987). *Seismic data processing*, volume 2. Society of Exploration Geophysicists Tulsa.
74. Zegelin, S. J., White, I., and Russell, G. F. (1992). A critique of the time domain reflectometry technique for determining field soil-water content. *Advances in measurement of soil physical properties: bringing theory into practice*, (advancesinmeasu):187–208.
75. Zhou, B. and Dahlin, T. (2003). Properties and effects of measurement errors on 2D resistivity imaging surveying. *Near Surface Geophysics*, 1(3):105–117.

Appendix A

A.1 Volumetric Water Content (VWC) Graphs

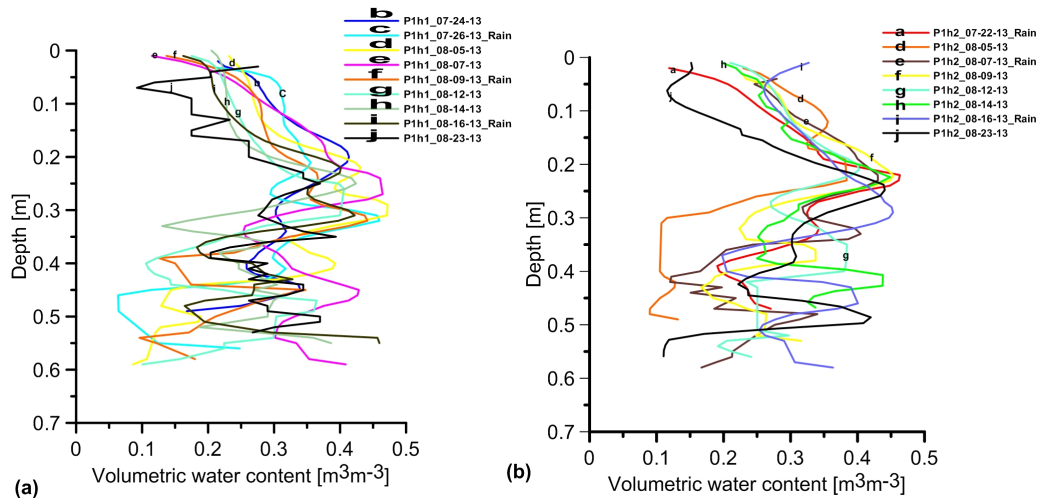


Figure A.1: Ploughed-harrowed plot VWC graphs (a) hole 1 (b) hole 2

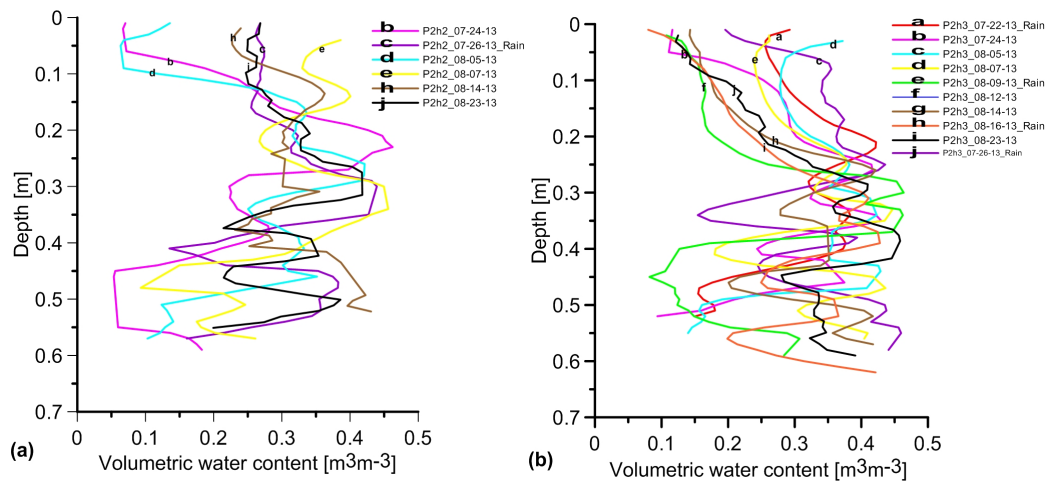


Figure A.2: Ploughed plot VWC graphs (a) hole 2 (b) hole 3

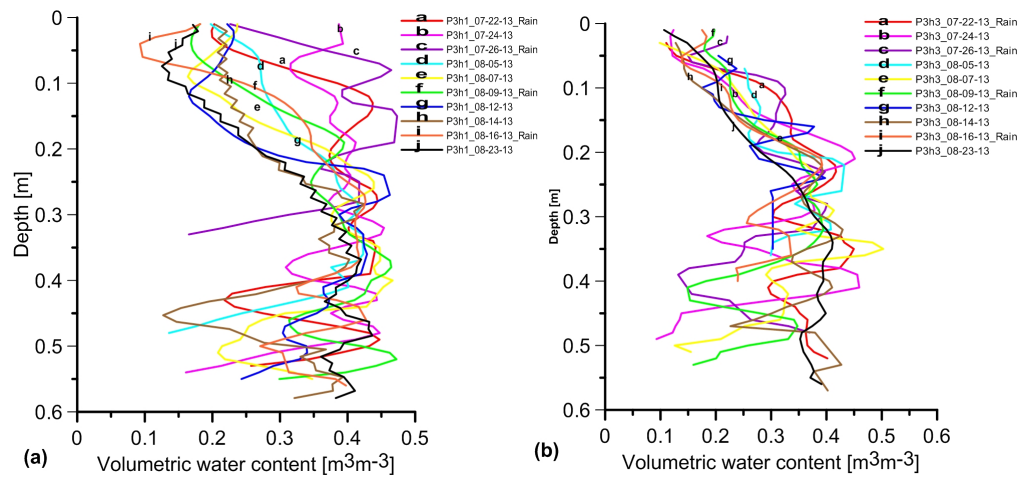


Figure A.3: Hoed plot VWC graphs (a) hole 1 (b) hole 3

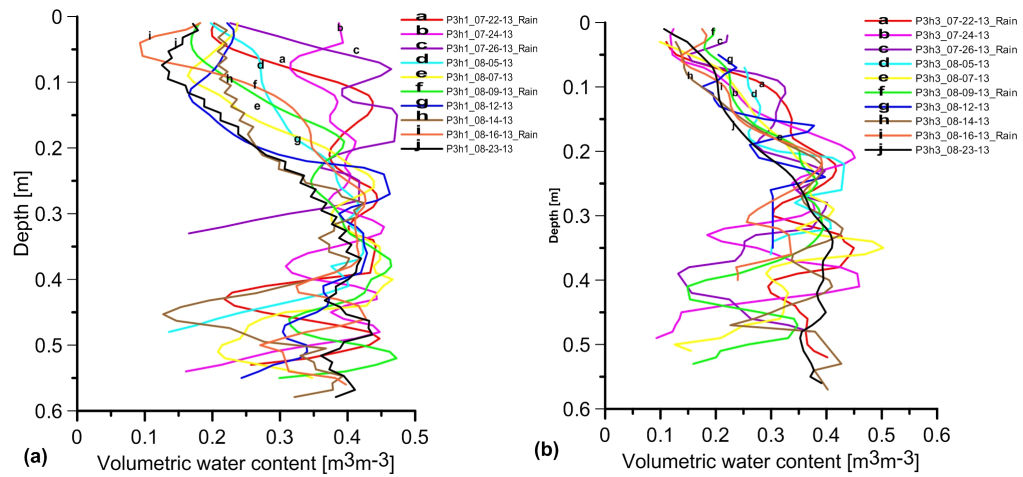


Figure A.4: No-till plot VWC graphs (a) hole 1 (b) hole 3

A.2 Calculation of Volumetric Water Content (VWC)

Table A.1: Calculation of Volumetric Water Content (VWC)

| 2D | 2T | D | $dx = 0.005$ | dT | Int. $V_{0.04 < V < 0.15}$ | V. H | Int. ε | Int. θ |
|-----------|-----------|----------|--------------|-----------|--|-------------|--------------------------------------|---------------------------------|
| 0.00 | 2.2408 | 0.0000 | 0.0050 | 0.0532 | 0.0940 | | | |
| 0.01 | 2.3472 | 0.0050 | 0.0050 | 0.0578 | 0.0866 | 0.0865 | 12.0370 | 0.2263 |
| 0.02 | 2.4627 | 0.0100 | 0.0050 | 0.0625 | 0.0800 | 0.0799 | 14.0824 | 0.2611 |
| 0.03 | 2.5877 | 0.0150 | 0.0050 | 0.0674 | 0.0742 | 0.0741 | 16.4129 | 0.2971 |
| 0.04 | 2.7225 | 0.0200 | 0.0050 | 0.0727 | 0.0688 | 0.0692 | 18.8067 | 0.3302 |
| 0.05 | 2.8678 | 0.0250 | 0.0050 | 0.0768 | 0.0651 | 0.0643 | 21.7428 | 0.3661 |
| | | | | | | | | |
| | | | | | | | | |
| | | | | | | | | |

A.3 Contour Map

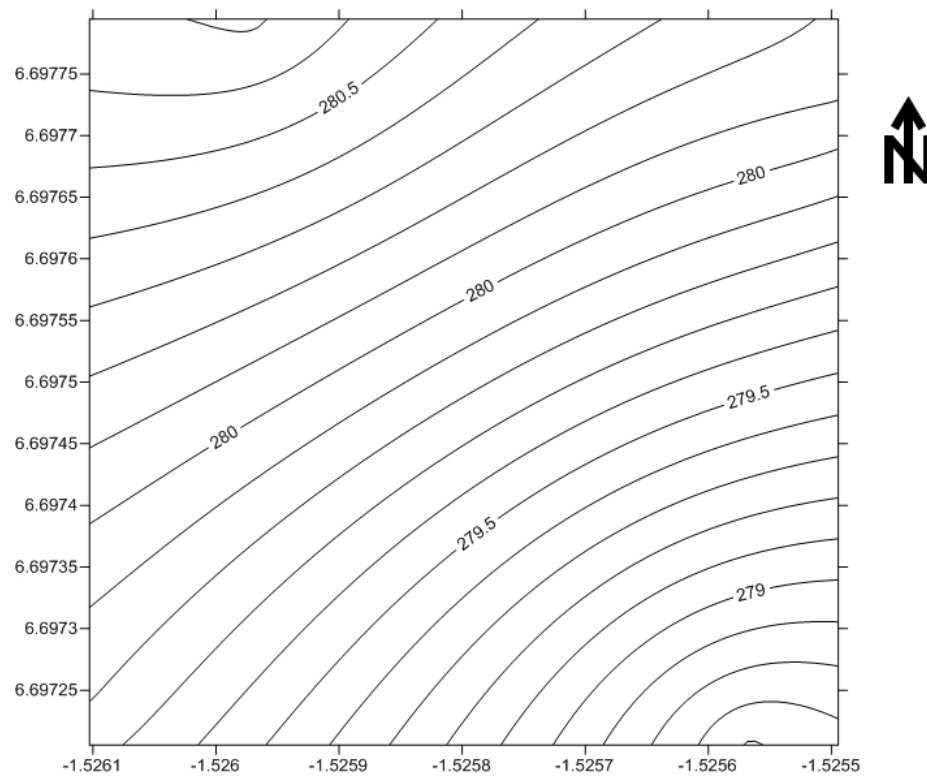


Figure A.5: Contour Map of study area showing elevation (m)

A.4 Shell Script Files

File: /home/equansah/Desktop/sontaa/compare2_files

Page 1 of 1

```
#!/bin/bash

filename="Profile1_1"
file=${filename}.dat
filename1="Profile1_2"
file1=${filename1}.DAT

awk 'NR==FNR{a[NR]=$1;next}{if (a[FNR]==$1) {print "1" > "3.txt"} else {print $0 > "3.txt"}}' $file $file1

#comparison is done on Profile1_1 and profile1_2 and the output is printed as 3.txt
```

Figure A.6: Shell script for Sorting of Data

File: /media/942857602286E8FE/Docum...1/data1_1/merging_filesdata1_1

Page 1 of 1



```
#!/bin/bash


filename="Profile1_1"
file=${filename}.dat
filename1="Profile1_2"
file1=${filename1}.dat
filename2="Profile1_3"
file2=${filename2}.dat
filename3="Profile1_4"
file3=${filename3}.dat
filename4="Profile1_5"
file4=${filename4}.DAT

paste $file $file1 $file2 $file3 $file4 | awk -F',' '{ printf "%1.2f\t%1.2f\t%3.6f\t%3.6f\t%3.6f\t%3.6f\t%3.6f\n", $1, $2, $3, $5,$7, $9, $11}'>Maizedata1_1.txt

#profile1_n (n=1,2,3,4,5) is the name of the data
#print column1 and 2 from file1.txt and column 2 from file2.txt
# and print the output as 'maizedata1_1.txt'
#chmod +x scriptname -this gives permission to run script#
```

Figure A.7: Shell Script for Merging of Files

Time lapse data
 0.20  Electrode spacing
 1
 185  Number of data points
 0
 0
 Time sequence data
 Number of time sections
 5
 Time unit
 Hours
 Second time section interval
 24.0
 Third time section interval
 24.0
 Fourth time section interval
 24.0
 Fifth time section interval
 24.0

Data


| | | | | | | |
|------|------|------------|------------|------------|------------|------------|
| 0.00 | 0.20 | 188.224900 | 195.755000 | 194.512100 | 214.900700 | 249.600000 |
| 0.20 | 0.20 | 231.415900 | 230.985200 | 223.521500 | 233.016600 | 256.775400 |
| 0.40 | 0.20 | 152.852200 | 170.570300 | 147.889500 | 187.845300 | 187.081900 |
| 0.60 | 0.20 | 282.650500 | 280.319400 | 342.013400 | 293.382800 | 321.783400 |
| 1.00 | 0.20 | 205.969400 | 230.817700 | 256.838900 | 241.348600 | 257.351400 |
| 1.20 | 0.20 | 203.106200 | 189.934900 | 185.118200 | 202.006700 | 222.868900 |
| 1.40 | 0.20 | 149.022300 | 182.957300 | 165.073300 | 180.330100 | 209.487900 |
| 1.60 | 0.20 | 186.217500 | 185.278300 | 197.506900 | 226.213100 | 230.057100 |
| 1.80 | 0.20 | 180.009300 | 200.386800 | 204.433300 | 218.734500 | 234.256700 |
| 2.00 | 0.20 | 169.851100 | 185.489700 | 195.258700 | 215.198300 | 227.271900 |
| 2.20 | 0.20 | 225.468000 | 239.950000 | 228.438900 | 241.470400 | 250.269600 |
| 2.40 | 0.20 | 248.876900 | 247.232900 | 212.327400 | 241.537100 | 284.992700 |
| 2.60 | 0.20 | 190.381000 | 226.646300 | 213.726800 | 233.617000 | 256.607800 |
| 2.80 | 0.20 | 287.185500 | 297.428700 | 250.054200 | 317.502500 | 351.211900 |
| 3.00 | 0.20 | 166.900100 | 195.265400 | 176.729800 | 213.741200 | 246.639000 |
| 3.20 | 0.20 | 189.779600 | 231.728700 | 231.272400 | 241.919600 | 280.565500 |
| 3.40 | 0.20 | 134.312500 | 155.148500 | 160.349100 | 188.955500 | 211.476500 |
| 3.60 | 0.20 | 203.395700 | 227.399800 | 223.998400 | 239.860700 | 266.598900 |
| 3.80 | 0.20 | 201.823600 | 221.124800 | 202.865000 | 225.019600 | 250.428700 |

Figure A.8: Sample time-lapse data file with five data sets

Appendix B

B.1 Used Softwares

- \LaTeX : typesetting and layout
- RES2DINV: Data processing
- ReflexW 4.5: Data processing
- Coral Draw X5 : graphics
- Golden Software Grapher 8: plots
- Golden Software Surfer 11 : plots
- MapInfo 10.5: Data processing and enhancing
- ArcGIS 10: Data processing and enhancing